UCSF

UC San Francisco Electronic Theses and Dissertations

Title

Microscale Material Strategies for Drug Delivery Applications

Permalink

https://escholarship.org/uc/item/6027q8f5

Author

Lykins, William

Publication Date

2020

Peer reviewed|Thesis/dissertation

Microscale Material Strategies for Drug Delivery Applications

by
William Lykins

DISSERTATION
Submitted in partial satisfaction of the requirements for degree of
DOCTOR OF PHILOSOPHY

in

Bioengineering

in the

GRADUATE DIVISION

of the

UNIVERSITY OF CALIFORNIA, SAN FRANCISCO
AND
UNIVERSITY OF CALIFORNIA, BERKELEY

Approved:

DocuSigned by:

Tejal A. Desai
5D917BC35F4B4A0...

Tejal A. Desai
_____
Chair

DocuSigned by:

Deanna Kroetz
DocuSigned by:4AA...

Deanna Kroetz
_____

Daniel Fletcher
DD28103531044C7...

Daniel Fletcher
_____

_____

_____
Committee Members

Acknowledgements

It has been the highlight of a lifetime to have been a small part of the Desai lab for the last 5 years. I am eternally grateful to the people in the ab who have given their time and energy to mentor me, including: Cameron Nemeth, Jean Kim, Erica Schlesinger, Daniel Johengen, Xiao Huang, Joel Finbloom, Cade Fox, Rachel Chavalier, and Dan Bernards. I am also grateful for the students who I've had the opportunity to mentor, who entrusted me with my time and never failed to astonish me with what they were able to accomplish: Kai Wisniewski, Eva Hansen, Natalie Wu-Woods, and Andre Lai. I wanted to especially acknowledge Eva Hansen, who for the last 2 years has been an invaluable collaborative and scientific partner. I have supreme confidence leaving many of my projects to her, and I know that she will find a lot of success in this work. I also wanted to say thank you to Dr. Tejal Desai, as a mentor and as someone who is willing to fight for students in lab and out. There are so many lessons that I will carry with me, and I hope that you will be able to see them pay off in the rest of my career. I also want to acknowledge my other dissertation committee members, Professor Deanna Kroetz (UCSF) and

iii

I also wanted to say thank you to my friends and to the UC Berkeley-UCSF Graduate Program in Bioengineering, and to the Bioengineering Association of Students (BEAST). It is astounding that I got to be in such a tremendous group of people, and seeing what they have done and accomplished has inspired me more than anything. To my friends: I've likely already said this to you, but I'm grateful to the people in and beyond grad school who laughed with me, who cried with me, and who dreamed of a brighter future with me. I am also thankful to my wonderful partner Sierra Fitch. There is so much to write, but you have been so much to me the last 6 years, and I couldn't have done it alone. Through hard times and good times, you have always been the person I could count on to be there for me, and the person I knew I could confide in if something went wrong. I am so grateful for your adventurous spirit, and I can't wait to see the world with you. You and your family, Tom, Christine, Eliza, and Dottie, have been a much-needed bedrock when the world seemed to be spinning to fast. I cannot wait to spend the rest of my life with you, and hopefully after this is all said and done, I can provide a life that is truly worthy of the wonder you are.

Finally, I want to thank my Family. It always has meant so much to know that you would support me no matter what. And even if things have not always gone as intended, and things haven't always been smooth, I have always known you were there. Hopefully in the future I'll be a little closer to home, and there won't be quite so long gaps between coming to visit.

Abstract

William Lykins

Microscale Material Strategies for Drug Delivery Applications

As the global market for next generation therapeutics continues to expand, there is a growing need to ensure that these strategies remain accessible. One strategy that has been historically successful in the context of pharmaceuticals is to develop new dosage forms to better conform to the clinical needs of the end user, which has been successful in the field of contraceptives, anti-psychotics, and other therapeutic areas. However, as our understanding of the underlying biology of disease and our ability to more easily generate highly defined microscale materials matures as it has in the last several decades, we have the ability to now adapt both the therapeutic and the dosage form to specific clinical indication. Manipulation of free-standing microscale materials that have the ability to function on biological length scales opens up the possibility of generating therapeutics that can be finely tuned to specific clinical needs, but has been historically limited by the intrinsic properties of conventional materials. Here, we present two examples of adapting a material platform to meet both a clinical need and a need for microscale materials that better conform to pharmaceutical standards. First, we discuss the use of polymer blends as a strategy to reduce the mismatch between useful lifetime and material residence times in long-acting drug eluting implants. Next, we discuss the development of a novel strategy for fabricating planar microdevices for oral protein delivery, composed entirely of materials used in existing FDA approved products, and how we can use the flexibility of this technique to understand how microscale materials behave in the gastrointestinal tract. These findings open the door to developing new, and more accessible, therapeutics to meet the diversifying needs of patients and providers on a global scale.

Table of Contents

List of Figures

List of Tables

Chapter 1 –Designing Long Acting Implants for HIV Pre-Exposure Prophylaxis via Microscale Techniques

1.1 Abstract:

Oral pre-exposure prophylaxis for the prevention of HIV-1 transmission (HIV PrEP) has been widely successful as demonstrated by a number of clinical trials. However, studies have also demonstrated the need for patients to tightly adhere to oral dosing regimens in order to maintain protective plasma and tissue concentrations. This is especially true for women, who experience less forgiveness from dose skipping than men in clinical trials of HIV PrEP. There is increasing interest in long acting (LA), user independent forms of HIV PrEP that could overcome this adherence challenge. These technologies have taken multiple forms including LA injectables and implantables. Phase III efficacy trials are ongoing for a LA injectable candidate for HIV PrEP. This review will focus on the design considerations for both LA injectable and implantable platforms for HIV PrEP. Additionally, we have summarized the existing LA technologies currently in clinical and pre-clinical studies for HIV PrEP as well as other technologies that have been applied to HIV PrEP and contraceptives. Our discussion will focus on the potential application of these technologies in low resource areas, and their use in global women's health.

1.2 Introduction:

Despite international success in the prevention and treatment of HIV-1, infection rates have stagnated throughout the 21st century.[1] Over the past 10 years oral pre-exposure prophylaxis (PrEP) has been found to successfully reduce the sexual and parenteral transmission of HIV.[2–5] Currently, there is only one approved HIV PrEP product, consisting of a fixed dose combination of two nucleoside analogue reverse transcriptase inhibitors (NRTI), tenofovir-disproxil fumerate 200mg (TDF) and emtricitabine 300mg (FTC), sold under the brand name *Truvada*® as a once daily oral pill. When taken daily, *Truvada*® is highly effective at preventing the sexual transmission of HIV by more than 75 percent with regular use,[2,4] and upwards of 92 percent with perfect adherence.[6] This highlights the major drawback of currently available HIV PrEP: the need for daily adherence to an oral pill regimen. Furthermore, oral PrEP has lower forgiveness for prevention of vaginal transmission, which requires use of at least 85 percent of expected doses (6 of 7 weekly doses) to maintain protective active pharmaceutical ingredient (API) concentrations in the lower female reproductive tract, whereas protective API concentrations in rectal tissues can be maintained with as little as 28 percent of expected doses (2 of 7 weekly doses).[7,8] Notably, two clinical trials of orally dosed HIV PrEP among female study populations that had very low estimated product use (less than 40% of participants) were unable to demonstrate effectiveness.[5,9] To overcome this adherence challenge, there has been extensive research and development invested in the optimization of long-acting (LA), user independent HIV PrEP formulations.[10–17] Feedback from end-users suggests that LA dosage forms are not only acceptable, but preferred over more frequent dosing regimens.[18–20] Healthcare providers also appear to have a preference for LA approaches.[Lutnick et al 2017, unpublished data]

In this review, we will summarize LA HIV PrEP delivery systems (defined here as at least 30 days between doses) that are systemic (excluding transient topical and local delivery technologies). We will also address technologies that have not been directly applied to HIV PrEP, but offer promising contributions to the future delivery pipeline. Our discussion will focus on the use of these technologies in vulnerable populations, low resource settings, and their application to global women's health.

1.3 Injectables for LA HIV PrEP:

The field of LA systemic HIV PrEP has been dominated by LA injectable formulations of highly potent antiretrovirals (ARVs).[10,17,21,22] To date, a number of phase I and II clinical trials have been carried out with a range of ARVs, with a phase IIb/III efficacy trial ongoing now for LA Cabotegravir.[hptn.org/research/studies/176, HPTN 083]

LA injectables span a wide range of formulations and processing strategies.[23,24] In this review we will primarily focus on wet nano-milling approaches that have been applied to the development of LA ARV depot injectables. Nano-milling describes the process of applying physical agitation and stresses to reduce the size of poorly soluble solid drug crystals as a means to improve their pharmacokinetic (PK) properties.[25–28] Nano-milling uses coated metal ball bearings (often zirconium) to mechanically grind drug suspensions that include a stabilizing polymer or surfactant coating[29,30]. The coating enables colloidal stability of the particles and prevents agglomeration of the nano-suspension by blocking hydrophobic collapse. This is accomplished either via steric hindrance or ionic repulsion. Common stabilizers include polyethylene glycol, cyclodextrin, and other polymers or surfactants.[23,24] Nano-milling — generating particles on the order of 200nm in diameter[23] — dramatically increases the surface area of a drug suspension. Increased surface area

has a positive impact on dissolution by increasing the solvent-accessible drug.[31] This increases the possible peak plasma concentration (C_{max}), compared to more traditional injectable solutions.[32,33] Because absorbance and dissolution time is delayed in the case of an intra-muscular (IM) nano-suspension injection, there is also an improved safety profile and a decrease in injection site reactions.[34,35] It is important to note however, that because the distribution of nano-suspensions is dissolution limited, concentration dependent kinetics of low solubility agents can be accompanied by long, sub-therapeutic PK tails.[10,24]

In the design and selection of an agent for a LA injectable formulation it is necessary to understand the potency (IC_{50}), hydrophobicity (LogP), and pharmacokinetic parameters (clearance, distribution kinetics etc.) of the API of interest.[36] There are a wide range of APIs available for the treatment and prevention of HIV that span orders of magnitude in potency and solubility. However, low solubility high potency APIs are preferred to best extend the release of the API from a nano-suspension and to decrease the total dose of API needed for effective protection. For this reason, the development of LA injectables has primarily focused on two agents: the non-nucleoside reverse transcriptase inhibitor (NNRTI) rilpivirine (RPV), and the integrase strand transfer inhibitor (INSTI) cabotegravir (CAB). Both APIs exhibit sub nanomolar potency, and are minimally soluble in biological fluids (RPV LogP=4.32, CAB LogP=2.20)[36] making them ideal candidates for LA injectable delivery applications[**Table 1-1**]. [10,37,38] Alternative APIs such as the INSTI raltegravir and the NNRTI nevirapine have been studied as LA injectables, however because of limited potency and residence time, neither API is currently being pursued in human clinical trials.[22,39][clinicaltrials.gov 2020]

CAB exhibits sub nano-molar potency against various lab strains of HIV-1 (IC_{50} 0.22nM to 0.34nM), and binds tightly to serum albumin leading to a target IC_{90} (PA-IC_{90}) of 166 ng/ml.[17] This

high potency combined with low aqueous solubility (0.015mg/ml) and low clearance (0.32mL/min/kg), has identified CAB as a target for LA PrEP applications.[17,40] CAB is related to the INSTI dolutegravir, but has been modified to increase serum protein binding, while reducing solubility and clearance, affording CAB an extended *in vivo* half-life compared to dolutegravir.[41] This extended half-life has made it possible to formulate a once per 8 weeks 4mL intramuscular (IM) injection of 800mg of CAB delivered bilaterally in the gluteus with two 2mL injections.[17] Bilateral dosing was shown to increase dissolution rate and C_{max} after dosing.[17] LA CAB is observed to persist for an extended period of time in serum, with a half-life of 25-54 days after an IM depot injection.[42] Repeat dosing studies have also shown that CAB accumulates in plasma during monthly dosing, suggesting that bi-monthly would be most effective at maintaining non-toxic serum concentrations.[21] CAB is currently being explored as a monotherapy for HIV prevention, and in combination with RPV as a therapeutic option.[21]

RPV is a potent API, with an unbound IC_{50} of 0.26nM in culture, leading to a serum PA-IC_{90} of 12ng/ml.[38,43] It is known to be potent against a range of HIV-1 isolates, and has been found to be generally tolerable to patients during repeat dosing.[44,45] The nano-suspension was formulated with a Poloxamer 338 (Pluronics F108) stabilizing surfactant, and ground using 500μm zirconium beads in a continuous wet milling process to a particle size on the order of 200nm then formulated in water along with tonicity agents at a concentration of 600mg/mL.[43,46,47] LA RPV has been dosed either at 600mg as a single IM injection, or at 1200mg in two bilateral injections in the gluteus.[47] Phase Ia human studies of LA RPV have found that RPV poorly distributes to vaginal and cervical tissues as measured by correlation with blood plasma concentrations.[48] Additionally, RPV only modesty distributes to rectal tissue at high IM dosages (1200mg).[48] Measurements of viral inhibition using homogenized vaginal and cervical tissue explants show little to no efficacy 40

6

days after a single 600mg or 1200mg dose, with mild suppression in rectal tissue.[48] However, dose proportionality studies using beagle dog models of PK distribution suggest that RPV accumulates in lymphoid tissues, potentially due to macrophage engulfment.[43] These findings suggest that RPV may be limited in its utility as a PrEP agent because of its limited presence in virus exposed tissues. However, LA RPV is potentially promising as a LA treatment option because of its accumulation in lymphatic tissues which are thought to be viral reservoirs.

In the case of an adverse reaction to an LA injectable API, removal or dialysis of the API from whole blood is not possible, necessitating a 14 day lead in oral dose to assess individual safety for LA CAB and RPV.[21,48,49]. Additionally, both LA formulations take on the order of a week to achieve therapeutic plasma concentrations, so even when safety in an individual is understood, lead in oral dosing might be required to cover this sub-therapeutic window. Clinical research with LA CAB has also required a lead out oral *Truvada®* regimen to cover the sub-therapeutic PK tail of CAB for up to a year after the end of the LA regimen to reduce the risk of break through resistance in volunteers.[49] These additional oral dosing requirements increase the complexity of the dosing regimen, and could interfere with appropriate compliance. While most study participants (70%-100%) experience some form of injection site discomfort or pain, severe discomfort, which may disincentivize users, was rare.[21]

In addition to small molecule therapeutics, there has been increasing interest in the use of broadly neutralizing anti-HIV antibodies (e.g. VRC01) as a prophylactic.[50–54] Antibodies have the advantage of being both highly potent, and naturally long lasting with serum half-lives on the order of a month. In studies using non-human primates, a single infusion of VRC01 was protective against high dose rectal challenge for up to two weeks.[50,51]. *In vitro* studies of tissue explants have suggested that various antibodies might be effective at preventing mucosal transmission of HIV.[55]

Current ongoing studies such as the AMP trials (HPTN 085 and HVTN 704) will provide more information on the clinical effectiveness of antibody based prophylaxis.[clinicaltrials.gov #NCT02716675] There are also ongoing antibody engineering studies focused on extending the half-lives of broadly neutralizing antibodies. By modifying the Ig constant region, researchers increased binding affinity to FcRn receptors by an order of magnitude, and were able to extend the serum half-lives of IgGs by 4 fold out to three months without a detectable decrease in antigen binding potency.[56,57] This extended half-life in combination with efforts to formulate high concentration (100mg/mL) antibody reagents makes antibody based PrEP injections a potentially feasible approach.[58]

1.4 Implantable Delivery Technologies for LA HIV PrEP.

The range of implantable drug delivery technologies for a variety of indications is vast and has been reviewed extensively elsewhere.[59–64] Compared to LA injectables, LA ARV releasing implants have four main advantages: 1) the capacity to enable release profiles that can exceed 12mo in duration [65–67], 2) the capability to enable extended zero order release, and "flat" PK profiles with limited sub-therapeutic tails, 3) the capability to be fully removed and "reverse" treatment, and 4) the ability to deliver highly soluble ARV agents.[63,68,69] Implantable drug depots, like the etonogestrel Nexplanon® rod, that utilize outpatient implantation procedures necessitate local anesthetic as well as wound closing measures.[70,71] Feedback from regulatory agencies has suggested that devices should maintain protective release profiles for more than six months per procedure.[49] In end user feedback surveys, both men and women have shown a willingness to undergo mild to moderate discomfort to achieve LA prevention of unintended pregnancy or HIV given long dosing intervals.[18,72]

Most LA drug releasing implants are based on drug embedded in a polymer matrix, or drug surrounded by a diffusion limiting membrane. While several commercial products are based on matrix type systems, most notably contraceptive implants,[67,73,74] this review will focus on the use of reservoir type devices. Such reservoir devices are capable of zero order, or internal concentration independent, drug release which enables constant mass flux and flat PK profiles.[61,69] In a drug reservoir system, biological fluid permeates a membrane and enters a drug containing core. Solid drug is then dissolved in the fluid (dependent on the solubility of the drug) creating a constantly saturated solution, enabling a constant concentration gradient in sink conditions [**Figure 1-1**].[69,75] Based on the principles of Fickian diffusion of mass through a rate controlling membrane, mass flux depends on two key parameters: 1) the interaction of the API with the membrane that determines its ability to permeate and diffuse through the membrane, and 2) the geometry (e.g.. surface area), density, and thickness (diffusive length scale) of the material comprising the membrane.[76] An alternative method to achieve zero order release is a single file diffusion regime, where the membrane pore size is on the same order as the hydrodynamic-diameter of the deliverable, preventing multiple molecules from exiting simultaneously from the same pore.[77] These kinds of devices are able to achieve zero order release of biological macromolecules, such as proteins and hormones, which is desirable for a number of different indications.[78,79]

Devices for the controlled release of HIV PrEP agents [**Table 1-2**] have focused on the release of tenofovir alafenamide fumarate (TAF), a more potent pro-dug of TDF.[80] Compared to TDF, TAF is an order of magnitude more potent based on serum concentrations (IC50 TAF=0.005µM, TDF=0.05µM).[80] Both TAF and TDF have the same active pharmaceutical form, tenofovir di-phosphate (TFV-DP), and mechanism of viral inhibition, premature termination of viral genome elongation.[80] However, TAF is unique in that it is only converted to TFV-DP in the presence of an intracellular cathepsin A enzyme, creating a driving force for the cellular accumulation and persistence of TAF in peripheral blood mononuclear cells (PBMCs), CD4+ T-Cells among other cell types.[81] TAF is also serum stable, extending its serum half-life around 100 fold beyond TDF (90min for TAF, 0.41min for TDF).[80,82] The nanomolar potency and serum half-life of TAF make it an attractive candidate for LA delivery. Because of its relative hydrophilicity (LogP 1.25),
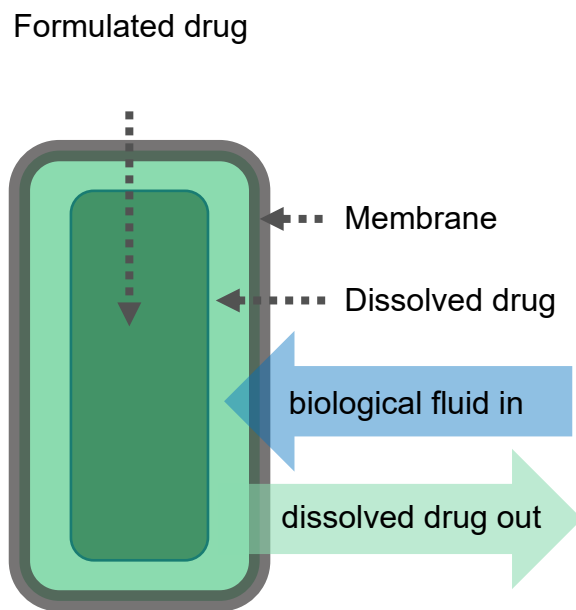
Figure 1-1:
Diagram of reservoir based controlled release device

tenofovir and its prodrugs are not good candidates for LA injections.[36] Investigators are also pursuing alternative APIs for long or short acting delivery such as the potent NRTI EFdA, which has also shown increased potency against common tenofovir resistance mutations.[83,84]

While there are numerous options for rate limiting membranes and polymer systems for matrix type devices[64], a smaller subset has been used in the context of HIV PrEP. It is necessary to consider the polymer along with the API, as there interaction will ultimately govern the diffusion through and partitioning of drug into the membrane.[64] Hydrophilic drugs tend to pass quickly through hydrophobic layers without partitioning into the polymer matrix in order to reduce energetically unfavorable interactions, whereas interactions between the API and the membrane will slow release.[85] Of the more conventional membrane materials there are polyesters such as polycaprolactone (PCL),[75] polyurethanes (PUR),[86] polyvinyl alcohol (PVA),[87,88] poly(ethylene-co-vinyl acetate) (EVAc),[89] and silicone.[90,91] Specifically, researchers have looked at PVA and PCL in the context of HIV PrEP.

PVA is a non-degradable hydrophilic polymer that can be formed into membranes using crosslinking or heat based polymerization, often depending on a separate co-polymer for structural support.[87,92,93] PCL is a relatively hydrophobic "soft" polyester that is bioresorbable via hydrolysis.[75,94,95] The degradation properties of PCL are tunable depending on the molecular weight blend of polymers used, on a scale of months to years, from implantation to total dissolution.[94,96] PCL has notably been used in the development of implantable contraceptive technologies.[97,98]

Oak Crest Laboratories are developing silicone-PVA implantable devices, fabricated from a piece of silicone tubing that has 1mm holes punched in its axis, that are then coated with a heat crosslinked PVA membrane [**Figure 1-2**].[99] The device is 40mm by 1.9mm with a wall thickness of 0.4mm.[99] The relative impermeability of silicone compared to PVA limits the release kinetics based on the number of PVA membranes included in the device, which can be tuned to achieve the desired release properties. The device demonstrated an in vitro release rate of 0.92mg TAF per

day, and an in vivo release rate of 1.07mg TAF per day. *In vivo studies* in a dog model of TAF PK, demonstrated that constant serum concentrations of TAF and intracellular concentrations of tenofovir-diphosphate were maintained above therapeutic levels for upwards of 40 days.[99] This device is non-degradable, and similarly to contraceptive implants, would need to be removed at the end of its lifetime.
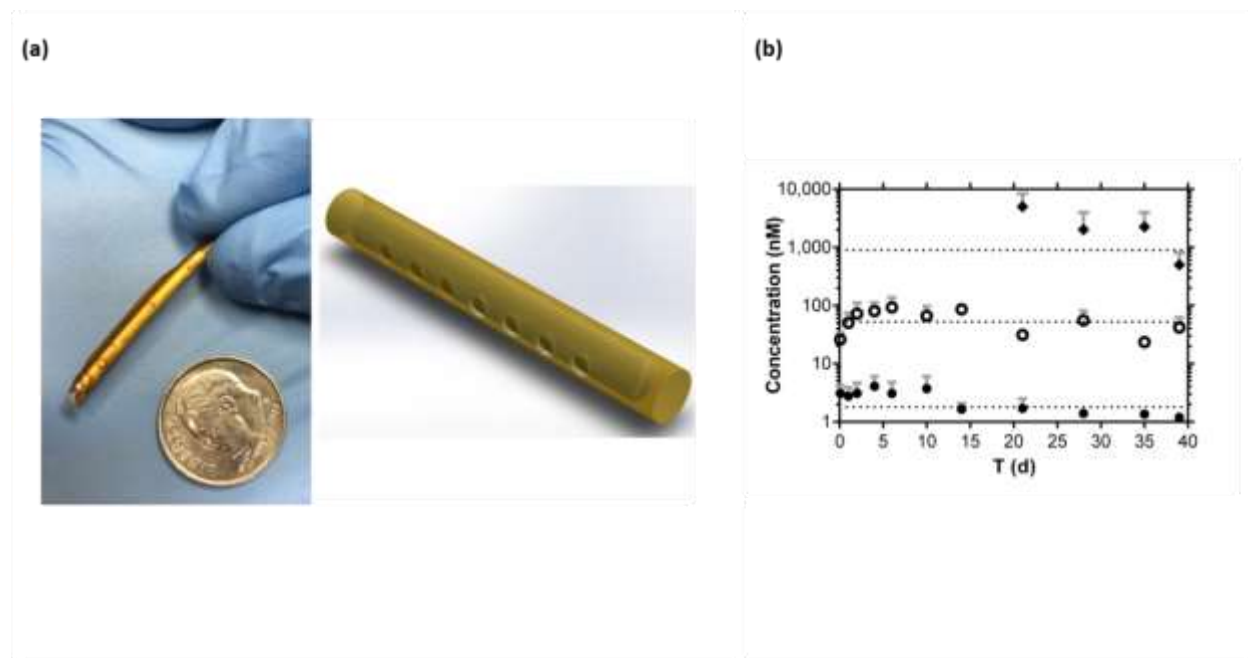
Figure 1-2:
Oak Crest Device (a): Device schematic and picture, (b) in vivo measurements of TFV (open circles), TAF (closed circles) and intracellular TFV-DP (diamonds). Each data point represents the mean ± SD, and dashed lines represent the median value for each analyte over the 40 day study. From Gunawardana et all [104], used with author permission

The "Thin Film Polymer Device" (TFPD), developed by the laboratory of professor Tejal Desai (UCSF) jointly with RTI International laboratories, consists of a thin flexible solvent cast 80kDa PCL membrane surrounding a core of TAF-PEG 300 in a 2:1 ratio by mass [**Figure 1-3**].[100] PEG-300 was included as a solubilizing excipient for TAF and helped to establish a membrane controlled, rather than dissolution controlled, release regime when using a 25µm thick membrane.[100] The TFPD is rod shaped, 40mm x 2.5mm, with heat annealed seams to seal the

reservoir. This device can be loaded with upwards of 150mg of TAF and has a release rate of 1.4mg/day which is thought to be physiologically relevant for protection, giving an estimated device lifetime of 3 months.[100] Because the TFPD is made of bioresorbable PCL, the device does not need to be surgically excised and instead will degrade after the drug payload has been exhausted. Additionally, the TFPD was able to maintain the stability of TAF in vitro for upwards of 100 days, as verified by HPLC, with only minor evidence of degradation.[100] This is especially significant in the delivery of a relatively unstable API like TAF, where *in vivo* stability might be non-trivial.[101,102] Small animal preclinical studies with the TFPD are ongoing, but preliminary rat studies have demonstrated the ability of the TFPD to function in an animal model for more than two weeks. Additionally, studies on the effects of gamma sterilization have shown negligible effects on drug purity or polymer degradation. Ongoing studies have demonstrated that the device can be removed up to one month post implantation, which is critical for future safety evaluations. [Swarner 2016 CROI poster, Schlesinger 2016 CROI Poster, Swarner 2016 HIV R4P Poster]

It is also of interest to consider other polymers and LA device systems for applications in HIV PrEP. Polyurethanes (PURs) have tunable hydrophilicity and degradation properties, and have been applied extensively in the area of membrane based implantable drug delivery devices.[86,103,104] Notably, PURs have been used in the development of reservoir devices for the long term delivery of the peptide steroid agonist histrelin in the treatment of advanced prostate cancer (Vantas) and central precocious puberty (Supprelin LA).[65,105–107] Non-degradable polymers such as ethylene-vinyl acetate (EVAcs) have been applied extensively in the most modern iteration of implantable contraceptive devices including the Nexplanon® system. EVAc has many desirable qualities as a controlled release medium, but can be difficult to source at a medical grade.[67,89,108]
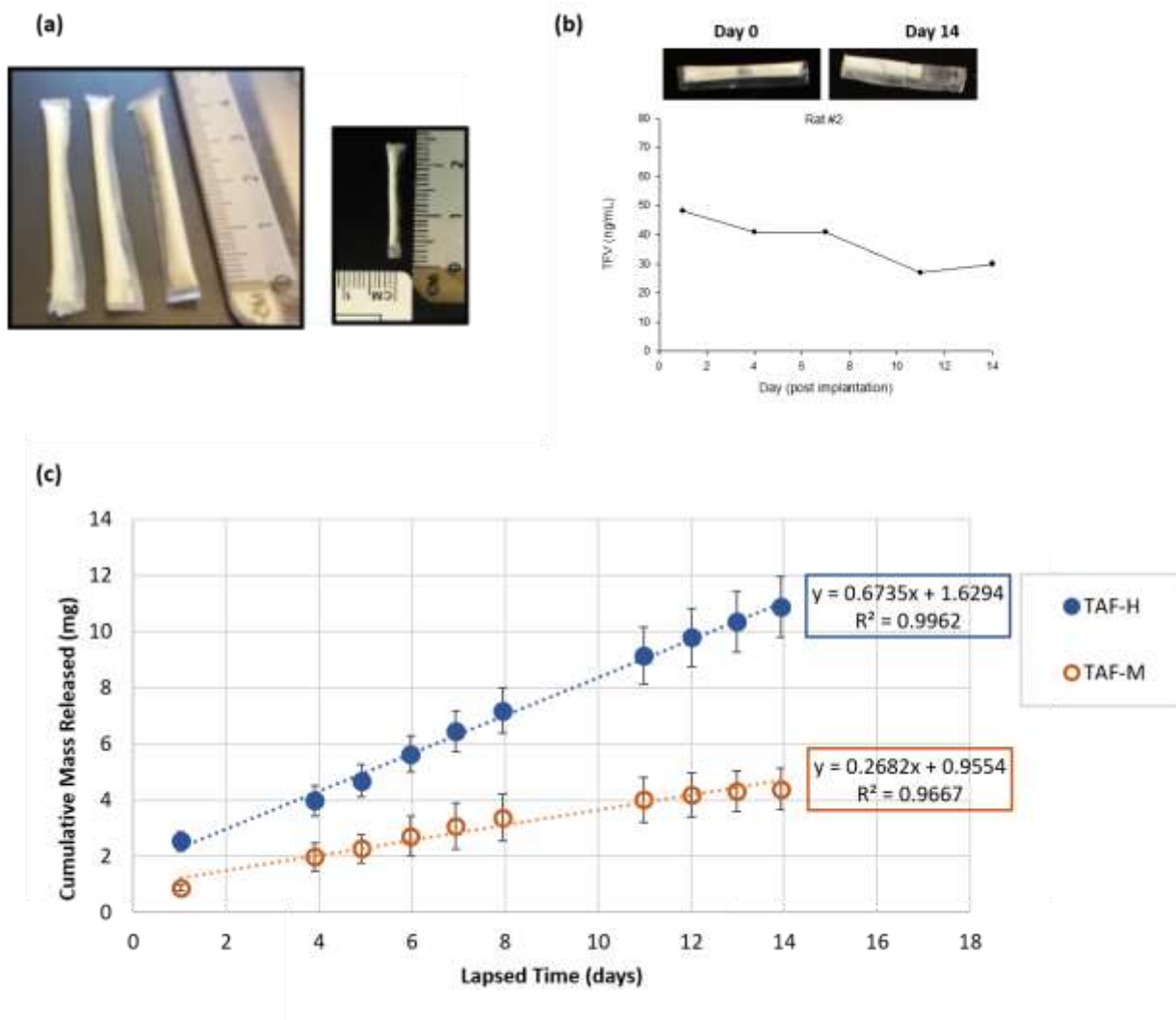
Figure 1-3:
TFPD Device. (a) Device pictures and fabrication scale. (b) in vivo Daily release for high dose (TAF-H) device over 14 days, with pictures of device pre and post implantation. (c) in vitro release kinetics for high and medium dose (TAF-M) TAF devices, each point represents mean ±SD. From Schlesinger et al 2016, used with author permission.

There is also interest in long term, refillable silicon nano-channel devices.[79,109,110] These devices are constructed from rationally designed silicone nano-slits, with a width corresponding to the hydrodynamic-diameter of the intended deliverable, which can be tuned to enable single file diffusion through the slits. By altering the channel lengths, and channel density, it is possible to tune the release of APIs from these devices.[79] These devices have seen extensive studies in animal models, and have been shown to rapidly establish zero order release regimes that persist for

upwards of 70 days with multiple APIs.[79] Investigators are also exploring methods to make the devices refillable, potentially enabling life-long PrEP administration from a single implant.

Intarcia Therapeutics in conjunction with the Bill and Melinda Gates Foundation are developing a osmotic pump based implant for long term HIV PrEP delivery. Recently their DUROS® device has completed phase III clinical trials for the delivery of exenatide for the treatment of type 2 diabetes as a 9 month subcutaneous implant.[111] The DUROS® device can achieve zero-order release of a range of APIs, and can be designed to last for 6-12 months.[112]

In addition to LA HIV PrEP technologies, there is an interest in and need for technologies that would afford users with a narrower window of protection, as well as multipurpose devices that could combine contraceptives with antivirals (MPTs). These technologies have taken many forms, including vaginal films,[83,113,114] microneedle patches,[eg. PATH] ARV eluting intrauterine devices,[eg. CONRAD] vaginal inserts,[115,116], vaginal rings,[74,117] and vaginal gels.[118,119] It is the goal of these and other multipurpose prevention technologies to decrease the burden of both HIV and unintended pregnancies in women in low resource areas.[120]

CONRAD, in collaboration with Dr. Patrick Kiser (Northwestern University), is developing a MPT intrauterine system (IUS) for the sustained (1+ year) use. A first-generation product in preclinical stages of development combines the INSTI elvitegravir (EVG) with copper as a nonhormonal contraceptive. The design of the device builds on that of existing T-shaped contraceptive IUS (e.g., Mirena, Paraguard). To date, this EVG-eluting IUS has demonstrated preclinical proof of concept that an ARV administered via the intrauterine route can be distributed throughout the female reproductive tract in animal models at levels expected to be prophylactic (Clark et al., 2016, poster P07.40, HIV R4P, Chicago IV). SHIV challenge studies in the pig tailed macaque were performed in 2017.[121]

1.5 Summary and Future Prospects.

Table 1-1:
Injectable LA PrEP Technologies in Development

API	Study Phase	LogP	PA-IC$_{90}$ (nM)	Formulation	Injection Concentration	Number and volume of injections	Dose Schedule
Rilpivirine (RPV)	2b (combination with LA CAB)	4.32	32.75	200nm particle formulated with poloxamer 338 as a stabilizer	300mg/ml	2 x 2mL IM injections	Bi-monthly
Cabotegravir (CAB)	2b/3	2.20	166	200nm particle with stabilizing surfactants and tonicity agents	200mg/ml	2 x 2mL IM injections	Bi-monthly

LA HIV PrEP should ultimately simplify HIV prevention methods, and thereby increase user adherence (specifically, quality of execution and persistence).[122,123] There is substantial precedent in the contraceptive space for the movement toward LA HIV prevention strategies, including 2-3

month LA injectables like Depo-Provera and Net-En, and 3-5 years LA implantables such as the Nexplanon® rod or the Jadelle 2-rod system. These products have dramatically expanded access to contraceptives for women globally by enabling increased ease of use and coverage.[124] Current products in clinical trials for LA HIV PrEP (e.g. LA CAB) promise a reduced dose burden, from daily oral pills to bi-monthly injections, which would dramatically reduce potential user treatment

Table 1-2:
Implantable LA PrEP Technologies in Development

Device	Device Type	Study Phase	Primary Materials	Contents	Device Dimensions	*In Vivo* Release Rate (mg/day)	Device Life time (days)
Oak Crest	Reservoir, non-degradable	Pre-Clinical	Silicone and PVA	TAF	40mm x 1.9mm	1.07	40
UCSF/RTI TFPD	Reservoir, bioresorbable	Pre-Clinical	PCL	2:1 TAF:PEG 300	40mm x 2.5mm	1.4	30

error.[21] However, the need for lead in and lead out dosing concurrent with current injectable formulations might make them cumbersome in practice. Implantable products, currently in preclinical trials could further reduce this dosing interval to once every six months or longer. There are still substantial challenges to be overcome for LA HIV PrEP, including demonstrating efficacy

17

in human trials. However, based on continued interest in increasing prevention options to vulnerable populations, embracing LA systematic HIV prevention technologies is necessary, and a clinical breakthrough is likely in the near future.

Chapter 2 – Measuring and Tuning the Degradation Profiles of Long Acting Polycaprolactone Implants

2.1 Abstract

Polycaprolactone (PCL) is a bioresorbable polyester that has been widely used in biomedical applications since the 1970s. Because PCL undergoes bulk degradation, it is especially amenable to drug delivery applications. To ensure safety, a drug eluting implant must remain fully intact throughout use and, once the drug is exhausted, the implant should degrade. Many PCL based implants target delivery on the order of six months to one year, while the time to degradation of PCLs are often on the order of multiple years. It is known that the time to degradation of PCL is directly related to its initial molecular weight. However, the limited integrity of neat low molecular weight PCLs make them unsuitable for implantation. Here, we outline an approach to tune the time to degradation of PCL, by blending low and high molecular weight polymers. We show that the degradation rate and permeability of PCL films are independent of their composition. Additionally, we demonstrate that the incorporation of as little as 25% (w/w) of a high molecular weight polymer can rescue the mechanical properties of a low molecular weight material. This enables a rational approach to design a material blend for any delivery application, without sacrificing material properties.

2.2 Introduction

Polycaprolactone (PCL) is a polymer that has been prevalent in the field of biomaterials and drug delivery since the 1970s. It is both bioresorbable and biocompatible and has been used in several FDA approved systems including sutures (e.g. Monacryl®) and root canal fillings (e.g. Resilon™).[125] Relatively inexpensive and with a comparably long-term bulk degradation, on the order of months to years, PCL is well-suited for tissue engineering implants and long-acting drug delivery systems.[126–129]

Thin PCL films are semipermeable, allowing water and small molecules to permeate while obstructing the passage of large molecules and particles.[75] It is also possible to introduce porosity into PCL films, rendering the films permeable to large and small molecules alike.[78,130,131] PCL loses its integrity when it reaches a critical molecular weight, which results in fragmentation and would impact the integrity of a drug delivery device.[132] Therefore, it is critical to tailor PCL degradation such that fragmentation only occurs after complete drug depletion and within a reasonable time-course compatible with administration of additional implants in the same location.

PCL degradation is well studied both *in vitro* and *in vivo*, providing a plethora of information and experimental protocols.[125,132,133] According to Pitt *et al.*, PCL degradation *in vivo* can be empirically described by an exponential decrease in average molecular weight over time, as shown in **Equation 1**.[132] This model was originally adapted to characterize the degradation kinetics of PLA and its copolymers, but has been demonstrated previously to be a suitable predictor of PCL degradation as well.[132]

$$M_n(t) = M_0 e^{-k't} \qquad\qquad \text{Eq. 1}$$

Where $M_n(t)$ is the number average molecular weight at time t, M_0 is the starting molecular weight, k' is the exponential degradation rate constant and k is the linear degradation constant. The form of **Equation 1** assumes that the dominant degradation mechanism is autocatalyzed acid hydrolysis from exposed acid groups on the terminus of polymer chains.[132] Throughout the degradation process, more and more acid groups are exposed, leading to a first order kinetics model. This equation has been employed to fit degradation behavior for an extended period until fragmentation occurs.[132] An alternative model assumes that degradation is dominated by random chain hydrolysis, meaning that that cleavage of ester bonds is dominated by the water present in biological fluids. This interpretation assumes the PCL film is uniformly saturated with water, leading to a constant velocity degradation model, as seen in **Equation 2.**[134] The various relevance or dominance of these two degradation models has been studied extensively for PLA and PLGA, but relatively little analysis has been done in recent years for PCL degradation routes.[135,136] Once fragmentation begins, it is hypothesized that an additional mechanism of degradation, characterized by a loss of mass and generation of soluble degradation products, becomes significant.[137] Regardless of which model is applied, time to PCL fragmentation depends on both the rate of degradation (k' or k) as well as the starting molecular weight (M_0). Therefore, one simple way to tailor PCL lifespan is to design around starting molecular weight of the polymer.

$$M_n(t)^{-1} = M_0^{-1} + k \times t$$

<div align="right">Eq. 2</div>

While the dependence of PCL degradation time on starting molecular weight provides a simple method for tuning degradation in theory, the practical application of this concept results in some

difficulties. For example, based on the degradation time kinetics reported in literature, a PCL system designed to maintain its physical integrity for one year should be comprised of PCL with a molecular weight of 36 kDa.[132] Furthermore, as PCL molecular weight decreases, polymer crystallinity increases, and the ability to cast, handle, and fabricate drug delivery systems from PCL thin films also decreases. For example, 10 kDa PCL may be solvent cast or extruded but results in a thin film that lacks integrity as a free-standing material. A 45 kDa PCL film can be cast but as the film tends to be more fragile than an 80 kDa film, there are often failures during device handling and processing. These factors limit the ability to independently tune degradation of a PCL drug delivery system without compromising other device properties.

In efforts to decrease the time to degradation of PCL devices, a variety of methods have been explored.[138–142] For example, PCL-PLA co-polymers, and blends of PCL and PLA have a faster time to degradation than equivalent neat PCL films.[140] Blends of PCL and PLA also showed significantly improved mechanical properties, such as greater tensile strength and elongation at break.[140] Co-polymerization of PCL with PLA or poly(ethylene glycol) (PEG) have also been used to tune degradation of drug delivery systems.[142] In addition, the effect of blending high molecular weight PLA with lower molecular weight PLA on drug release has been explored.[141,143] This study showed that introducing low molecular weight PLA increased the rate of drug release from PLA films and microspheres compared to those made from unblended high molecular weight PLA. However, to our knowledge, there have not been reports studying the effects of PCL blending on drug diffusion through PCL thin films. Considering inflammatory responses associated with PLA and PGA, which are often blended with PCL, there is great merit to a method that allows fabrication of PCL thin film with reduced time to fragmentation without requiring a secondary polymer.[144,145]

We also noted that both number (M_n) and weight (M_w) average molecular weight have been used to evaluate degradation of PCL or blends of PCL and PLA. In the case of blended polymers, their composite M_n and M_w values can be calculated using **Equations 3 and 4** shown below, which can be derived from the definitions of M_n and M_w.[132,138–140,146]

$$M_{n,blend} = \frac{1}{\sum_i \frac{w_i}{M_{n,i}}} \qquad \text{Eq. 3}$$

$$M_{w,blend} = \sum_i w_i M_{w,i} \qquad \text{Eq. 4}$$

Where w_i is the mass fraction of polymer i included in the blend, and $M_{n,i}$ and $M_{w,i}$ are the number average and weight average molecular weight of polymer fraction i. When blending disparate PCL compositions (e.g. an M_n of 10kDa and 80kDa), it is possible to obtain an effective M_n between either component (**Figure 2-7**), but due to the biomodal nature of the blends, the polydispersity will increase dramatically (**Figure 2-8 A-B**). Considering the increased PDI of blended PCL, we explored the relevance of M_n and M_w of PCL blends in determining the time to fragmentation which, despite the difference in implications of the two measurements, they are often reported interchangeably.

In light of the constraints on device fabrication with low molecular weight PCL we investigated degradation and thin film fabrication of using blends of widely available PCL stocks. We demonstrate that the decay rate of the M_n of PCL under accelerated conditions and the permeability of films to small molecules are unaffected by blending, providing a simple and predictable approach to tune the lifetime of PCL implants. We also show that incorporating high

molecular weight PCL increases the ultimate tensile strength of the film compared to unblended PCL film with the same M_w.

2.3 Materials & Methods

All materials were obtained from Sigma-Aldrich (St. Louis, MO) unless otherwise noted. Statistics were performed using a two-tail Student's t-test or one way ANOVA. Data is reported as mean ± one standard deviation.

PCL film fabrication & characterization: Films were draw-casted onto a glass surface using a multiple clearance square applicator (Paul N. Gardner Company, Inc., Pompano Beach, FL) with applicator height of ~150 µm (0.006 in) from 150 mg/ml solutions of PCL in 2,2,2-trifluoroethanol (TFE). A range of PCL solutions were prepared by blending varied mass fractions of commercially available PCL with M_n of 80 kDa, 45 kDa, and 10 kDa.   lists the mass fractions of each PCL film used in this study. PCL film thickness was measured using a micrometer (iGaging, San Clemente, CA) with 1 µm resolution. All films used in this study had a thickness of 11±1 µm.

Accelerated degradation: Films were cut into pieces roughly 3x3 cm (~10 mg of polymer), fully submerged in 5 mL of 4 N formic acid, and incubated at room temperature on an orbital shaker. At 1, 2, 4, and 5 weeks after the start of the study, PCL film samples (n=4 for each time point)

were removed from the formic acid solution, rinsed thoroughly in Milli-Q deionized water, dried

in a vacuum chamber, weighed, and stored under ambient conditions until further analysis.

GPC analysis: PCL molecular weight distributions were determined via gel permeation

chromatography (GPC) (1260 Infinity Quaternary LC System, Agilent Technologies, Santa

Clara, CA). An isocratic method with tetrahydrofuran (THF) (VWR, Radnor, PA) as the running

buffer was used with a series of four Styragel® THF GPC columns (HR5/WAT0554460,

HR4/WAT044225, HR2/WAT044234, HR0.5/WAT044231; Waters Corporation, Millford, MA)

and a refractive index detector (RID). A flow rate of 1 mL/min was used. Molecular weight

analysis was completed using a universal calibration method based on polystyrene standards.[147]

Diffusion studies: PCL thin film reservoir devices were fabricated utilizing a modified

TransWell® model and loaded with drug as shown in **Figure 2-1**. Two prototypical small

molecules with similar molecular weight and structure but different logP were utilized to

evaluate permeability of PCL films: atenolol (MW 266 Da, logP 0.16) and timolol maleate (MW

316 Da, logP 1.83). PCL films were cut using a 10 mm biopsy punch, and affixed to the bottom

of TransWell® inserts using a silicone adhesive, and allowed to fully cure at room temperature

overnight. A concentrated drug solution (1 mg/mL) fully solubilized in PBS was placed in the

upper chamber, and enough pure PBS was placed in the bottom chamber to eliminate any

competing convective forces due to a hydrostatic pressure imbalance. After 24 hr, the fluid in the

bottom chamber was sampled and stored at 4 ºC until analysis. Drug concentrations in samples

were determined via ultraviolet absorption analysis on a SpectraMax plate reader (Molecular

Devices, Sunnyvale, CA) based on a standard curve. Mass flux rates were calculated using the

equation for diffusion through a thin film from a constant activity source (**Equation 5**).[75]

$$J = \frac{A \times P \times C_R}{L} \qquad\qquad \text{Eq. 5}$$

Where J is the mass flux of drug across the membrane of the transwell insert, A is the surface

area of the membrane (0.33 cm^2), and P is the permeability of the drug into and through the

polymer phase (in cm^2/sec), C_R is the concentration of drug in the upper chamber, and L is the

thickness of the membrane.

Scanning electron microscope (SEM) imaging: Imaging of blended films was performed using a Carl Zeiss Ultra 55 Field Emission Scanning Electron Microscope (Carl Zeiss, San Francisco, CA) with an electron high tension (EHT) emission voltage of 3 kV and a secondary electron (SE2) detector. The samples were coated with 10 nm of gold palladium using a Cressington-HR sputter coater (Cressington, Watford, UK).

Mechanical testing: Mechanical testing was performed by Westpak, Inc. (San Jose, CA) based on the general guidelines of ASTM D882-12: Tensile Properties of Thin Plastic Sheeting using a Shimadzu load frame (AG-I/50N – 10kN) and a 1 kN load cell (SLBL-1kN) (Kyoto, Japan). All films (n=3 per condition) were measured with a jaw separation rate of 13 mm/min, except films 1 and 2 that used a rate of 508 mm/min.

2.4 Results

PCL film mass characterization

There was no significant mass loss observed for PCL films under accelerated degradation conditions up to time of fragmentation. Any changes in recorded mass were within the error of the analytical balance. A lack of mass loss during accelerated degradation indicates bulk degradation of PCL blends, as expected based on literature reports.[132,133]

Molecular weight distributions and degradation profiles of PCL blends

Figure 2-2 compares molecular weight distributions of PCL with various compositions of equivalent M_w, as measured by GPC. **Figure 2-3** shows the evolution of molecular weight under

accelerated degradation conditions for selected blends. A good fit to **Equation 1** ($R^2 =$ 0.93±0.05) and **Equation 2** ($R^2 = 0.96±0.04$)) shows that degradation of PCL under accelerated conditions can be modeled equivalently well using either first-order kinetics or constant-rate kinetics, as expected from previous studies ($p > 0.1$, n=9 measurements per group).[132,134,138]

  describes the blend compositions tested throughout the study, ranging from M_w of 120 to 27 kDa. PCL blends with M_w below 27 kDa were not explored further as they fragmented immediately following casting and were not viable for fabrication applications. Since the M_w and M_n can vary substantially for blends derived from the same source polymers (**Figure 2-8 A-B**), identifying the correct parameter that predicts time to fragmentation was critical. Interestingly, over time, the polydispersity index of the polymer samples (calculated as M_w/M_n) approached ~2 for all polymer blends (**Figure 2-8 C**). Using the observed point of fragmentation in conjunction with SEM analysis, we concluded that the M_w of PCL blends is the relevant parameter in determining time to fragmentation. This follows from the mathematical construction of M_w as a measurement of the center mass of a polymer sample, meaning that M_w declines are more sensitive to the loss of high molecular weight structural polymer than M_n measurements. Based on our observations, it appears that film fragmentation correlates with the time the blend M_w reaches approximately 40±1 kDa. We saw that M_w decays uniformly among blends, and can therefore be used in a predictive manner (**Figure 2-10**). SEM imaging of films that reached an M_w of approximately 26.9 ± 0.3 kDa showed indications of bulk fragmentation (**Figure 2-4 A**). Samples composed of 66% and 75% (w/w) 10 kDa PCL blended with 80 kDa PCL were observed to fully fragment by day 35, while blends containing less than 66% (w/w) were still partially intact (**Figure 2-10**) Blended PCL films before and during accelerated conditions imaged at increased magnification, indicated PCL fragmentation on the micro-scale (**Figure 4B**).

In addition, the observed degradation rate was mostly unaffected across blended and unblended

PCL compositions, as shown in the degradation rate constants (k' and k) in . While there was

some variability in rate constants among different blends, the variability lacked correlation with

specific blend composition (**Figure 2-11**).

Film permeability

Figure 2-5 shows diffusion of two drugs through PCL films. Atenolol (**Figure 2-5 A)**

and timolol (**Figure 2-5 B**), both ß-blockers, were chosen as they have similar structures and

molecular weights but have different logP values. As the graph indicates, permeability of drugs

was not significantly different among different PCL films ($p>0.1$), regardless of the specific

composition of the PCL films used as a diffusion barrier.

Mechanical properties of PCL blends

The ultimate tensile strength (UTS) and elastic modulus (E) of blended and unblended PCL films

was measured for films 1 to 11 (**Figure 2-6**). Films 12 and 13 were not tested as they were too

fragile to handle without damaging prior to testing. As expected, ultimate tensile strength of

films generally decreased with decrease in M_w. Additionally, we found that statistically

equivalent ($p<0.05$) UTS could be achieved for blends of 80 kDa or 45 kDa PCL blended up to

50% (w/w) with 10 kDa PCL. Similarly, statistically equivalent E could be achieved for blends

of 45 kDa PCL blended up to 50% (w/w) with 10 kDa PCL.

2.5 Discussion

Degradation under accelerated conditions

Accelerated degradation studies aim to simulate the lifetime of a PCL implant in a matter of weeks. In vivo, unblended PCL implants can last for upwards of years, often much longer than their useful lifespan as a drug eluting implant or other device.[148] If PCL degradation occurs by bulk rather than surface erosion, a decrease in molecular weight should occur over time without a notable loss in mass. The mechanism of bulk erosion results in cleavage of polymer chains throughout the bulk, without significant loss of structure. Conversely, surface erosion is characterized by a reduction in molecular weight at the polymer surface, leading to mass loss, as surface polymer chains become small enough to diffuse away from the bulk material. Therefore, we can conclude that degradation under our accelerated condition occurs via bulk erosion as no noticeable mass loss is observed until fragmentation, which agrees with previously established literature.[132,141]

To use results from the in vitro accelerated degradation studies to predict PCL degradation in vivo, a relationship between in vitro and in vivo rate constants should be established. To establish a comparison, previous literature has established the degradation kinetics of PCL in a sub dermal implant ($R^2 = 0.989$ and $k' = 2.75 \times 10^{-3}$ day^{-1}) by fitting M_n measurements over time to **Equation 1**, resulting in a half-life of 252 days.[132] Considering the average exponential rate constants in this study (0.022 ± 0.005 day^{-1}), we can calculate the average half-life of the PCL under accelerated degradation conditions as 31 days, meaning that one day under accelerated conditions is equivalent to approximately 8 days in vivo. From this relationship, we can predict time to fragmentation of a given PCL film in vivo based on its starting molecular weight.

Degradation of PCL blends

Notably, based on accelerated in vitro degradation studies, the rate of PCL degradation was largely unaffected by differences in molecular weight distribution ( ). Additionally, both autocatalysis and random chain scission proved to be equally effective at fitting experimental results, but not particularly informative as to the actual mechanism of degradation. While only investigated under accelerated conditions in vitro, previously published correlations between accelerated in vitro, in vitro, and in vivo PCL degradation indicate that under appropriate conditions where bulk erosion was observed, the mechanisms and trends in PCL degradation are consistent between accelerated and non-accelerated conditions.[132,133,149] Furthermore, since the degradation rate constant(s) do not change based on PCL blend composition (**Figure 2-3**), blending can be used reliably to tune time to fragmentation by selecting the desired initial molecular weight (M_n), which can be calculated for any arbitrary composition using **Equation 4**.

Furthermore, as noted earlier ( ), M_w and M_n of a blended system can be significantly different, thus a parameter indicative of film fragmentation must be identified. While M_w and M_n values of all tested blends were calculated using **Equation 3 and 4**, our accelerated degradation studies found that a simple average of molecular weights (M_w) was representative of the general trend of PCL degradation. For example, if M_n was the relevant parameter in determining time to fragmentation, films 9 through 13 should exhibit similar fragmentation behaviors as they have very similar M_n values. However, while films 12 and 13 were too fragile for handling during tensile strength testing, films 9, 10 and 11 could be bent and handled without fragmentation. In addition, in accelerated degradation studies, films with the same M_w fragmented together at a similar time point. Our observations were also supported by SEM images of films throughout accelerated degradation (**Figure 2-4 B**).

Film permeability

PCL blends can be used to produce materials with a superior correlation between device lifespan and degradation timeline. Because of an interest in PCL as a drug delivery tool, it is important to understand how differences in PCL molecular weight distribution impact film permeability. We noted that in a previous report on blending high and low molecular weight PLA, a change in diffusive drug release was observed upon blending.[143] Other groups have observed this phenomena with PLA using matrix-type first order diffusion models, however in the case of a zero-order diffusion model looking at PCL, there does not appear to be a difference in permeability between blend compositions. Because our permeability model was not dependent on the solubilization kinetics of the model small molecule or the fluid ingress into the polymer matrix, we expect this to be a good model of the permeability of these polymer systems. As illustrated in **Figure 2-5**, permeability of two small molecules representative of the standard pharmaceutical space (atenolol (logP 0.16) and timolol maleate (logP 1.81)) were not significantly different for blended or unblended PCL films (p>0.1). As shown in the SEM images (**Figure 2-4 B**), microscopically visible imperfections in blended films were not observed until they reached the fragmentation limit. Our results suggest that blended PCL products can be applied as diffusion limiting barriers in an analogous manner to neat PCL materials, without changing the permeability of the film.[148] However, this result will likely need to be validated on a case-by-case basis for APIs of interest.

Tensile strength of PCL blends

To assess our general observation that films made from blends were qualitatively less fragile than unblended films, ultimate tensile strength (tensile strength at break) and the elastic modulus of various blends were compared (**Figure 2-6**). Ultimate tensile strength of 80 kDa PCL film (17.1 ± 0.9 MPa) was similar to what has been reported in literature (ranging from 10.5 to 16.1 MPa for bulk PCL with M_n = 91,900 ± 7,700 Da).[150] Ultimate tensile strength of films with the same composite M_w was always greater when 80kDa and 10kDa PCL were blended (films 7, 9, and 11) compared to when 45kDa and 10kDa PCL were blended (films 6, 8, 10). This is likely due to the presence of longer PCL polymer chains that are able to elongate prior to fragmentation. Interestingly, ultimate tensile strength of unblended 80 kDa PCL film was similar to that of films 2, 5, 7, and 9, which contained 33%, 50%, 67%, and 75% (w/w) 10 kDa PCL respectively. However, once 83% 10 kDa PCL was blended (film 11), ultimate tensile strength of the resulting film was significantly reduced ($p < 0.05$). This result indicated that tensile strength of PCL can remain unaffected with 10kDa PCL blending until a certain blending percentage ($\leq$ 50% w/w). We see that for both tensile strength and elastic modulus, it is possible to produce blends with lower initial M_n and M_w that have equivalent mechanical properties to unblended, higher molecular weight materials. Based on our results above, we can note that degradation kinetics are generally unaffected by the starting material, and that M_w seems to also decrease uniformly across blends (**Figure 2-3** and **Figure 2-9**). This implies that the time to fracture, looking at blends of 80kDa and 10kDa PCL, can be reduced by half without sacrificing mechanical properties. Similarly, for materials derived from blends of 45 kDa and 10 kDa we can freely reduce the time to fracture by ~38% without consequence.

2.6 Conclusion

We show that blending PCL to create binary or ternary molecular weight distribution allows one to create PCL thin film devices with a lower starting molecular weight without changing the polymer degradation rate. Furthermore, we demonstrate that different blended PCL compositions can be used in drug delivery applications as a diffusion barrier without changing diffusive flux. Lastly, our tensile strength testing indicates that low molecular weight PCL can be blended up to a certain mass percentage ($\leq$ 50% w/w) with high molecular weight PCL without impacting ultimate tensile strength. While additional work is needed to validate the degradation timelines of PCL blends *in vivo*, early results demonstrate the utility of this approach for tailoring the design of drug delivery systems, and other PCL based resorbable implants.

2.7: Real Time Biodegradation of GMP Polycaprolactone

Because of the extended lifetime of unblended polycaprolactone, degradation studies are often performed under accelerated conditions. However, these studies are often limited in their ability to directly speak to the lifetime of the material in a biological system. In order to more fully understand how these materials, behave under conditions that replicate a simulated use case, we looked at the real time degradation of two varieties of GMP grade polycaprolactone over the course of 21 months. Devices were either filled with a model excipient (castor oil) or left empty,

and were incubated in PBS with 0.05% (w/w) sodium azide (as a biocide). Samples were taken, dried, and stored for analysis every other month for the first year, and monthly thereafter.

Table 2-1 :
M_w and M_n of various PCL blend combinations and their degradation time constants under accelerated condition. Blends 10-13 were excluded from further analysis due to their poor handleability.

	Mass Fraction						k
	10kDa	45kDa	80kDa	M_w [kDa]	M_n [kDa]	k' [day^{-1}]	[(day*kDa)$^{-1}$ x10^{-4}]
1			1.00	120	80	0.034	6.260
2	0.33		0.67	86	24	0.028	6.521
3		1.00		69	45	0.013	4.438
4	0.33	0.33	0.33	69	22	0.023	5.977
5	0.50		0.50	69	18	0.018	5.388
6	0.33	0.67		52	21	0.008	3.060
7	0.67		0.33	52	14	0.017	5.552
8	0.50	0.50		43	16	0.006	2.628
9	0.75		0.25	43	13	0.013	4.877
10	0.67	0.33		34	14		
11	0.83		0.17	34	12		
12	0.80	0.20		27	12		
13	0.90		0.10	27	11		

Samples were assessed for their molecular weight via GPC and for their percent crystallinity via dynamic scanning calorimetry. We observe that, as expected, the increase in crystallinity is inversely correlated with molecular weight (**Figure 2-11**). We observed that empty tubes began to fail after around 9 months of incubation, while filled devices failed after 12-15 months of incubation, indicating that formulation and form factor might impact degradation timelines.

Additionally, comparing the degradation rates of filled and empty devices, based on molecular weight measurements out to 25 and 12 months respectively, devices filled with a mock castor oil excipient decay 35% slower than empty devices (**Figure 2-12**), suggesting that the form factor and formulation of the device impacts it's degradation, which contradicts previous results that suggested the PCL degradation was independent of device construction or contents.[132,147]
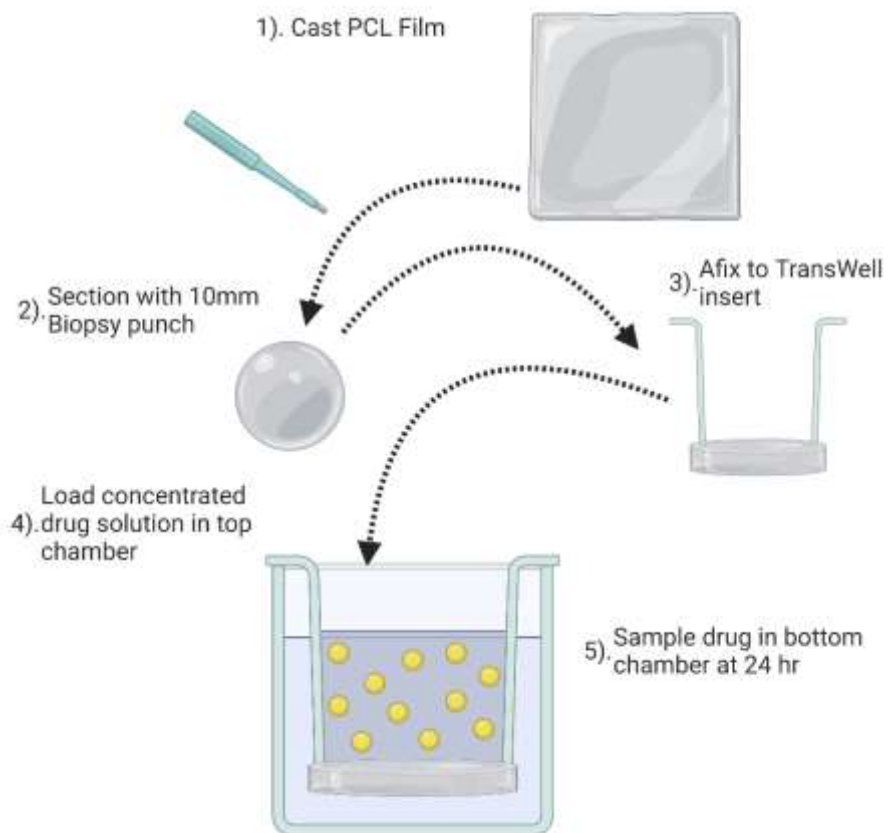
Figure 2-1:
Schematic diagram of thin film PCL diffusion chamber setup. Briefly: Cast films
(1) are cut into 10 mm diameter disks using a biopsy punch (2). Disks are affixed
to the bottom of TransWell cell culture inserts (3) using a silicone adhesive and
allowed to cure overnight. To perform the permeation study, a concentrated drug
solution in an appropriate buffer is placed into the top chamber (4). The bottom
chamber is filled to the same height to prevent pressure driven transport. After
24hr, the solution in the bottom chamber is removed and analyzed for the presence
of the molecule of interest (5). Produced under license from Biorender.com.
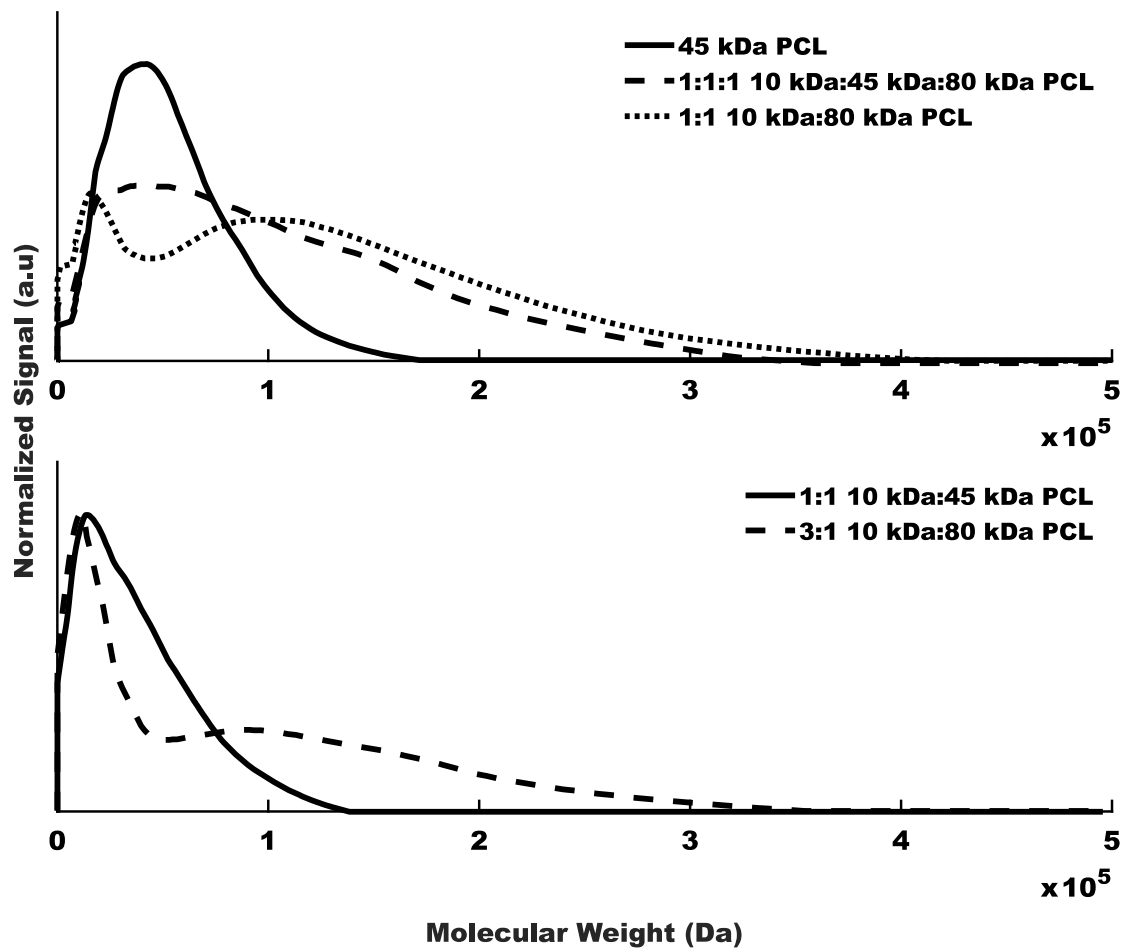
Figure 2-2:
Molecular weight distributions of PCL blends with (Top) M_w = 69 kDa and (Bottom) M_w = 43 kDa normalized to the area under the curve (concentration of polymer in sample solution). Data shows representative traces from the indicated blends.
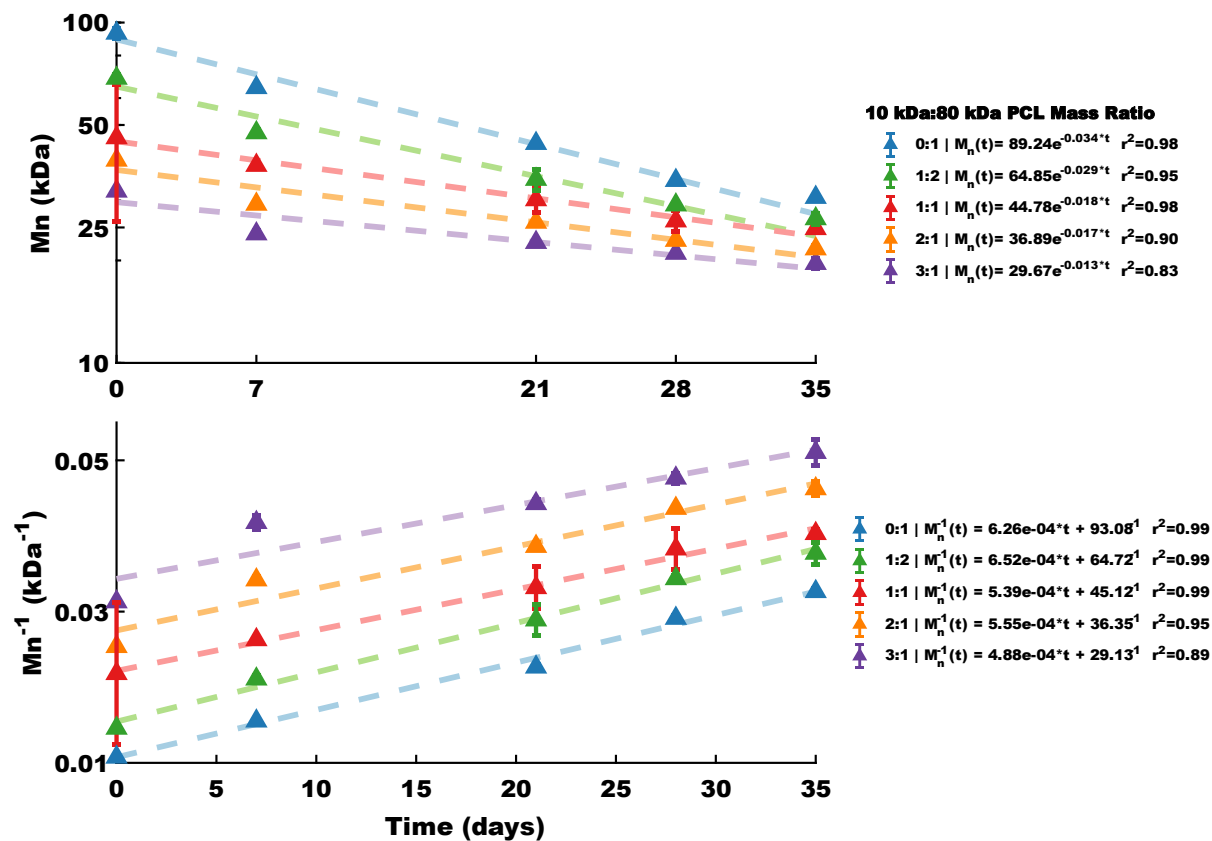
Figure 2-3:
M_n reduction of PCL blends under accelerated degradation conditions. Triangles show experimental data (mean ± 1 SD, n=4 for all groups). Dashed lines show fit to a (A) Equation 1 and (B) Equation 2 for the indicated blends, expressed as mass ratios of 10 kDa and 80 kDa PCL. Data represents the mean ± 1 SD of four separate measurements. Fitting parameters can be found in .

A.
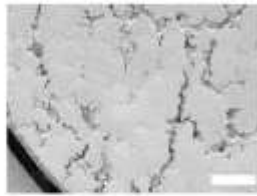
B.
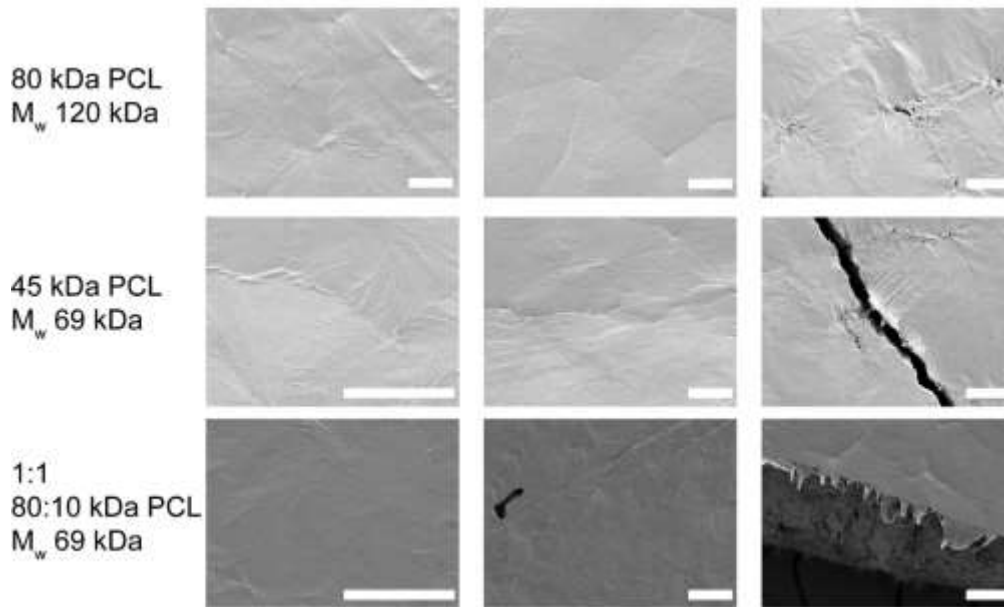
Figure 2-4:
SEM images of (A) a film that reached fragmentation limit (film 12 upon casting) and (B) blended PCL films before and during accelerated degradation up to 5 weeks. In A, scale bar = 100 μm. In B, scale bar = 10 μm.
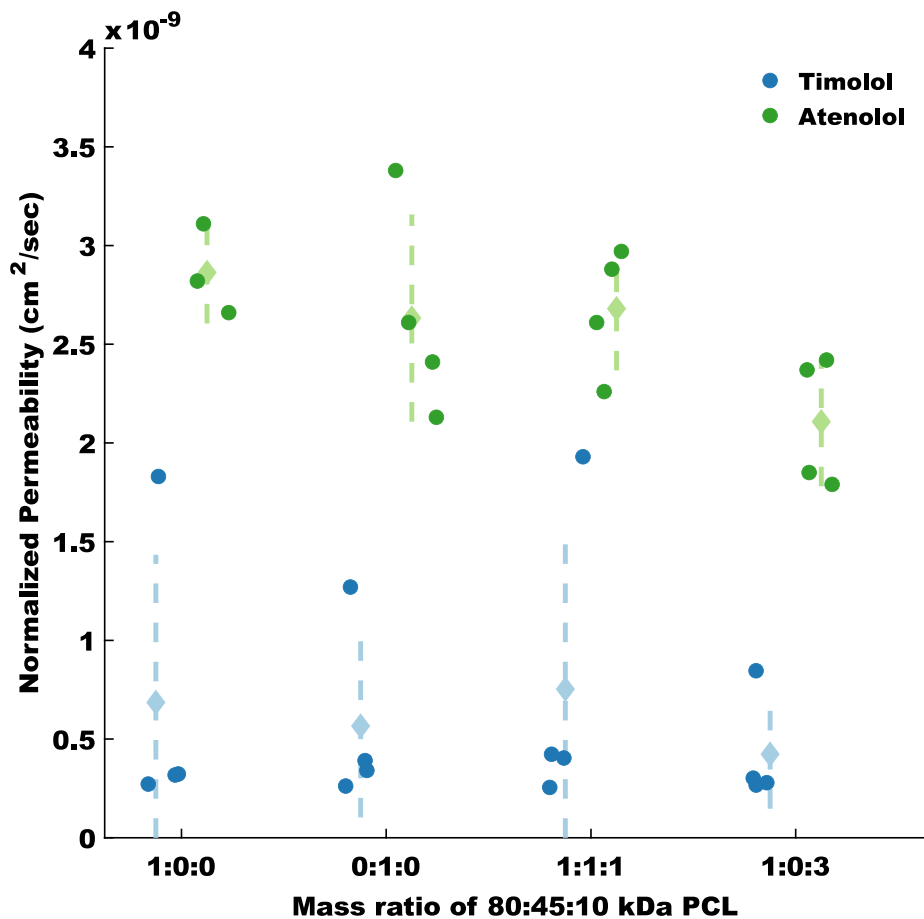
Figure 2-5:
PCL film permeability for a low logP pharmaceutical (atenolol, logP 0.16) and a high logP pharmaceutical (timolol maleate, logP 1.81). Solid diamonds represent the mean of the measurement, and the dashed lines represent the 95% confidence interval of the measurement. n= 3 for 1:0:0 blend Atenolol, n=4 for all other measurements.
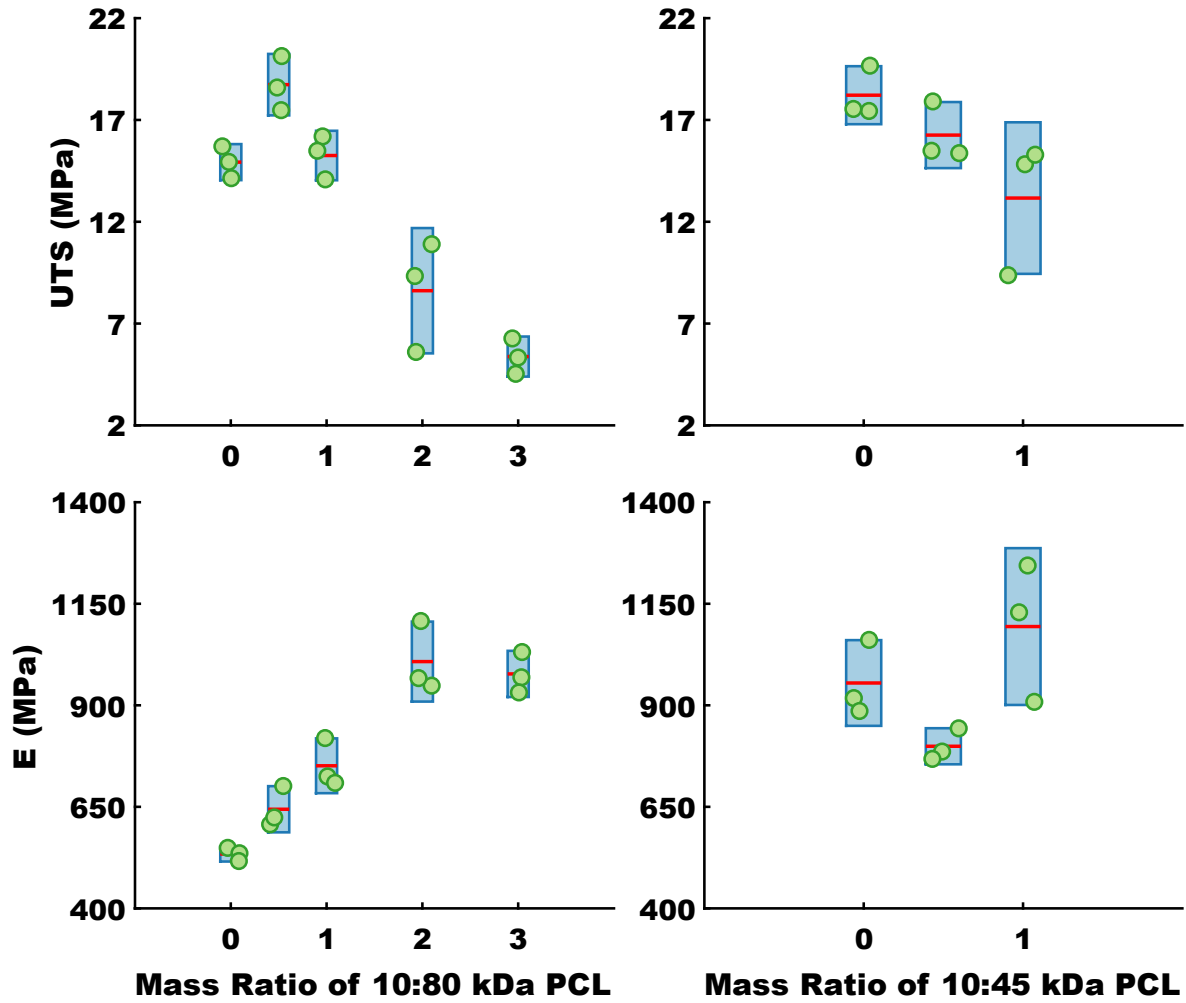
Figure 2-6:
Ultimate tensile strength (UTS) and elastic modulus (E) of PCL blends obtained by tensile strength testing. Blue bars represent 95% confidence intervals of the observed mean, green circles represent replicate observations, and red lines represent the arithmetic mean of n=3 measurements per film group.
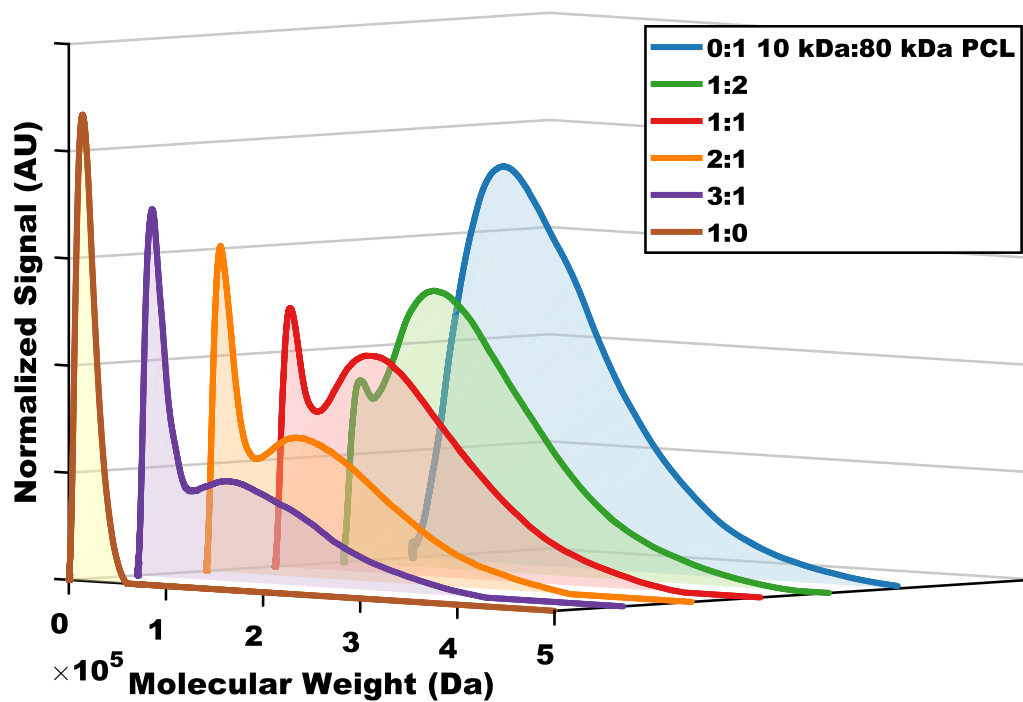
Figure 2-7:
Molecular weight distributions for the indicated mass ratio bends of 10 kDa and 80 kDa PCL prior to accelerated degradation
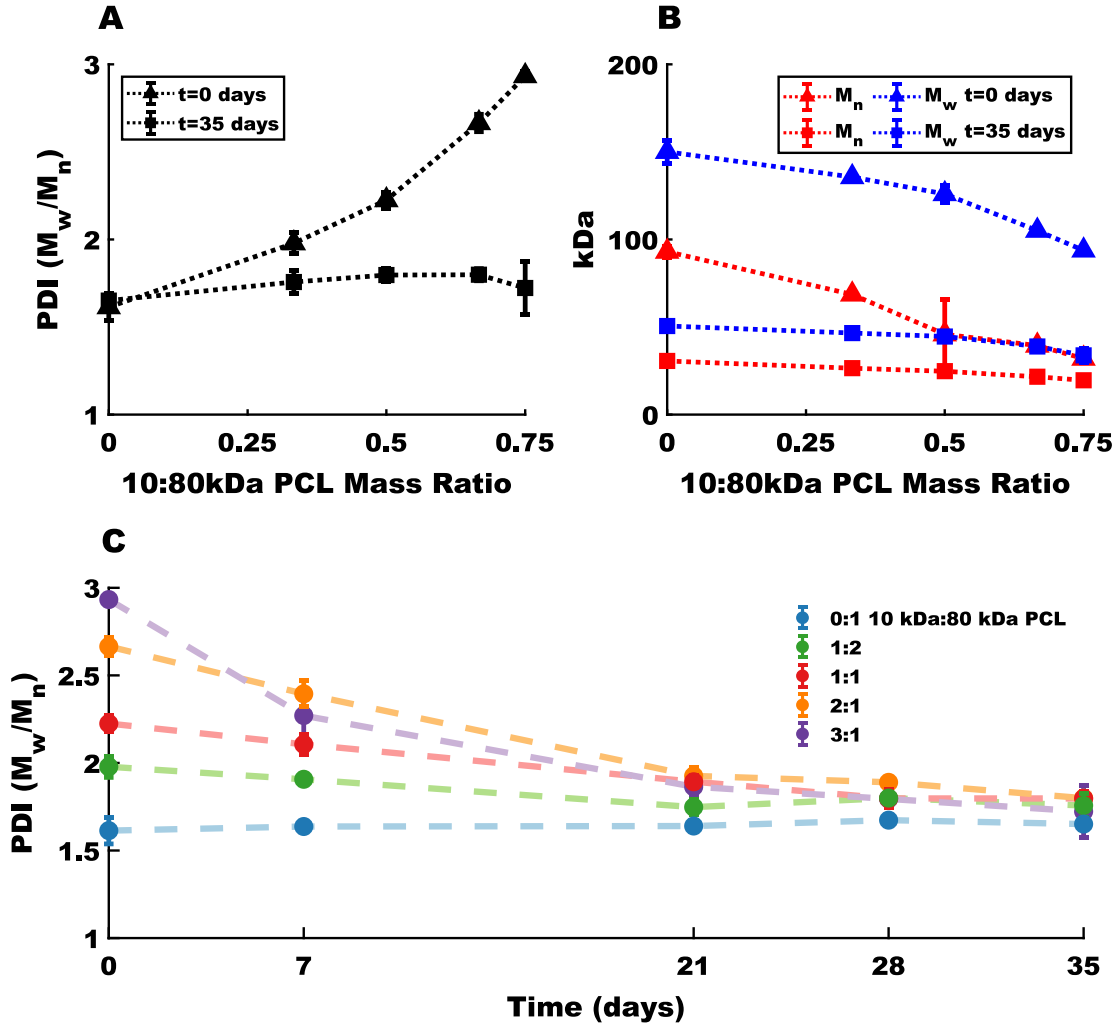
Figure 2-8:
Changes in polydispersity as function of time and starting polymer composition. (A) The polymer polydispersity index (PDI) at the begging of the accelerated degradation study (time = 0 days, triangle markers) contrasted with the PDI at the conclusion of the study (time = 35 days, square markers) vs the initial polymer composition. (B) M_n (red lines) and M_w (blue lines) plotted against the initial polymer mass fraction at day 0 (triangles) and day 35 (squares). (C) PDI plotted against time for the indicated polymer blends, presented as mass ratios of 10 kDa to 80 kDa PCL. All data plotted as mean ± SD of n = 4 independent trials.

45
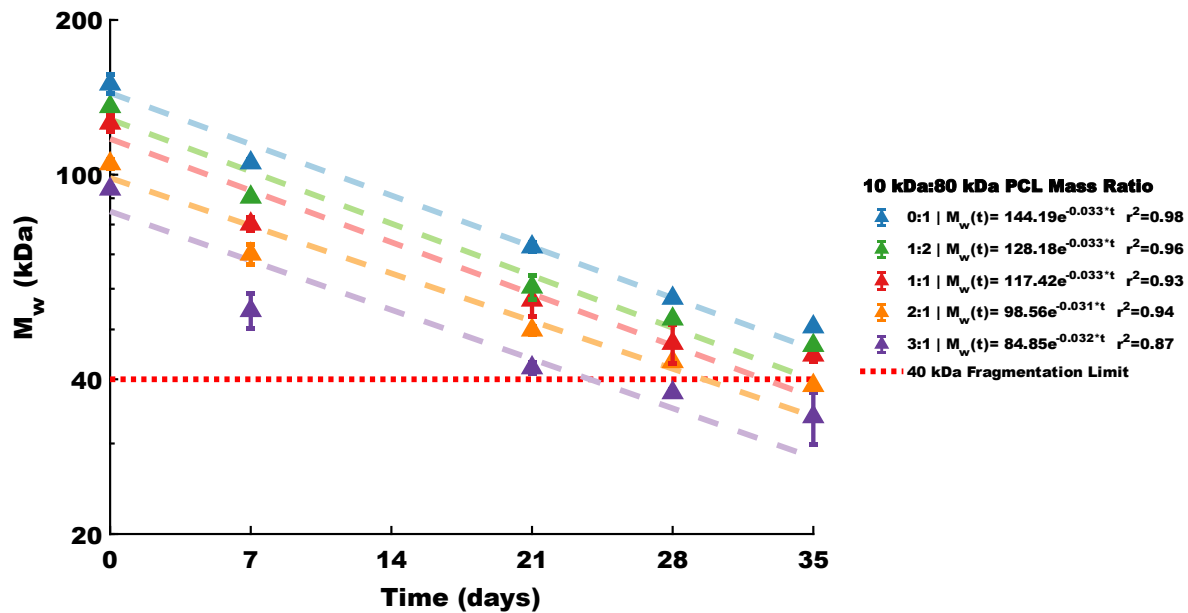
Figure 2-9:
Weight average molecular weight over time, plotted with a fit to a single exponential decay model as shown. The dashed red line indicates the observed $M_w = 40$ kDa fragmentation point. Blends presented as mass ratios of 10 kDa to 80 kDa PCL. Data presented as mean ± SD of n = 4 independent trials.
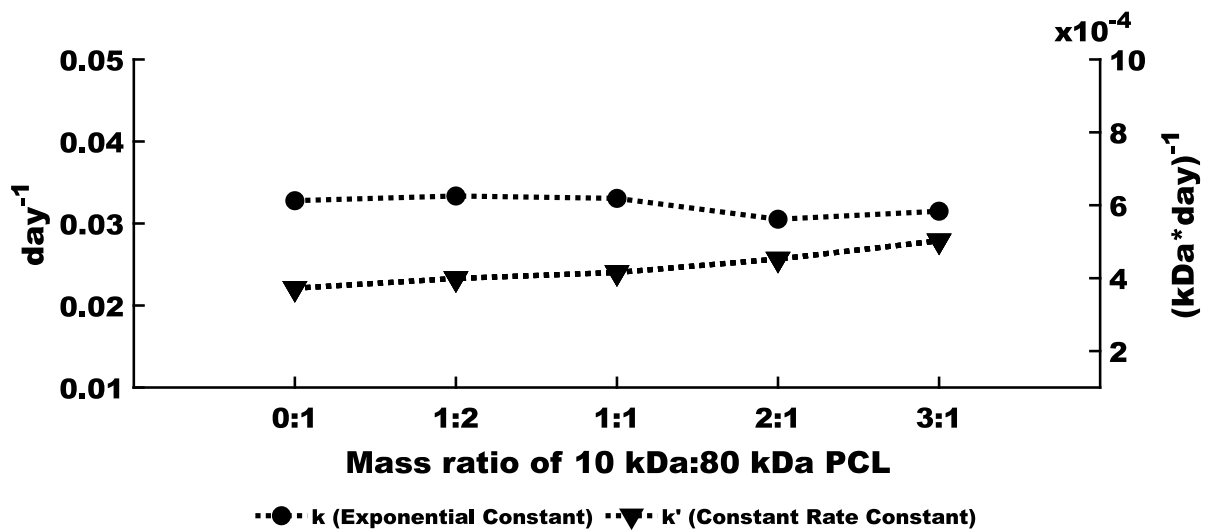
Figure 2-10:
Empirical constants derived from fitting PCL degradation curves to **Equation 1 and 2**, plotted against film blend composition
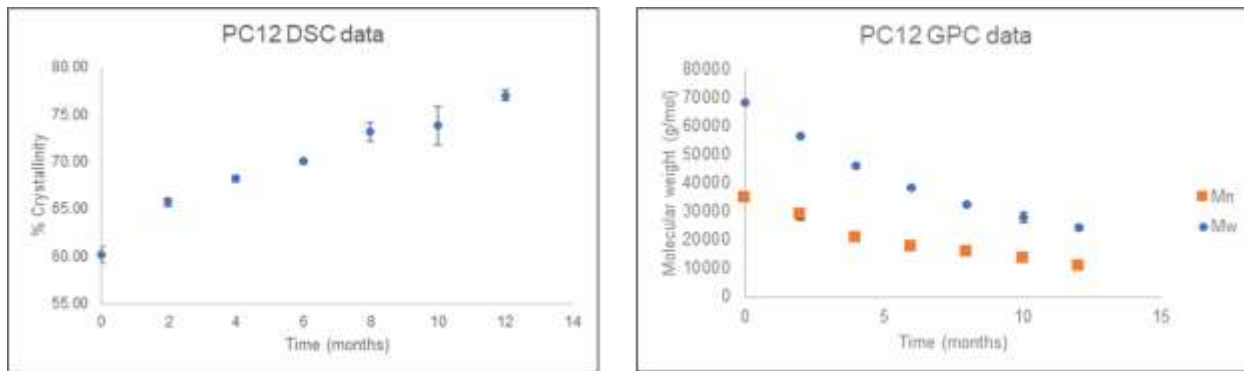
Figure 2-11:
Crystallinity and molecular weight measurements form empty tubes from real time biodegradation study over the course of 12 months. Data is representative of the mean ±1 SD of 4 independent samples.
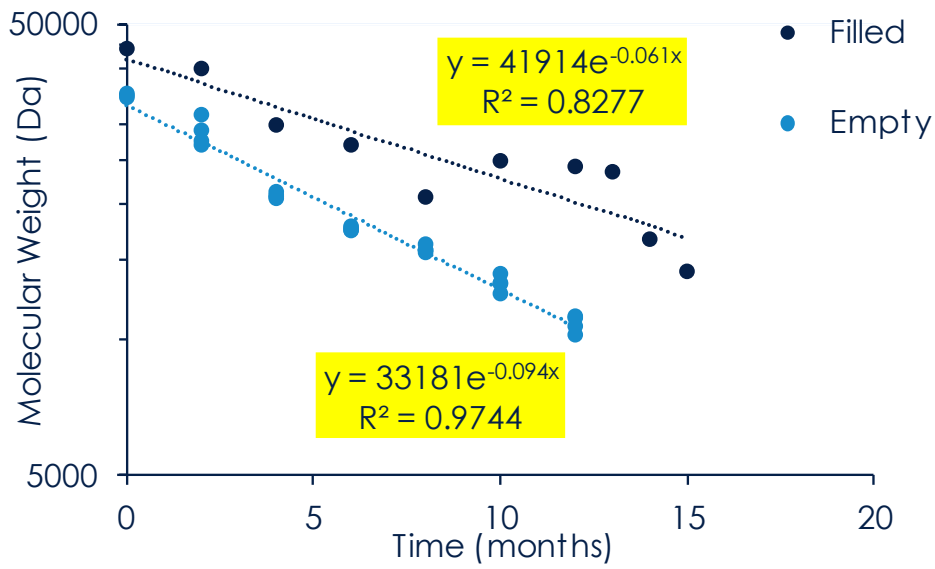
Figure 2-12:
Incorporation of formulation agents impacts device degradation rate. Plotted molecular weight measurements fit to a single exponential decay model over the course of 15 months. n=3 measurements per time point for empty devices, and n=1 measurement per time point for filled devices. Based on time constants, filled devices degrade 35% slower than empty devices.

Chapter 3 - Bottom-Up Fabrication of Multilayer Enteric Devices for the

Oral Delivery of Peptides

3.1 Abstract

Purpose: To develop a planar, asymmetric, micro-scale oral drug delivery vehicle by i) fabricating microdevice bodies with enteric materials, ii) efficiently and stably loading sensitive drug molecules, and iii) capping microdevices for controlled drug release. *Methods*: Picoliter-volume inkjet printing was used to fabricate microdevices through additive manufacturing via drop-by-drop deposition of enteric polymer materials. Microdevice bodies with reservoirs are fabricated through deposition of an enteric polymer, Eudragit FS 30 D. A model API, insulin, was loaded into each microdevice and retained its stability during printing and release. Eudragit L 100 and/or S 100 were used to cap microdevices and control the kinetics of insulin release in simulated intestinal conditions. *Results*: Microdevice morphologies and size can be tuned on the fly based on printing parameters to span from the microscale to the mesoscale. Insulin retained its stability throughout device fabrication and during *in vitro* release in simulated intestinal conditions. Insulin release kinetics, from burst release to no release, can be tailored by controlling the blend of the Eudragit capping material. *Conclusion*: This approach represents a uniquely scalable and flexible strategy for microdevice fabrication that overcomes limitations in loading sensitive biologics and in the tunability of device geometries that are inherent to traditional microfabrication strategies.

3.2 Introduction

Oral drug delivery is preferred by both providers and patients as a method of therapeutic administration due to ease of use and high patient compliance [151]. Despite many advances in oral delivery systems, peptides and proteins are restricted to parenteral administration due to their high molecular weight, degradation by proteolytic enzymes, and extreme pH conditions in the gastrointestinal (GI) tract. Limited permeability across the GI mucosa further exacerbates the problem leading to oral bioavailabilities of less than 1% [152–154]. Therefore, there is a need for innovative delivery systems that can simultaneously protect the sensitive protein cargo while improving the oral bioavailability of the active pharmaceutical ingredient (API).

Lipid and polymer micro/nano-particles have been used to improve the dispersion of APIs with low solubility in the GI tract and to protect encapsulated materials against pH and enzymatically driven proteolysis to improve the efficiency of oral delivery [155,156]. However, these spherical particles release the encapsulated drug omni-directionally, which is inefficient and leads to reduced local concentration of drug molecules at the apical surface of the intestinal epithelium where the absorption process occurs, resulting in a lower overall oral bioavailability [155].

To overcome these delivery challenges, many groups have turned to a microtechnology approach [156]. Microfabrication has traditionally been used in the semiconductor industry to create structures on the size scale of one micron or smaller [157]. Microfabrication principles have also been heavily employed in advancing healthcare technologies including the fabrication of microneedle arrays for dermal drug delivery, microfluidics devices for organ on a chip systems, and micro-machined particles for oral administration [155,158,159]. Our group and others have demonstrated the use of fabricated micron-scale devices with customized size, geometry, and aspect ratios to overcome the anatomical and physiological barriers impeding oral drug delivery [156,160]. The

majority of these fabrication approaches have utilized conventional materials such as poly(methyl methacrylate), SU-8, silicon, or polydimethylsiloxane for the encapsulation of therapeutic molecules [160–162]. However, the safety and compatibility of these materials for clinical use, particularly via the oral route, have not been confirmed, which presents a significant regulatory barrier limiting the translation of these microdevice products to the clinic [163].

Additive manufacturing, a potential microfabrication alternative, describes a broad range of processes that involve the layer-by-layer assembly of 3D structures. Based on the desired application, additive manufacturing can be applied to a number of different materials, including plastics, metals, and photo-crosslinkable resins [164,165]. Compared to traditional microfabrication approaches, additive manufacturing offers flexibility in scaling device parameters and speed of iterations [164,166]. Most current approaches that utilize additive manufacturing to produce pharmaceutical products, including *Levetiracetam®* from *Aprecia,* use a binder jetting technique to achieve rapidly dissolving 3D structures to improve the ease of use and onset time [167–169]. This is achieved through sequentially depositing a water-soluble binder onto a powder bed dispersion of the API and other formulation agents. However, this strategy is not amenable for controlled or delayed release formulations because of the lack of a diffusion-limiting layer. To develop controlled or delayed release formulations using additive manufacturing, other groups have demonstrated the use of a continuous or drop-on-demand material jetting approach, using filaments composed of API and polymer [169]. One limitation of translating these strategies is the reliance on hot-melt extrusion to homogenize APIs and formulating polymers into the desired form factor with the required mechanical properties. This limits the API selection to molecules that can survive relatively high temperatures or APIs that are miscible with low melting temperature binding materials [170,171].

Materials and techniques used in the fabrication of oral protein/peptide delivery systems must maintain the stability of their cargo during fabrication, processing, and administration. Among the most common materials used in the controlled oral delivery of APIs is the Eudragit family of polymers. Eudragit polymers contain a range of linear methyl methacrylate polymers with differentiated pH-sensitive dissolution based on the ratio of acrylate groups to free carboxylic acids. Eudragit polymers are ideal for oral protein delivery due to their extensive characterization and their ability to be processed without harsh organic solvents or excessive heat [172,173].
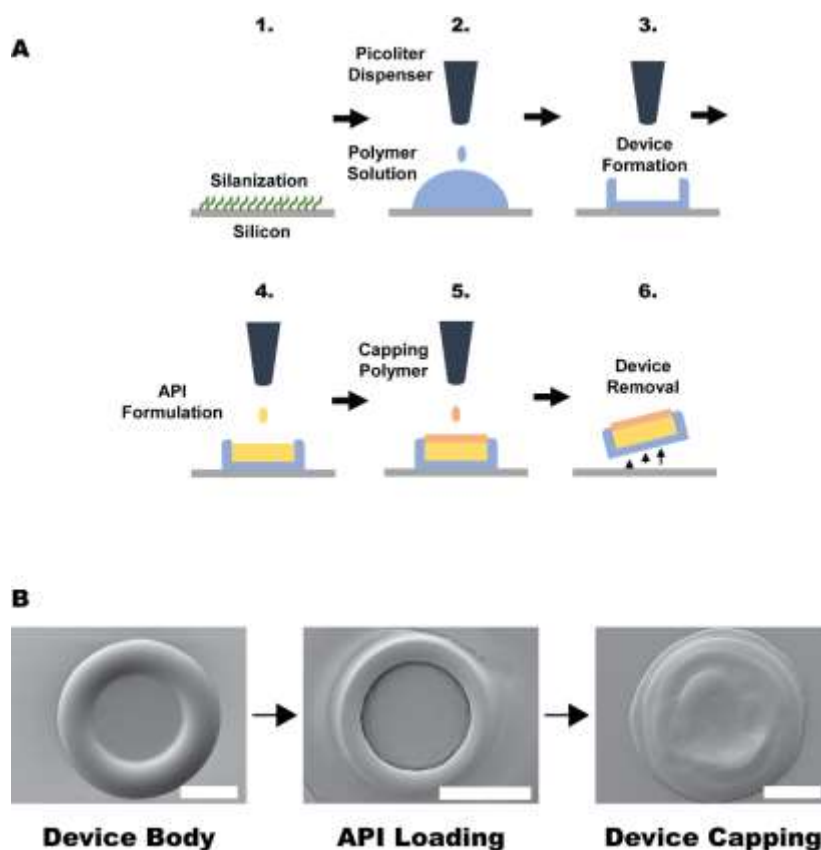
Figure 3-1:
Schematic of the printing process. A silicon wafer is silanized to achieve a hydrophobic surface. The polymer dispersion is ejected from the picoliter dispenser onto the silicon wafer. Evaporation of solvent results in the formation of device body. The dispenser is then used to print API formulation into each device. After devices are loaded with API, a second polymer is printed on top of devices to form a cap. Devices can then be removed from wafer for use. (B) Scanning electron microscopy (SEM) images of representative devices throughout the fabrication, loading, and capping process. All scale bars are 100 µm

Our approach is similar to a drop-on-demand additive manufacturing system and inkjet printing, where APIs and enteric coatings are additively assembled in a dropwise, layer-by-layer process to achieve micron scale, multilayer structures [174]. Similar techniques have been applied for more than a decade in the commercial scale fabrication of DNA and RNA microarray chips [175,176]. Because our approach utilizes piezoelectric-based droplet formation of aqueous solutions, there is no sample heating, enabling us to deposit biologics and other heat-sensitive materials [177–179]. First, Eudragit FS 30 D is deposited onto a silicon wafer and evaporated utilizing the "coffee-ring" drying effect to form concave device bodies. Next, solutions of insulin as a model peptide API are deposited into the wells of the device bodies, resulting in loaded devices. Compared to alternative strategies for microdevice loading (e.g. super critical impregnation, hot embossing, spray coating, spin coating, or powder filling), droplet inkjet printing has dramatically reduced drug waste and is amenable to many APIs [162,180–185]. This makes inkjet printing the ideal method for loading costly but soluble protein and peptide therapeutics as our group and others have shown previously [177–179,186]. Finally, we are able to fully encapsulate APIs in multiple capping layers of enteric polymer, enabling controlled and delayed release of APIs, tunable to the desired pharmacokinetic profile. This strategy also enables on-the-fly tuning of device parameters, including device size, the mass of API and capping material deposited, and the capping material formulation. This allows for greater flexibility and adaptability compared to traditional microfabrication approaches that rely on costly photomasks and replica molding equipment.

3.3 Materials and methods

Materials

Lyophilized recombinant human insulin (CAT: 91077C), hydrochloric acid (HCl), HPLC grade trifluoroacetic acid (TFA), HPLC grade acetonitrile (AcN), ethyl alcohol, simulated intestinal fluid

(SIF) and trichloro(1H,1H,2H,2H-perfluorooctyl)silane were purchased from Sigma-Aldrich (St. Louis, MO). Triethyl citrate (TEC) was purchased from Thermo Fisher Scientific, USA. Eudragit FS 30 D, S 100 and L 100 were graciously provided by Evonik Industries (Essen, Germany). 3'' silicon wafers were purchased from Addison Engineering Inc, USA. India Ink was purchased from KOH-I-NOR (Bloomsbury, NJ).

Microdevice reservoir fabrication

The overall fabrication, loading, and capping process is shown in **Figure 3-1 A**. First, a silicon wafer was oxygen plasma treated for 3 min at 50 W followed by silanization with trichloro(1H,1H,2H,2H-perfluorooctyl)silane via vapor deposition under vacuum at room temperature for 25 min. India ink stock was diluted 10-fold with deionized water. Eudragit FS 30 D dispersion was diluted with deionized water to form a 5% (w/v) solution with 0.5% (w/v) TEC. All solutions were filtered through 0.22 µm polyvinylidene difluoride (PVDF) syringe filters (Millipore, Burlington, MA). All microdevices with reservoirs were fabricated using a sciFLEXARRAYER S3. Prior to printing devices, India Ink was aspirated into the dispenser nozzle and was used to print fiducial markers on the silicon wafer. The FS 30 D formulation was then aspirated into the dispenser nozzle, which was aligned to the fiducial markers, to begin printing the microdevices. Voltage, pulse width, and frequency parameters were optimized to obtain drops with volumes of ~400 pL. To form the microdevice body, a specific amount of solution was spotted on the wafer and allowed to air dry. Total volume of dispensed droplets was controlled by the number of drops dispensed. Drop volumes of 10, 20, 40, 80, and 160 drops were used. Furthermore, the stage holding the wafer was temperature controlled. Tested temperatures included 14°C, 16°C, 18°C, 20°C, and 22°C. Relative humidity was maintained between 50-55% in the printing chamber. Each 3'' silicon wafer was printed with an array of 26×26 microdevices

for a total of 676 devices and was baked post-printing at 100°C for 20 min. The height profile of microdevices was measured using an Ambios Technology XP-2 profilometer.

For stability studies, wafers with printed devices were diced into smaller sub-quadrants containing 169 devices. Each quadrant was placed into a petri dish and exposed to SIF for 60 to 90 min at 37°C on an orbital shaker. Samples were removed and rinsed with deionized water to remove salts from solution before being dried under a stream of dry N_2 gas. Dried samples were then mounted and prepped for scanning electron microscopy (SEM) imaging.

Insulin loading

Insulin solution was prepared fresh at 10 mg/mL in 10 mM HCl and filtered through a 100 kDa centrifuge tube for 5 min at 5000 RCF (Pall Corp, New York, New York). Insulin printing was performed using the sciFLEXARRAYER S3. Prior to printing, drug solution was aspirated into the dispenser nozzle. During setup, the printer's control unit was aligned to the fiduciaries on the silicon wafer, which enabled programmable automatic dispensing. The stage temperature was set to 22°C. Parameters were optimized to obtain drops with volumes of ~400 pL as described earlier. A sufficient volume of insulin solution was printed into device reservoirs to maximize loaded volume inside the reservoir and minimize solution spillover. The printing process was performed in multiple cycles to allow the solvent to completely evaporate between each cycle. Microdevices were loaded with ~100 ng insulin per device and stored under desiccated conditions at 4°C until further use.

Fabrication of a sealing cap

Eudragit L 100 and Eudragit S 100 were dissolved in ethyl alcohol at 1% (w/v) with 0.1% (w/v) TEC and filtered through 0.22 µm PVDF syringe filters. Microdevice capping was performed using the sciFLEXARRAYER S3. The printer was primed with ethyl alcohol prior to printing, and

the stage temperature was set to 22°C. The system was aligned to the fiduciaries on the silicon wafer as described earlier. Parameters were optimized to obtain drops with volumes of ~300 pL. Either Eudragit L 100, Eudragit S 100, or a 1:1 blend was aspirated into the nozzle and a sufficient amount of 300 pL drops was dispensed onto each device to form caps. The printing process was performed in multiple cycles to allow the solvent to completely evaporate between each cycle. Devices were capped with between 200 ng to 220 ng of material, depending on the diameter of the device. Capped microdevices were stored under desiccated conditions at 4°C for further use.

Morphology of planar microdevices

A Carl Zeiss Ultra 55 field emission scanning electron microscope (Carl Zeiss, Oberkochen, Germany) was used to assess the morphological and structural characteristics of the microdevices, before and after printing, API loading, capping, mechanical removal from the silicon substrate, and before and after exposure to SIF. Prior to imaging, devices adhered to a silicon wafer were mounted on aluminum stubs using conductive carbon tape (Ted Pella, Redding, CA) and desiccated under vacuum overnight. Devices were sputter coated with 20 nm of gold, imaged at a 10° tilt and a 2 keV accelerating voltage with magnifications ranging from 150x-250x.

Characterization of insulin release

Insulin release from uncapped and capped sub-arrays, each containing a total of 169 microdevices, was performed by incubating the devices in SIF for 5, 15, 30, and 60 min, on an orbital shaker at 37°C. Samples were then analyzed using high-performance liquid chromatography (HPLC). Insulin release was quantified using a 1260 Infinity Quaternary LC System (Agilent Technologies, Santa Clara, CA) using a 50x2.0 µm Proto 200 C18, 5 µm column (Higgins Analytical, Mountain View, CA) at room temperature with a 100 µl injection. Insulin was detected at 214 nm using an MWD. Quantification was performed using a reverse-phase HPLC method where mobile phase

(A) is deionized water with 0.1% (v/v) TFA and mobile phase (B) is HPLC grade acetonitrile with 0.08% (v/v) TFA. For min 0-50, the fraction of mobile phase A decreased linearly from 100% to 0% and maintained from min 50-55. In min 55-60 the mobile phase A fraction increased from 0% to 100% and maintained until min 70. Between samples, the autosampler was dip washed in methanol. Insulin was observed to elute at 19.1±0.1 min.

3.4 Results

Microdevice integrity and need for plasticizer

Device bodies were fabricated from Eudragit FS 30 D, a low viscosity aqueous anionic polymer dispersion developed for colonic delivery and dissolution at pH $\geq$ 7.0 [172]. Eudragit FS 30 D was
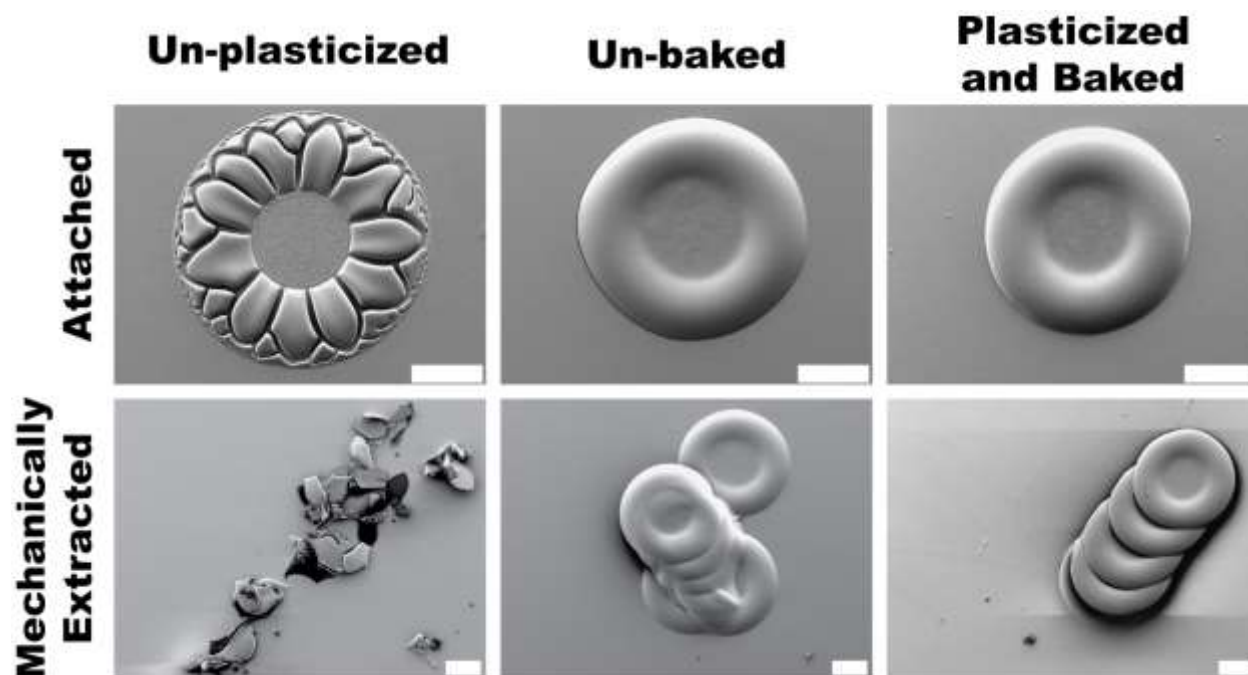
Figure 3-2:
SEM imaging shows microdevices are robust against mechanical extraction from a silicon substrate with the addition of a plasticizing agent and a bake step. Devices printed without the addition of a plasticizing agent (Left) have a roughened morphology and are prone to shattering upon removal. Devices that are not baked (Center) before removal adhere to each other and do not disperse effectively after removal. Devices printed with added triethyl citrate (10% w/w by polymer mass) and baked at 100°C for 20 min have a smooth surface, are robust post-extraction, and disperse effectively (Right). All scale bars are 100 μm.

diluted to 5% (w/v) with deionized water to meet the viscosity limitations of the printer system.

58

During Eudragit FS 30 D printing, the chamber was maintained between 50-55% relative humidity, which was found to yield the most reproducible results.

It was necessary to incorporate a plasticizer (0.5% w/v TEC) into the Eudragit FS 30 D formulation to improve the mechanical robustness of the material (**Figure 3-2**). Microdevices printed without TEC became brittle after evaporation of solvent, and upon removal, devices fractured, whereas devices with incorporated TEC were mechanically robust upon removal. The addition of TEC improved device integrity and brittleness was no longer observed after solvent evaporation.

Wafers printed with Eudragit FS 30 D microdevices were baked at 100°C for 20 min. Without a bake step, the devices were soft, susceptible to deformation, and difficult to remove from the wafer. After the bake step, the microdevices hardened and were easily removed from the silicon wafer via scraping with a sharp blade (**Figure 3-2**).

Scaling microdevice size with number of drops

By controlling the volume of Eudragit FS 30 D dispensed, it is possible to scale microdevice size. Wafers were chilled on a stage at 14°C prior to dispensing droplets. Increasing the number of dispensed droplets from 10-160 leads to microdevices with increasing diameter and height, ranging from ~198-573 µm and 9-19 µm, respectively (**Table 3-1**, **Figure 3-3 A**). Reservoir volumes increased from 90-1821 pL for 10-160 droplets respectively, correlating to a range in loading capacity from 100 ng of insulin per device to upwards to 2 µg of insulin per device. There is a positive correlation between the number of drops and the size and volume of the device (**Figure 3-3 C**, **Table 3-1**).

Controlling microdevice morphology with temperature

Temperature plays an important role in the evaporation rate of water, the transport kinetics of solutes in solution, and the formation of the coffee-ring effect [187,188]. To determine the role of temperature in our system, 40 droplet devices were printed while adjusting the stage temperature (**Table 3-2**, **Figure 3-3 B**). As the temperature increased from 14°C to 22°C, accelerated drying resulted in a device morphology with thinner reservoir bases, ranging from ~1.75 µm to less than
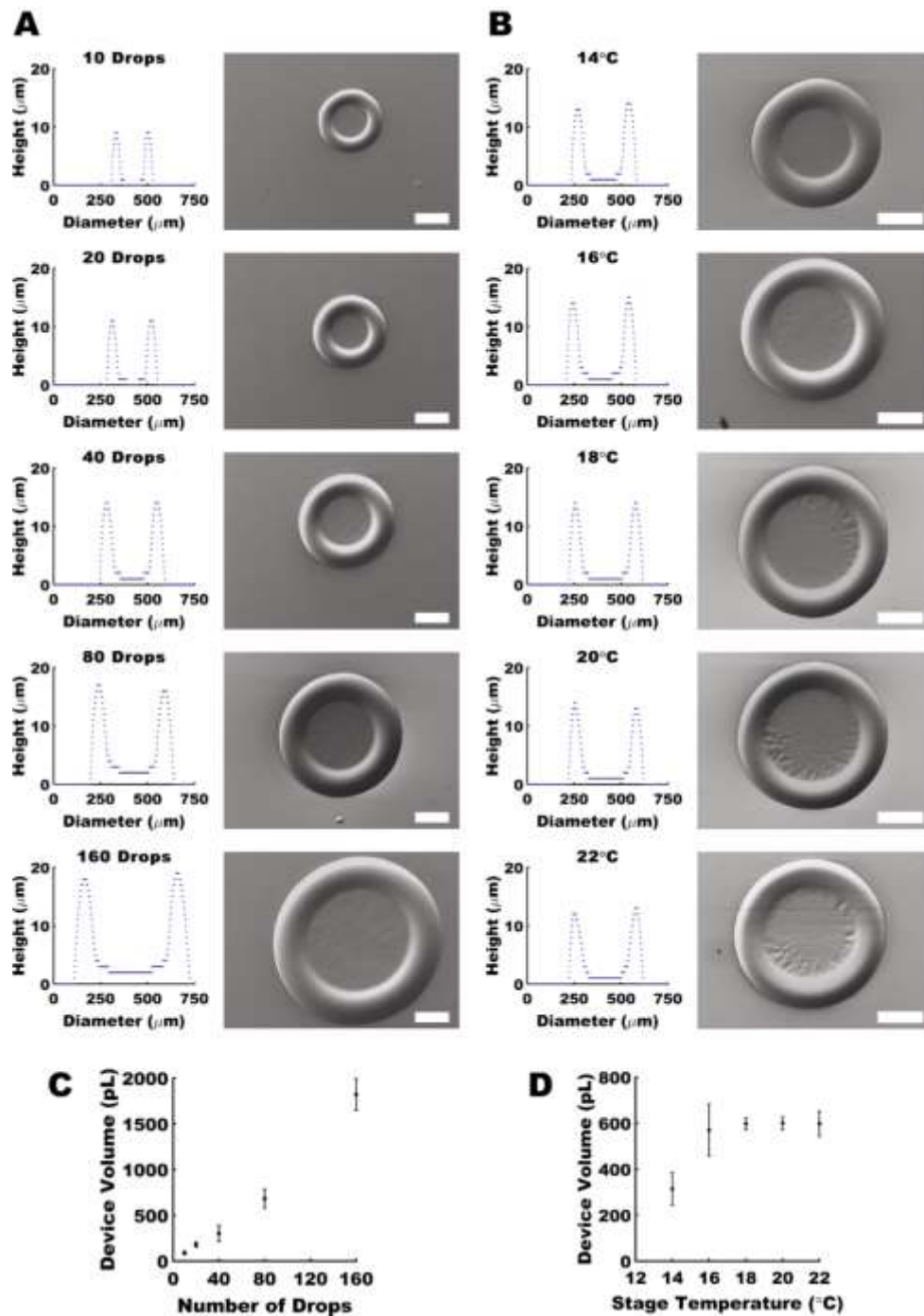
Figure 3-3:
Microdevices composed of Eudragit FS 30 D have tunable morphologies and reservoir volumes. Device body profiles can be tuned based on the number of drops deposited (A) and the stage temperature (B) as shown by profilometry and SEM. Device volume increases in correlation with increasing volume (C) and stage temperature (D). Data shows mean $\pm$ 1 SD, n=5 measurements of separate devices for all groups. All scale bars are 100 µm.

1 µm respectively. Profilometry revealed sloped reservoir walls that increased from ~177 to 250

µm as temperature increased from 14°C to 22°C. The result is a larger volume capacity, 314 pL vs. 598 pL for 14°C vs. 22°C respectively (**Figure 3-3 D**, **Table 3-2**). However, the thin reservoir bases of devices printed at greater than 14°C are susceptible to rupture when mechanically
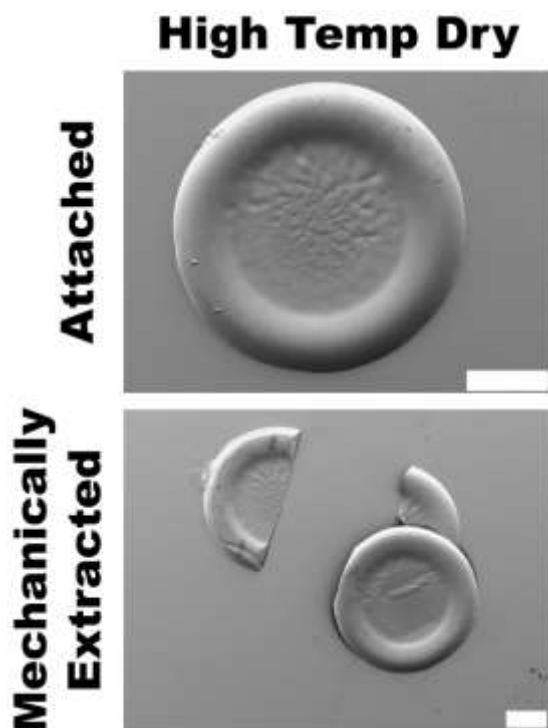
Figure 3-4:
SEM images of devices dried at an elevated temperature (22°C). Devices have a thin reservoir base and tend to fracture upon extraction. All scale bars are 100 µm.

perturbed by a razor blade for removal (**Figure 3-4**). As a result, we maintained the use of a 14°C stage temperature throughout the rest of our studies, as it provided the most mechanically robust devices.

Microdevice material stability

Microdevice bodies were exposed to simulated intestinal fluid (SIF) for 90 min to simulate release in the small intestine and the local pH conditions. SIF is a buffer with a pH of 6.8, below the

theoretical threshold of dissolution for Eudragit FS 30 D. To assess the integrity of the FS 30 D polymer, we took SEM images to visualize surface dissolution. While there was some noticeable surface erosion, device morphology was relatively unchanged, suggesting functional stability in a relevant time frame for delivery (**Figure 3-5**).

Insulin loading and controlled release

Microdevices were loaded as described previously [179]. Filtered insulin formulated in 10 mM HCl was aspirated into the capillary and aligned to the fiducials on the silicon wafer before beginning an automated print run. Approximately 100 ng of insulin was deposited into each device. Insulin was stable upward of 94% after loading, capping, and *in vitro* release (**Figure 3-6**). This insulin stability is similar to previous work using the printing process [179]. SEM images of each stage of device fabrication can be seen in **Figure 3-1 B**.
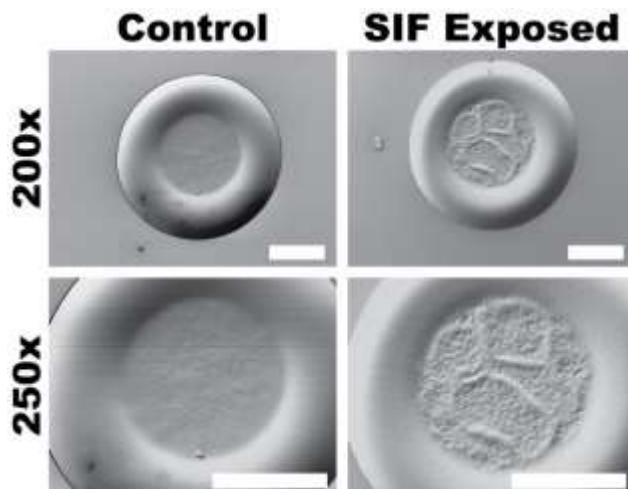
Figure 3-5:
SEM imaging at 200x and 250x magnification shows that devices retain their integrity after prolonged exposure to simulated intestinal fluid (SIF). Compared to control devices (Left), exposed devices (Right) show signs of surface erosion but retain their morphology and integrity. All scale bars are 100 µm.

Two types of Eudragit were used for capping: L 100 and S 100. Eudragit L 100 is a co-polymer designed for dissolution in solutions pH 6.0 or higher, whereas Eudragit S 100 is a similar

polymer designed for release in environments above pH 7.0. Prior to SIF exposure, capped devices appear to be similar in material deposition (**Figure 3-7 A**). To simulate oral drug delivery to the small intestine, microdevices were exposed for 60 min in SIF. Release studies were performed at 37°C to simulate physiological conditions for release kinetics and protein stability. In order to normalize release profiles between wafers, some devices are left uncapped. After exposure, it is evident from profilometry data that dissolution of the capping material and loaded insulin occurred in L 100 caps while 1:1, and particularly, S 100 caps, show resistance to dissolution (**Figure 3-7 B**). Devices are allowed to fully dry between sequential insulin and cap printing steps, and stored under desiccating conditions, limiting the presence of residual solvent in the final devices.
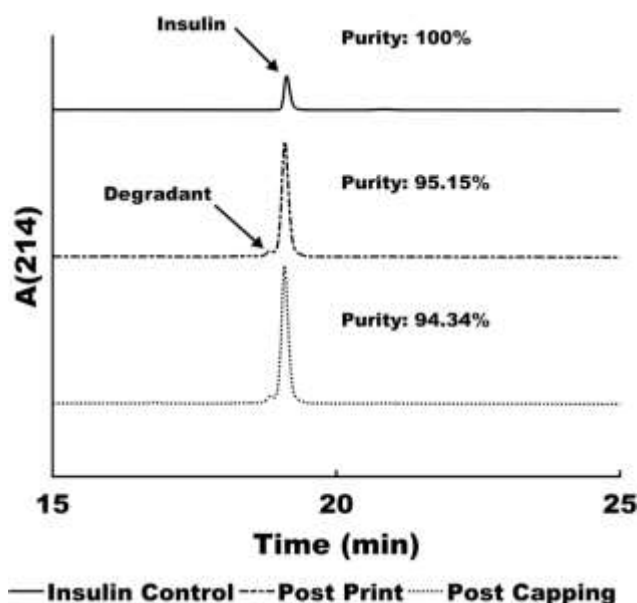
Figure 3-6:
Stability of insulin is maintained throughout device fabrication, loading, and capping. Insulin was either prepared fresh in 10 mM HCl at a concentration of 10 µg/mL (Insulin Control), aspirated into the sciFLEXARRAYER S3, and deposited into devices before being eluted into SIF for one hour (Post Print), or capped prior to elution (Post Capping). Collected samples were analyzed using the described HPLC method.

Based on capping formulation, microdevices exhibited a range of release kinetics (**Figure 3-8**). L 100 capped devices show purely burst release properties, releasing more than 80% of their

loaded insulin within 5 min, and more than 90% at 15 min. S 100 capped devices alternatively

showed almost no insulin release, with less than 10% of the loaded insulin released by 60 min.

The 1:1 capped devices have a release profile that is a hybrid of the L 100 and S 100 caps. By 5

min, the 1:1 capped devices have released less than 3% of the loaded insulin, suggesting a temporal

delay that closely matches the kinetics of the S 100 capped devices. Then between 15 min and 60

min, the 1:1 capped devices gradually released an additional 70% of the loaded insulin, suggesting

the presence of a more effective diffusion-limiting barrier as compared to the L 100 capped or

uncapped devices.
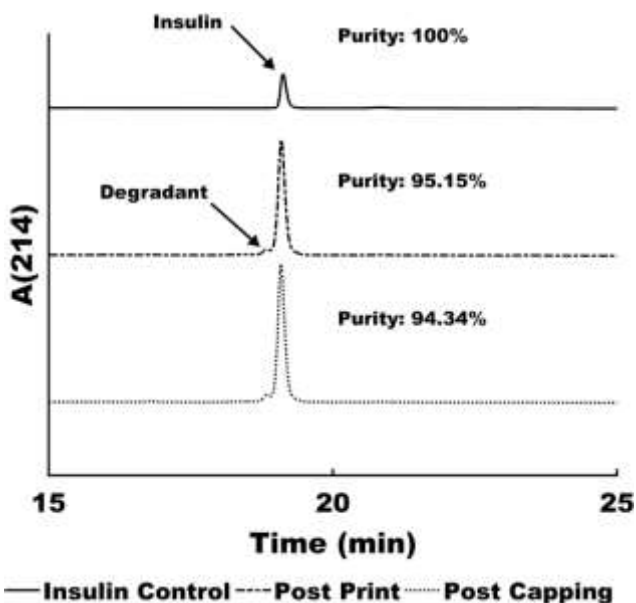
Figure 3-7:
Capping formulation impacts dissolution kinetics and
morphologies as shown through SEM imaging and
profilometry. (A) Insulin loaded devices either left
uncapped, capped with L 100, S 100, or capped with a 1:1
blend of L 100 and S 100 before exposure to simulated
intestinal fluid (SIF). (B) Insulin loaded, capped devices
exposed to SIF for 60 min. As expected, caps that
incorporate

Mechanical integrity of capped microdevices

Insulin-loaded, capped Eudragit FS 30 D devices printed onto a silicon wafer (**Figure 3-9 A**)

maintained their structural integrity through mechanical removal from the wafer using a razor

blade (**Figure 3-9 B**) including their layered structure and with intact caps even without a heat processing step for the capping materials.

3.5 Discussion

Device fabrication and characterization

In this work, we demonstrate an additive manufacturing approach using droplet deposition from a picoliter dispenser to fabricate micron-scale devices of varying geometries in a scalable manner. The same picoliter dispenser is used to load sensitive peptides in a low-waste manner followed by enteric polymer capping for controlled release of peptide for oral delivery. The drug carrier and
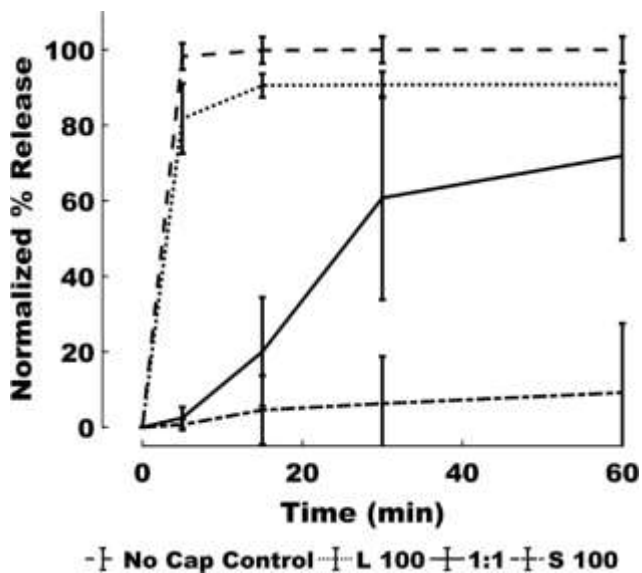
Figure 3-8:
Release of insulin from capped microdevices over the course of 1 h in SIF. Three different caps were tested: i) Eudragit S 100, ii) 1:1 blend of Eudragit S 100 and Eudragit L 100, and iii) Eudragit L 100. Caps containing Eudragit S 100 show temporal and kinetic delay of insulin release. Data represents mean ± 1 SD (No Cap Control; L 100; 1:1, n=3; S 100, n=4).

cap components are formulated out of Eudragit-based materials, which are commonly used polymers for GI targeting, sustained drug-release, and enhanced solubility [172].

An ideal drug carrier will protect its payload during gastrointestinal transit. Eudragit FS 30 D was the ideal candidate for printing the microdevice body due to its resistance to degradation in pH conditions < 7.0, thereby producing a carrier that will persist in the stomach for oral delivery to the small intestine. It is formulated as a low pH, aqueous dispersion that is amenable to dilution, blending, and additional formulation with plasticizers like TEC. Furthermore, the low-viscosity of the solution, < 10 cP, makes it amenable for printing out of a picoliter ink-jet printer.
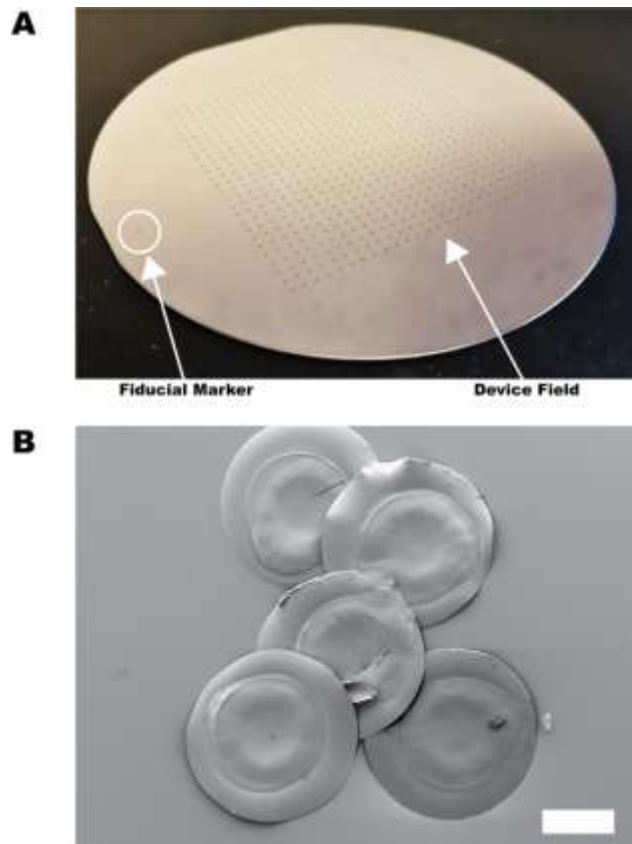
Figure 3-9:
Loaded and capped microdevices are mechanically robust and dispersible. (A) Representative image of 3'' silicon wafer with 676 printed devices and India ink fiduciary marks. (B) Insulin loaded, S 100 capped devices mechanically scraped from silicon substrate using a razor blade remain intact for subsequent processing and delivery. Scale bar is 100 μm.

The microdevice body shape is formed via a phenomenon in material deposition during drop-drying known as the coffee-ring effect [188–190]. Edge pinning and convective transport of dispersed material causes material deposition preferentially at the drops' edge. The result is a device with a thick ring on the outside and a thinner base in the center to form a reservoir. This unique geometry allows us to take advantage of the interior space for drug loading. In addition, the geometry of our devices can be tuned on-the-fly by adjusting the total number of drops

Table 3-1:
Effect of volume deposited on final device body morphology. Measurements made via contact profilometry. Data represents mean ± 1 SD, n=5 measurements of separate devices for all groups. Wafer temperature was set at 14°C for all groups. Reservoir volume represents a derived value based on the reservoir diameter and height estimated as a cylinder.

Volume Dispensed	Device Diameter (µm)	Device Height (µm)	Reservoir Diameter (µm)	Reservoir Height (µm)	Reservoir Thickness (µm)	Volume (pL)
10 drops	198.04±2.30	9.14±0.11	114.00±4.89	8.80±0.07	0.34±0.13	89.82±15.43
20 drops	247.60±4.48	11.42±0.13	145.52±5.03	10.88±0.08	0.54±0.15	180.95±25.04
40 drops	298.96±3.66	13.72±0.40	178.02±12.70	12.18±0.31	1.54±0.50	303.16±86.84
80 drops	394.48±4.28	16.74±0.48	244.00±8.97	14.62±0.46	2.12±0.67	683.62±102.77
160 drops	573.00±6.98	19.15±0.22	366.00±7.79	17.31±0.14	1.841±0.26	1821.16±173.11

dispensed, an improvement to previous methods utilizing microfabrication or batch processes. We found that it is possible to fabricate devices with a wide range of volume capacities, the most important parameter for drug loading, that span two orders of magnitude from tens to thousands of pL, Common clinical doses of insulin are on the order of 100s of µg, which would correlate to

100s of the 160 droplet sized devices, though for human scale trials even larger devices could be implemented, drastically reducing the number of devices required per dose.[191]

In addition, by controlling the kinetics of drying and transport, it is possible to control deposition morphology. By precisely controlling the chamber humidity and substrate temperature, we generated devices that have a defined reservoir and base after material deposition onto a silicon substrate. In addition, we discovered that it is critical that microdevices are formed at low temperatures, 14°C, to ensure that microdevice reservoirs are thick enough to prevent fracture

Table 3-2:
Effect of substrate temperature on final device body morphology. Measurements made via contact profilometry. Data represents mean ± 1 SD, n=5 measurements of separate devices for all groups. 40 drops were dispensed per device for all groups. Reservoir volume represents a derived value based on the reservoir diameter and height estimated as a cylinder.

Stage Temperature (°C)	Device Diameter (µm)	Device Height (µm)	Reservoir Diameter (µm)	Reservoir Height (µm)	Reservoir Thickness (µm)	Volume (pL)
14°C	305.88±6.94	14.48±0.31	176.98±10.02	12.78±0.24	1.7±0.39	314.39±71.41
16°C	351.60±9.84	14.58±0.63	230.58±11.19	13.66±0.56	0.92±0.84	570.41±113.18
18°C	360.72±7.00	14.00±0.39	241.16±1.52	13.08±0.41	0.92±0.57	597.46±23.97
20°C	360.26±3.09	13.88±0.41	241.56±1.61	13.10±0.47	0.78±0.63	600.36±26.98
22°C	359.78±4.33	13.08±0.92	250.38±1.70	12.14±1.06	0.94±1.41	597.73±54.85

when removed from the silicon wafer. Drying at higher temperatures result in devices with thin bases that cannot be removed from the silicon substrate without shattering, due to accelerated convective transport of the FS 30 D dispersion to the pinned edges of the drop during drying.

Conversely, lower temperatures approaching the environmental dew point prevent fluid evaporation and device drying, a requirement for device formation.

Still, micronized Eudragit FS 30 D may be more susceptible to accelerated dissolution due to increased surface area compared to the bulk material. Thus, we wanted to ensure that the Eudragit FS 30 D microdevices do not dissolve prior to the release of insulin. By exposing the devices to SIF, which mimics a pH environment similar to that of the small intestine, we found minimal evidence of surface erosion with our microdevices. This is important for two main reasons. First, the device will protect the API payload throughout transit and second, the device body will not lead to critical failure that would cause burst release of the API.

API loading and release

We loaded our microdevices with insulin as our model API. While the loading process is similar to our previous work, the ability to print fiducial markers and microdevices with the same platform used to print API improves the throughput of the entire fabrication process. Controlled drug release in the gastrointestinal tract is a necessary benchmark for improved pharmacokinetic properties in oral delivery systems.[192,193] Effective targeting of the small intestine can maximize absorption but requires a delivery vehicle that can release the drug in the correct region of the small intestine, usually in a pH sensitive manner. Our controlled release and dissolution studies demonstrate the utility of different formulations of Eudragit caps to enable tunable drug release. The goal of this process was to produce a device cap with different dissolution properties compared to the device body, which prompted the use of Eudragit S 100 and L 100, both of which erode at a lower pH compared to Eudragit FS 30 D. In normal use cases, Eudragit L 100 is ideal for small intestinal delivery. However, our microdevices have a much higher exposed surface area compared to that

of the bulk material, leading to more rapid dissolution. Conversely, Eudragit S 100 is designed for colonic delivery. In our study, we show that a micronized form of Eudragit S 100 is very robust against exposure to a pH less than 7, leading to effectively no erosion or drug release. In addition, we formulated a 1:1 (w/w) blend of both Eudragit L 100 and S 100 to create caps which feature characteristics of both materials. Our results demonstrate that altering the capping formulation can change both the temporal delay and kinetics of drug release. This demonstrates that controlling the ratio of L 100 to S 100 in the capping materials allows for tunable control of peptide release kinetics. Micronized forms of both L 100 and S 100 are expected to undergo dissolution in SIF, but these assumptions are based on studies of macroscale bulk materials. It is reasonable to assume that the low aspect ratio and the form factor of the S 100 and the 1:1 blend led to the observed deviations from the expected dissolution profiles of these two capping materials. The release data are further supported by SEM images of both uncapped and capped devices with all three Eudragit formulations before and after exposure to SIF for 60 min (**Figure 3-7**). It is likely the case that through further tuning of the blending and layering of the capping material, it will be possible to achieve an even wider range of API release profiles including pulsatile release profiles. Furthermore, our drug release studies in SIF demonstrated that we were able to recover an intact, stable insulin product after deposition into the devices and post-capping. This demonstrates that the printing process and subsequent capping process can be used for sensitive drug molecules, an advantage over other systems that lead to drug degradation during the fabrication process.

From a translational point of view, it is important that we are able to extract the microdevices from the silicon wafer and formulate them into a solution for oral drug delivery. However, our extraction process does not require use of water or solvent, an advantage over

previous microdevice technologies that require a wetting solvent to ensure clean extraction of devices, which can lead to premature drug release during the device removal process.

3.6 Conclusions

We demonstrated a bottom-up, layer-by-layer approach for fabrication of microdevices for oral peptide delivery. We take advantage of drop-drying physics and the coffee-ring effect to fabricate micron-scale devices with reservoirs. The microdevices consist of Eudragit FS 30 D as a device body having a reservoir to allow encapsulation of insulin as a model peptide, followed by a capping polymer. The microdevice size can be tuned by controlling the substrate temperature and the number of printed drops. More than 94% insulin remained intact during the fabrication process, demonstrating that the process does not appreciably degrade protein cargo. Furthermore, we show that by altering the capping material, it is possible to achieve a range of release kinetics from our devices. This method enables rapid iteration and optimization of new materials, APIs, and device geometries during fabrication and has potential utility beyond drug delivery in microelectronics and microfluidic systems.

Chapter 4 - Impact of Microdevice Geometry on Transit and Retention in the Gastrointestinal Tract

4.1 Abstract:

The delivery of protein and macromolecule therapeutics via the oral route is a widely explored research area, with far reaching clinical implications. An emergent methodology is to encapsulate therapeutics in microscale, asymmetric, planar microparticles, referred to as microdevices. Previous work has shown that, compared to spherical particles, planar microdevices have longer residence times in the gastrointestinal (GI) tract. However, relatively little work has explored how device size governs their behavior in the intestinal environment. In this study, we probe how the geometry of planar microdevices impacts their transit and accumulation in the murine GI tract. Additionally, we present a strategy to label, image, and quantify these distributions in intact tissue in a continuous manner, enabling a more detailed understanding of device distribution and transit kinetics than previously possible. We show that smaller particles tend to empty from the stomach faster than mid-size and larger devices, and that larger devices distribute more broadly in the GI tract and exit slower than other geometries. These results inform the future design of drug delivery systems, using particle geometry as an engineering design parameter, to control how the devices accumulate and distribute in the GI tract. Additionally, our image analysis process provides more insight into the tissue level distribution of individual particles, and how the particle populations transit through the GI tract. Using this technique, we show that microdevices act and translocate independently, as opposed to transiting in one homogeneous mass, meaning that target sites will likely be exposed to devices multiple times over the course of hours post administration. This technique has relevance in applications where understanding local targeting in the gastrointestinal system may influence treatment outcomes, such as in treatment of inflammatory disease, in the delivery of probiotics, or in oral vaccination.

4.2 Introduction:

Oral delivery of protein drugs remains a highly desirable but elusive goal. Many barriers exist to systemic dosing of protein drugs through the oral route, notably the inhospitable chemical environment of the gastrointestinal (GI) system, and the limited ability of biomacromolecules to effectively absorb across the mucosal surface.[152] Despite this, many patients prefer oral delivery when possible, even if it incurs a higher price.[194] Throughout the last two decades, a number of groups have approached using micro and nano materials as a means to improve the bioavailability of macromolecular therapeutics via the oral route.[195–197] These technologies are often designed with the dual goal of protecting the encapsulated active pharmaceutical ingredient (API) from degradation in the low pH of the stomach or digestion via intestinal proteases, and facilitating the increased absorption of API across the intestinal epithelium.[153] Another potential benefit of micro and nanoscale material approaches is the ability to incorporate targeting into the system design, which has been demonstrated using lectins, micromotors, chemically responsive materials, and other physiochemical approaches.[185,198–201] One strategy has been to adapt micro scale fabrication techniques to generate planar materials that incorporate asymmetry. Due to their asymmetric reservoir design, these particles can be loaded with a therapeutic cargo, and capped to enable controlled drug release or mucoadhesion.[160] This design also facilitates asymmetric release of the loaded compound, which allows for increased concentration of the API and associated formulation agents at the mucosal surface and limits loss to the lumen which is inherent in omnidirectional release. Importantly, unlike similar systems using microspheres, planar materials have a greater surface-area-to mass ratio, rendering them unable to roll across mucosal surfaces and conferring an inherent adhesive property. It has been previously demonstrated on a tissue level that these materials tend to have longer residence times than

equivalent microspheres.[185] However, there has been little work to better understand how microscale properties and design choices impact planar microdevice transit and accumulation in the gastrointestinal (GI) tract.

Many pharmaceutical systems protect their cargo in the GI tract via encapsulation with enteric polymers. Enteric polymers are pH sensitive materials designed to erode and solubilize above a specific pH.[172,173] By blending these materials, it is possible to release cargo in specific areas of the GI tract based on the local pH microenvironment, which ranges from highly acidic in the stomach and proximal small intestine, to more alkaline (pH ~7) in the proximal colon.[202] Enteric materials exist in a number of formulations, and have been widely incorporated into FDA approved products, making them an excellent choice for the development of oral drug delivery systems. However, their application in oral drug delivery systems has been mostly restricted to use as a spray or dip applied coating, while microscale device structures are still produced using more conventional photolithography and microfabrication.[156,199,203] Photolithography-based microfabrication is a scalable and reproducible process, but is often a barrier to rapid iterative design, requiring extensive reoptimization and redesign of photomasks to generate new materials.[157] Additionally, photolithography depends on a limited set of materials that are not necessarily compatible with clinical use, limiting the translation of these systems.[163] Previously, we demonstrated a technique to generate planar microdevices using a non-contact picoliter droplet printer and layer-by-layer additive manufacturing techniques.[204] These devices were fabricated, loaded with protein, and capped with an enteric coating using a single instrument. These particles are composed entirely of Eudragit brand polymeric materials (Evonik, Essen Germany), which are widely used in clinical products to enable extended release formulations and as solubility enhancers for solid dispersions.[172] This approach also enables rapid iteration of

76

device geometry, enabling production of materials that can range in size by 3-4 fold in an on-demand, programmatic fashion.

A major goal in the development of oral protein delivery systems is to increase the bioavailability of their cargo, which often necessitates material accumulation in a target location for an appropriate amount of time.[202] Early studies examining the transit of materials through the GI tract used a radioactively labeled ion exchange resin to study the impact of viscosity and polymer coatings in the context of gastric emptying.[205] Other groups have explored how nanoscale materials of varying sizes and geometries distributed through and were taken up by GI tissue, demonstrating how material choices impact organ targeting and delivery.[200,206–208] However, because these materials often reach systemic circulation, the mechanism of their interaction with GI tissue is likely very different than larger scale materials, which are more prone to gravitational sedation and cannot be taken up through transporter mechanisms. Studies tracking the transit of larger materials, such as capsules or tablets, have shown that perturbing the animal during imaging might alter the speed at which these materials move through the GI tract.[209] Other studies have approached tracking self-propelled micromaterials in tissue, and how motile forces could be engineered to achieve different transit speeds and retention times.[198] However, it remains unclear how low aspect ratio materials, such as planar micro devices, dependent only on peristaltic motion, will distribute and accumulate in the GI tract. Studies that have approached tracking the distribution of microscale materials generally have examined spherical particles and have been limited by the resolution of their tracking methodologies.[210,211]

Applying the flexibility of the printed microdevice system, we sought to understand the downstream impact of design choices on the *in vivo* behavior of these materials. Due to the unique capabilities of the microdevice printing platform, we generated monodisperse particle

populations of distinct sizes, using the same base materials and body geometry. This consistency in fabrication is unique compared to other systems that have been used to examine the impact of particle size on GI transit, which have used distinct formulations for each particle size or were restricted in the range of generatable particle sizes.[200] Here, we demonstrate the fabrication and use of fluorescently labeled, planar microdevices as a model to understand how planar materials behave in transit through the murine GI tract. Because the printed microdevices are on the order of hundreds of microns in diameter, they were unable to be absorbed through transcellular or paracellular processes, enabling transit throughout the entire length of the GI tract. The introduction of a covalently bound near-IR fluorophore into the backbone of the enteric materials used in our microdevice bodies allowed for direct tracking of devices in intact tissue via an *in vivo* imaging system (IVIS). We have also developed an accompanying image analysis workflow to understand how these devices distribute in tissue at a finer resolution than previously possible. This computational image analysis workflow allowed us to extract continuous distance vs. fluorescence signals, and provided refined insight into impact of microdevice size on transit speed. This generation of a continuous signal allowed us to explore how microdevices traffic as populations and how they interact with each other *in vivo.* Taken together, this study confirms that microdevice size can be used as an engineering design parameter to control distribution kinetics and retention time in the GI tract, and validates an image analysis approach to quantify the continuous distribution of materials in the GI tract, enabling a finer degree of understanding that may be lost in regionalized approaches.

4.3. Materials and Methods:

Materials: Eudragit FS 30 D and S 100 were kindly provided by Evonik Industries (Essen, Germany). All other chemicals and materials were acquired from Thermo-Fisher.

Fluorescent labeling of Eudragit polymer: AlexaFluor-647 Cadaverine (AF 647-cad) was covalently bound to Eudragit S 100 using a DCC-NHS coupling reaction. Briefly, Eudragit S 100 (50 mg, ~4 nmol) was dissolved in dimethylformamide (DMF) (4 mL) on a magnetic stir plate. The solution was moved to an ice bath, and *N*-Hydroxysuccinimide (NHS) (7.8 mg, 67.8 μmol) in DMF (2 mL) was added stirring on ice for 5 min, followed by the addition of *N,N'*-Dicyclohexylcarbodiimide (DCC) (14 mg, 67.8 μmol) in DMF (2 mL). The reaction was allowed to proceed for 3 hr stirring on ice. A stock of AlexaFluor 647-Cadaverine (AF 647-Cad) (1 mg, 1 μmol) was prepared in dimethyl sulfoxide (100 μL). AD-647 Cad stock solution (40 μL, 0.4 mg, 0.4 μmol dye) was diluted in DMF (600 μL) along with triethylamine (TEA) (0.56 μL, 4 μmol) and allowed to react on an orbital shaker (100 rpm) for 1 min protected from light at ambient temperature. The dye solution was added to the polymer solution, and allowed to react on a magnetic stir plated for 72 hr while protected from light. After 72 hr, the reaction solution was diluted with 45 mL of 4-(2-hydroxyethyl)-1-piperazineethanesulfonic acid (HEPES) buffer (100 mM) adjusted to pH 8 with 1M NaOH for 8 hr on an orbital shaker (100 rpm) protected from light at ambient temperature. The resulting solution was passed through a 0.2 μm vacuum filter to remove precipitates, followed by multiple rounds of concentration using a 30K MWCO spin concentrator to remove excess small molecule dye. The resulting product was lyophilized to afford a blue powder (50 mg, 100% polymer recovery). Conjugation was validated through reverse-phase liquid chromatography (**Figure 4-8**).

Device fabrication: Microdevices were fabricated as previously described using a ScienIon sciFLEXARRAYER S3 (Scienion, Berlin, Germany) non-contact, picoliter, inkjet printer (**Figure 4-1 A**).[204] Briefly: A 3 inch silicon <100> wafer was cleaned in a piranha solution (1:1 sulfuric acid : hydrogen peroxide) for 30 min and allowed to soak in deionized water for 30 min to remove excess solution. Wafers were then dried completely using dry nitrogen gas and silanized with trichloro(1H,1H,2H,2H-perfluorooctyl)silane under vacuum at room temperature for 40 min, followed by curing for 20 min on a 150 °C hot plate. Polymer solutions were prepared at 5% (w/v) total polymer. For fluorescently labeled devices, the AF 647 Eudragit S 100 was incorporated at 20% (w/w) of the total polymer mass, with Eudragit FS 30 D comprising the remaining material. Triethyl citrate was added to 0.5% (w/v) as a plasticizer. All solutions were filtered through a 0.22 μm filter prior to aspiration. The polymer solution was aspirated into the printer nozzle and dispensed in ~400 pL droplets onto the wafer surface, which was maintained at 20 ⁰C. Fluorescently labeled devices were protected from light throughout the printing process. After printing, the devices were allowed to completely dry under ambient conditions, before being moved to a hot plate and baked at 100 ⁰C for 20 min to remove residual moisture. Resulting device bodies were then stored in a vacuum desiccator at room temperature and protected from light until further use.

In vitro **assessment of conjugate stability**: For fluorescent imaging, devices were printed onto glass coverslips using the method described above. Printed devices were incubated in either simulated intestinal fluid or simulated gastric fluid for the indicated amount of time. After incubation, devices were washed briefly in deionized water and dried at room temperature in a vacuum desiccator. Devices were then affixed to a microscope slide and imaged using an

inverted Nikon 6D fluorescent microscope using a Cy-5 filter set at 20x magnification. Quantification of maximum pixel intensity was performed using imageJ.

Oral gavage of fluorescent microdevices: All animal studies were performed in accordance with the UCSF Animal Use and Care Program, under protocol no AN180829-02A. All studies were performed with 8-12 week old female C57BL/6J mice acquired from Jackson Laboratories (Bar Harbor, ME). One week prior to dosing, the diet of animals was switched to a low auto-fluorescence diet (5v75, LabDiet, St. Louis, MO) and 24 hr before device administration, the mice were fasted. To prepare devices for administration they were removed from the silicon wafers mechanically using a razor blade, and dispersed in a simulated gastric fluid solution containing 1% (w/v) polyvinyl alcohol (PVA) as a dispersant. Devices were concentrated either via natural sedimentation or low speed benchtop centrifugation, and then loaded into a 30 mm 18 G polypropylene feeding tube. Devices were dispersed in 200-250 μL and gavaged directly into the stomach of each mouse at time 0 min. At each timepoint, mice were sacrificed via carbon dioxide asphyxiation and cervical dislocation. The complete GI tract of each mouse (stomach to anus) was extracted and the ends were sutured closed. The tissue was stored on ice between paper towels saturated with PBS and imaged immediately using a Xenogen IVIS Spectrum Imaging System using the pre-set AF 647 filter settings. To capture regional fluorescence data, non-tissue areas were masked out using Xenogen software, and ROIs were drawn to capture each area and limit signal cross-contamination.

Visualization of device transit: Visualization of device tracking was performed using a MatLab script in combination with an ImageJ plugin. Briefly, images of mouse GI tracts were exported as separate monochromatic fluorescent and light photograph images (**Figure 4-9 A**). Both images were identically cropped to only contain relevant areas. Next, the GI tract in the light

microscopy image was traced using a MatLab ROI selection tool, which was used to select the equivalent area on the fluorescent image (**Figure 4-9 B**). The image was imported to ImageJ, and linearized using the straighten selection tool (**Figure 4-9 C**). The linearized image was re-imported to MatLab, where irrelevant pixels were removed and the image was compressed into a one-dimensional vector (**Figure 4-9 D**). The signal data was normalized to the total signal, and distance was expressed as a percent of total distance along the GI tract (**Figure 4-9 E**). Further details can be seen in the caption of **Figure 4-9**.

Statistical analysis: Statistical analysis was performed using the MatLab 2020B statistics and machine learning package (MathWorks, Natick, MA). Statistically significant differences between groups were evaluated by one-way ANOVA, followed by a Tukey-Kramer correction for multiple comparisons, setting $\alpha = 0.05$. For digital signal analysis, statistical significance was determined by cross correlation, followed by a Bonferroni correction for multiple comparisons setting $\alpha = 0.05$.

4.4. Results:

Fluorescent dye conjugate synthesis: The fluorescent polymer conjugate was prepared using activated ester conjugation chemistries and purified from free dye via spin concentration (See Materials and Methods). The formation of a covalent linkage was evaluated via reverse phase HPLC, monitoring conjugate elution at 650 nm (**Figure 4-8**). Conjugation efficacy was determined via absorbance at 650 nm of a 1 mg/mL solution of the dye-polymer product,

demonstrating the addition of approximately 3 µg of dye per mg of polymer, or the conversion of approximately 37% of the initial dye.
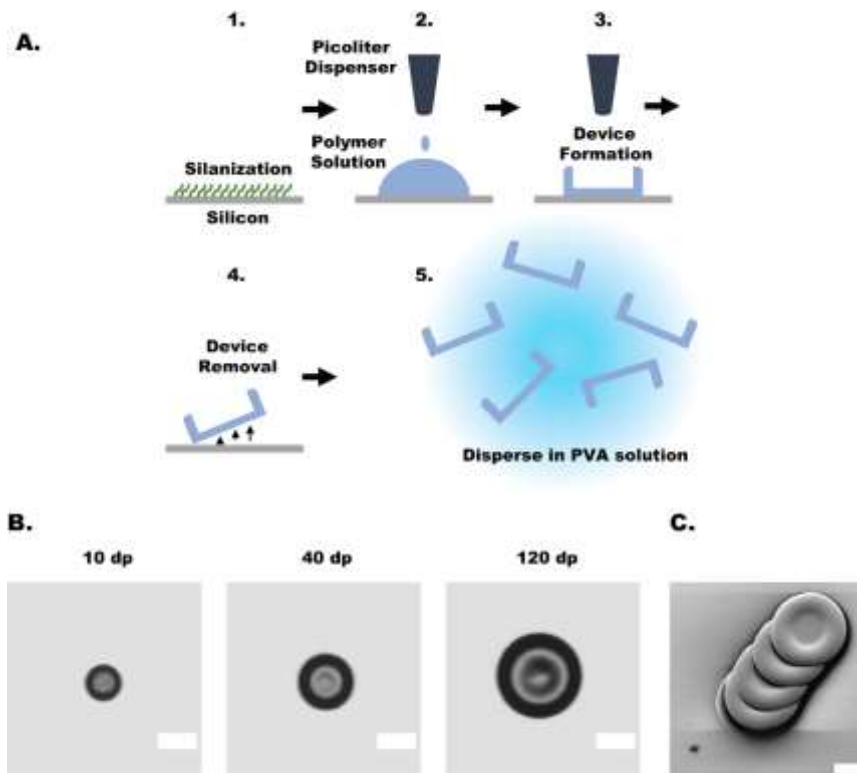
Figure 4-1:
Schematic of device fabrication and device characterization. (A) (1). A silicon wafer was silanized to enable fluid beading on the surface. (2) The programed volume of polymer solution was dispensed onto the surface. (3) The polymer solution was allowed to fully dry, forming the device reservoir. (4) Devices were removed from the wafer surface using a razorblade. (4) prior to oral dosing, devices were dispersed in a simulated gastric fluid solution containing 1% (w/v) polyvinyl alcohol. (B) Light microscopy images of representative microdevices. Device measurements can be found in **Table 4-1**. Scale bars represent 200 µm. (C) Scanning electron microscopy image of devices mechanically removed from silicon wafer; scale bar represents 100 µm.

Device Fabrication and Characterization: As demonstrated previously, planar, asymmetric, microdevices were fabricated using a non-contact picoliter droplet liquid handling system (**Figure 4-1 A**). Devices were fabricated from a 20% (w/w) blend of 100-AF to 80% (w/w) FS 30 D because it was observed to be sufficiently bright to enable *in vivo* imaging without compromising the mechanical integrity of the device bodies (data not presented). In order to

83

adjust final device size, the volume of material deposited was adjusted by controlling the number

of 400 pL droplets dispensed per device. Device diameters were measured to be 194.6±8 μm,

293.2±7 μm, and 440.8±9 μm (mean ± 1 SD, n=5 measurements per group), corresponding to 10

droplets, 40 droplets, and 120 droplets, respectively (**Figure 4-1 B**). As previously shown, SEM

images of discrete mechanically extracted devices demonstrate maintained structural stability

(**Figure 4-1 C**).[204]
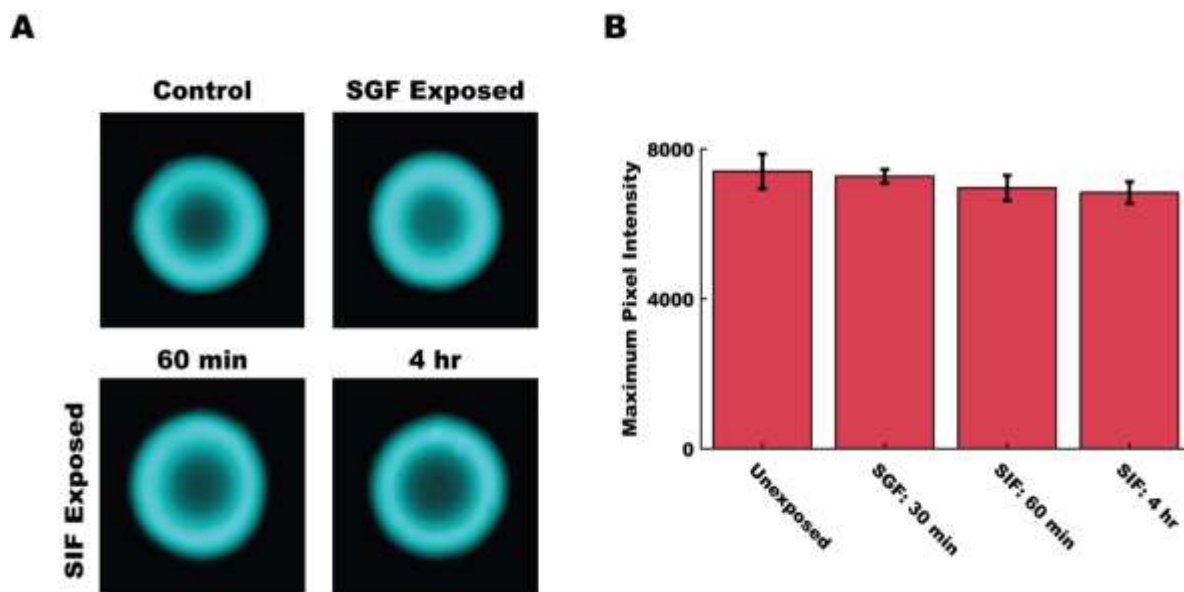
Figure 4-2:
Fluorescent polymer conjugate was stable throughout the anticipated use case. (A) Representative fluorescent images of devices after exposure to simulated gastric fluid (SGF) and simulated intestinal fluid adjusted to pH 5 (SIF). (B) Comparison of maximum pixel intensity between fluorescently labeled devices exposed to SGF for 30 min, SIF adjusted to pH 5 for 60 min or 4 hr. Data represents mean ± 1 SD of n=5 devices per group. No differences were detected between groups at α=0.05, using a one-way ANOVA followed by a Tukey-Kramer correction for multiple comparisons

Fluorescent Conjugate Stability: Devices were exposed to simulated gastric fluid or simulated

intestinal fluid adjusted to pH 5 with hydrochloric acid to better mimic the murine intestinal

environment (**Figure 4-2 A**).[212] Mean pixel intensity data was compared to a control unexposed

group (**Figure 4-2 B**). Simulated gastric fluid exposure for 30 min does not impact device

fluorescence intensity, measured as maximum pixel intensity in a given device image. Similarly, devices exposed to simulated intestinal fluid (pH 5) for 60 min and 4 hr maintained their fluorescent signal throughout the duration of their exposure. No significant differences (at $\alpha=0.05$) were detected in any pairwise comparison.

Oral Gavage and Regional Fluorescence: For oral dosing studies, dosages were prepared by device number, and adjusted to account for the difference in device mass per device between groups. Animals were dosed according to **Table 4-1** (**Figure 4-3 A**) and imaged at the specified time points, recording both ROI information and the fluorescent signal overlay (**Figure 4-3 B**). After administration, there was a noticeable loss in device numbers in the dead volume of the syringe, amounting to between 15-20% of the total devices. During imaging, no pixel saturation was observed in any sample. The 200 μm and 450 μm groups had n = 3 animals per time point, while the 300 μm group had n = 2 animals per time point due to the exclusion of a preliminary data set that was deemed to have insufficient fluorescent signal.

Comparisons between regional signal data were used to track the accumulation of devices in biologically relevant areas (**Figure 4-3 B** and **Figure 4-4**). At the 30 min time point, the stomach signal in the 200 μm group (**Figure 4-5**) was significantly larger than the signal in the lower small intestine (p=0.018), the cecum (p=0.0052), and colon (p=0.0051). By 60 min the device
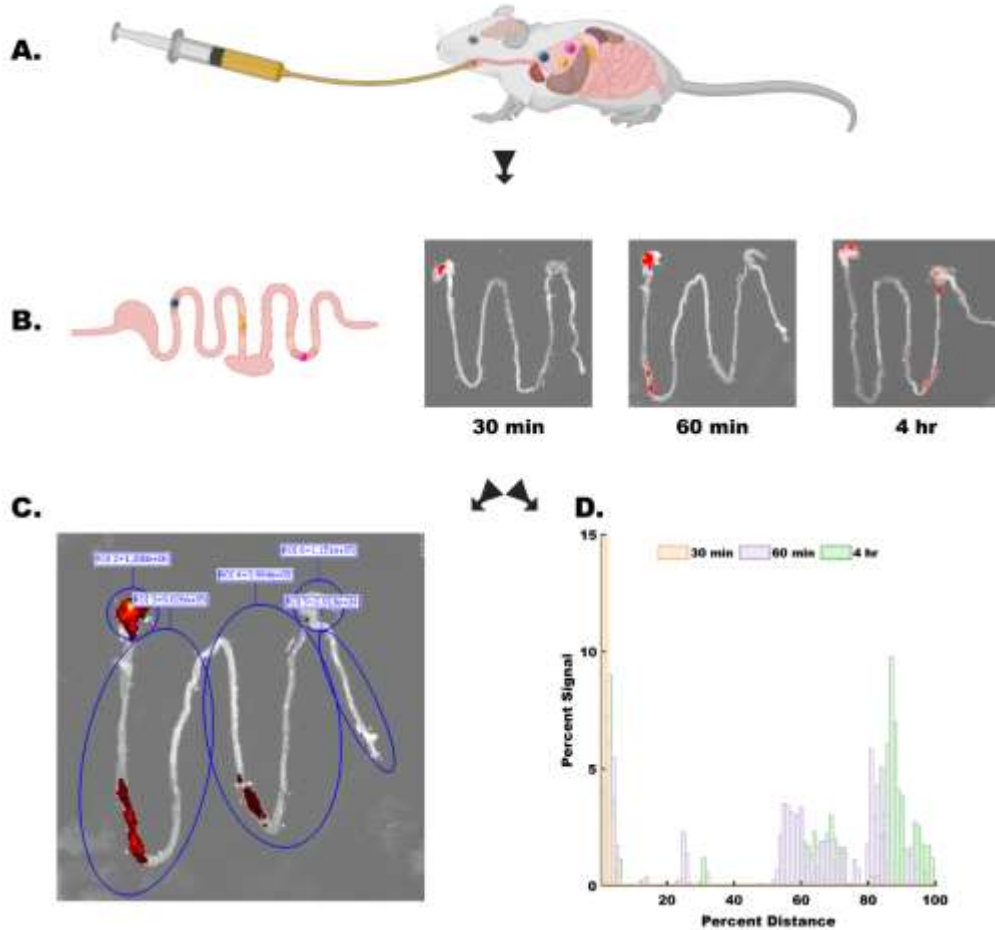
Figure 4-3:
Experimental process schematic. (A) Micro devices were dosed to animals via oral gavage, directly into the stomach at time = 0. (B) At each time point (30 min, 60 min, & 4 hr) animals were sacrificed, their gastrointestinal tract from the stomach to the anus was removed and imaged (representative images of 300 μm device group shown). Images and image meta-data were processed using two independent methods: (C) using pre-set ROIs, total fluorescent signal from major compartments was captured (in order: stomach, upper small intestine, lower small intestine, cecum, and colon). Fluorescent signal was collected as total photon counts. (D) In parallel, images were processed to extract device distribution information in a continuous manner. Data shown was extracted from images in B. Signal was normalized to the total amount of signal in each sample, and distance was normalized to the total distance of the GI tract sample. Data is presented in a semi-compressed format, where each bar represents the total signal from the preceding 1% of the GI tract. More information on the image processing pipeline in **Figure 4-9**. Produced under license from Biorender.com.

population has spread such that there was no longer a significant difference across groups.

Similarly, in the 450 μm group, at 30 min post gavage there was a statistical difference between

the stomach and the upper and lower small intestine (p=0.037, p=0.037), the cecum (p=0.0085),
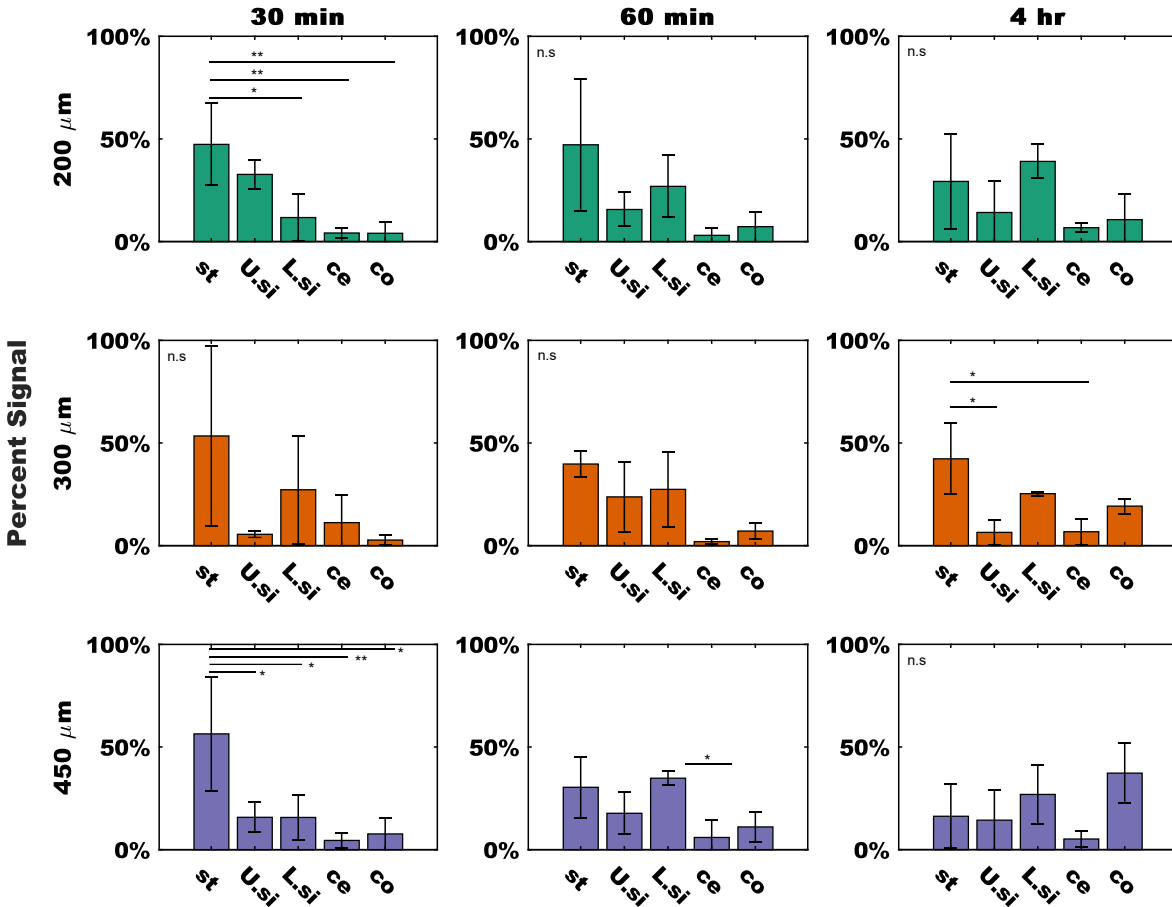
Figure 4-4:
Fluorescent signal from discrete tissue regions demonstrates device transit through tissue. Signals divided by device group (rows) and time (columns). Data was normalized to the total amount of signal in each sample and expressed as a percentage. From the left to right in each plot bars represent signal from the stomach (st), upper small intestine (U.si), lower small intestine (L.si), cecum (ce), and colon (co). Data was expressed as the sample mean ± 1 SD, n = 3 measurements per group for the 200 μm devices (green) and 450 μm devices (purple), n=2 measurements per groups for 300 μm devices (orange). Statistical difference between groups was determined by one-way ANOVA followed by a Tukey-Kramer correction for multiple comparisons. * = p<0.05, ** = p<0.01. ns= no significant differences measured

and the colon (p=0.0128). At 60 min the signal in the lower small intestine of the 450 μm group was significantly higher than the upper small intestine (p=0.029), but there were no other significant differences in any measurement at this time point. By the 4 hr time point, the signal in the stomach of the 300 μm group was significantly higher than both the upper small intestine (p=0.048) and the cecum (p=0.049). In the 200 μm 450 μm groups, by the 4hr time point the particles had dispersed such that there was a similar signal across all measured regions.

Table 4-1:
Dosing for in vivo device transit studies by group. Size measurements represent the mean diameter of n=5 devices, ± 1 SD.

Droplet Number (dp)	Number of Devices (# per animal)	Approximate dose mass (mg total polymer per animal)	Approximate dye mass (µg per animal)	Device Size (µm.d)
10 dp	3120	6.2	18.6	194.6±8
40 dp	2340	18.7	56.1	293.2±7
120 dp	1560	37.4	112.2	440.8±9

Visualization of continuous *in vivo* distributions: IVIS imaging data was processed to produce continuous signal vs distance curves for each device group at each timepoint (**Figure 4-9**).

Figure 4-5 shows the results of visualizing the average distribution of each device geometry at each time point. Each bar represents the sum of the preceding 1% of the data set, in order to better represent the underlying patterns of the volatile data.

In order to link these distribution results to a more rigorous statistical method, we calculated the

cross-correlation coefficients pairwise between each group at each time point, as well as a p-

value associated with that comparison (**Figure 4-6**). In this context, the cross-correlation

coefficients for two vectors can be interpreted as a metric of similarity or goodness-of-fit. Cross-
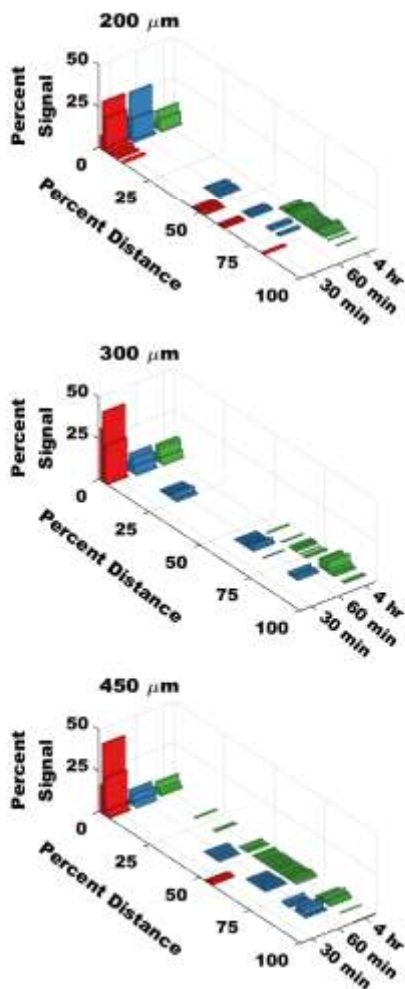
Figure 4-5:
Continuous distributions show device translocation through the GI tract over time.
Signal data was normalized to the total amount of signal in each sample, and
expressed as a percentage. Distance was expressed as a percentage of the total
distance along the GI tract. Each bar represents signal summed over the preceding
1% of the length of the GI tract. Data represents the mean of n=3 separate
measurements for the 200 μm and 450 μm groups, and n=2 separate measurements
for the 300 μm group.
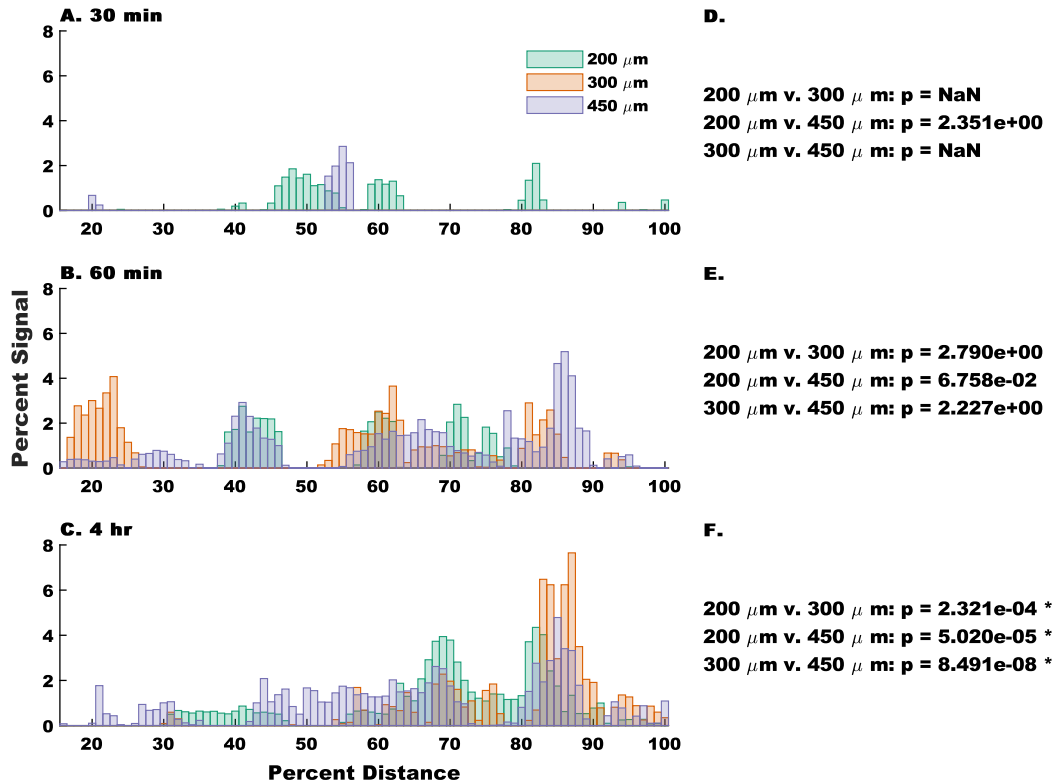
Figure 4-6:
Comparison of distribution signals by-time indicate group stratification. (A-C) Overlays of each device group at 30 min (A,D), 60 min (B,E), and 4hr (C, F) presented after gastric emptying (15%-100% total distance). Signal data is normalized to the total signal present in each sample, and distance is normalized to the total distance along the GI tract. Each bar represents the arithmetic mean of the cumulative signal from the preceding 1% of total distance from n=3 animals for the 200 μm and 450 μm groups, and n=2 animals for the 300 μm group. (D-F) Cross correlation results for pairwise comparisons between groups. P-Values less than p=0.05 represent a statistically significant correlation between the indicated signals, while larger p values fail to reject the null-hypothesis of no correlation. In the 30 min group (E) there was insufficient signal from the 300 μm group for comparison. Family-wise error rate was limited to α=0.05 using a Bonferroni correction for multiple comparisons. * = p < 0.05, and indicates a statistically significant correlation.

correlation coefficients can also be used for hypothesis testing against the null-result of no correlation between the compared signals. When comparing overlayed fluorescence vs. distance signals at each time point between device groups (**Figure 4-6 A-C**), a p-value of less than α = 0.05 indicates significant correlation between the groups, whereas a larger p-value fails to reject the null-hypothesis of no correlation (**Figure 4-6 D-F**). For the purpose of this analysis, we excluded signal from the stomach compartment (~0-15% of total distance) and instead focused on signal from motile devices in the small intestine, cecum, and colon (**Figure 4-9 E**). At 30

min, we observed no correlation between the signal from the 150 μm and 450 μm groups, but due to limited signal in this region from the 300 μm group we were unable to draw any comparisons to that signal. At 60 min, we observed no statistical correlation between any groups, suggesting that all groups present statistically distinct distribution profiles. At 4 hr post gavage, there was a statistically significant correlation between the signals from all device groups, suggesting all groups were similar at $\alpha = 0.05$. Family-wise error rate was limited to $\alpha=0.05$ using a Bonferroni correction for multiple comparisons. These results were further supported by confirming the intragroup correlation between replicates of the same device group and time point (**Figure 4-10**).

Finally, we analyzed the correlation lag between each device group at each time point (**Figure 4-7**). Correlation lag measures the number of discrete steps along the x axis a signal must be shifted to align with a given fixed signal. In this analysis, each lag step equates to shifting the signal backwards (negative) or forwards (positive) one percent of the total distance along the GI tract. In groups in which we were unable to reject the null hypothesis of no correlation, we observed unity peaks at non-zero lags, which indicated that these signals differ in distance along the GI tract. In groups that show significant correlation with one another, we observed unity peaks at 0 lag, showing that the fluorescence vs. distance signals were superimposable to a scalar factor.

4.5. Discussion:

Fluorescent device fabrication: Previously, we reported the use of additive manufacturing to fabricate microdevices of tunable sizes, entirely using materials present in FDA approved oral dosage forms.[204] Here, we build upon that work by leveraging the flexibility and consistency of

the printed microdevice approach in order to fabricate materials that can be used to better understand the transit of microscale drug delivery systems through the GI tract. With this information, we can more rationally design materials to target specific regions of the GI tract or a desired transit time depending on the desired therapeutic profile. Despite the breadth of efforts to
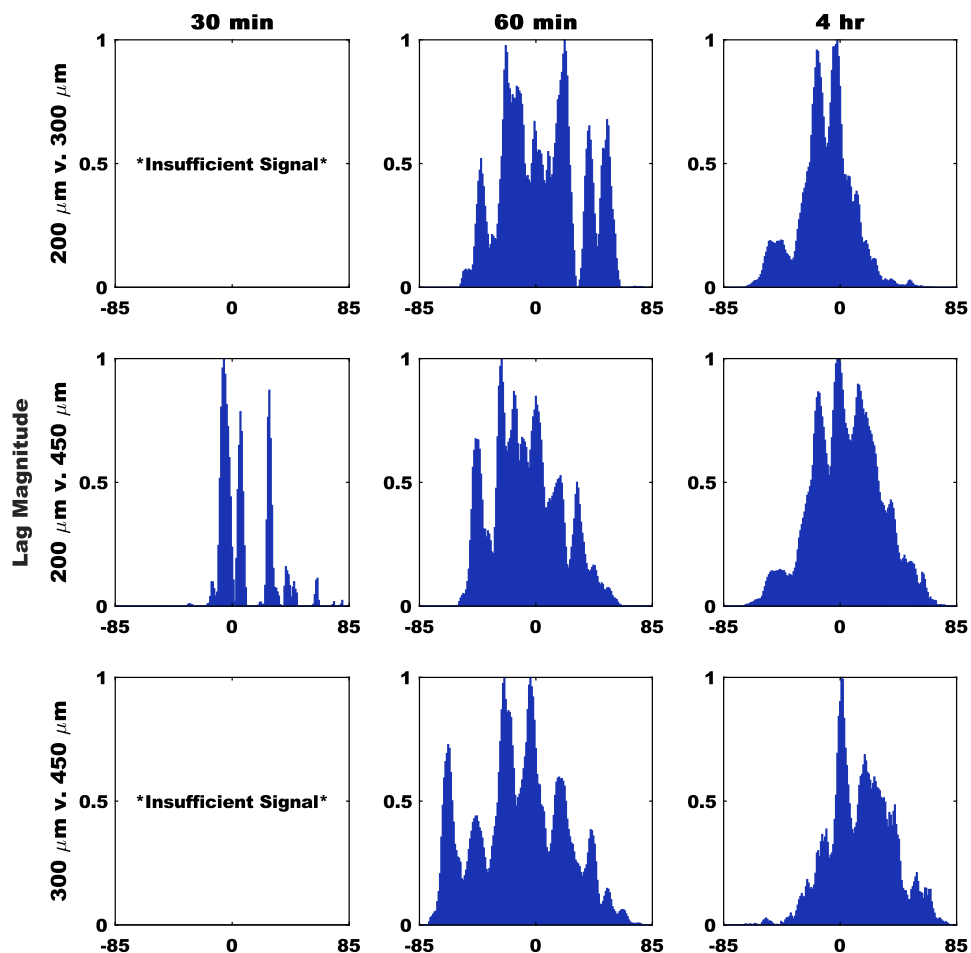
Figure 4-7:
Signal lag shows devices accumulate differentially along the GI tract over time. Biased correlation Lag analysis results presented to account for shifts along the entirety of the analyzed portion of the GI tract (excluding the stomach). Signals were normalized to the maximum in each group. Peaks at positive lag values represent the second term needing to shift in the positive direction to match the first term, while negative lag values indicate the second term moving in the negative direction. Due to insufficient signal, no comparisons to the 300 μm group were possible at the 30 min time point.

develop a microscale device-like system for oral delivery applications, many approaches utilize particles on a similar size scale, between 200-500 μm in diameter.[155,156] The reasons for this

clustering are manyfold, but are most likely tied to the ease of manufacturing particles at this size

scale using photolithography and replica molding.[159] Due to the ease of tunability in our device

printing approach, we were not limited in the same manner. This allowed us the opportunity to

better understand the transit implications of device size, by producing microdevices that

maintained a consistent material profile, but ranged in size by nearly threefold. Other groups

have developed devices for oral delivery using additive manufacturing. These strategies produce

materials on the millimeter scale using micro stereolithography printing, which can achieve more

complex designs, but are limited by the resolution of the instrument, the inflexibility of the CAD

design process, and the necessity of photocrosslinkable materials or specific printer resin

filament.[199,213]

Fluorescence tracking has previously been applied to understand the location of materials in the

gastrointestinal tract and associated tissues.[198,200,206] By conjugating our enteric materials directly

to a near IR fluorophore we reduced the need for disruptive processes, such as microsurgery or

tissue digestion, for detection, which may have otherwise disturbed device placement. As shown

in **Figure 4-2**, the fluorescently labeled microdevices retain their fluorescent signal throughout a

simulated use case, suggesting that there was limited loss of fluorescence intensity through

chemical means or via erosion of the labeled S 100. Eudragit S 100 is a material designed to

erode above pH 7, However, because the murine GI tract never exceeds pH 5, the devices remain

in an intact state.[173,212] The observed stability of the fluorescent microdevices confirms that all

signal observed in the GI tract is related directly to intact devices, and not to eroded polymer or

disassociated free-dye, underlining the utility of these materials in tracking applications in the

murine GI tract.

Regional Device Distributions: In order to understand the impact of microdevice size on transit, we first examined how the accumulation of particles in each tissue compartment varied over time. As shown in **Figure 4-4**, in both the 200 μm and 450 μm groups at the 30 min timepoint, the signal in the stomach was significantly larger than the signal from the more distal compartments. This suggests that devices were still largely retained in the stomach. In the 200 μm group, there was no significant difference between the upper small intestine and stomach groups at 30 min, which suggests that some of the devices may have already emptied into the duodenum. In most samples, there were few differences between groups at the 60 min and 4 hr timepoints, which is indicative of device dispersion throughout the GI tract. In the 450 μm group we observed that there was a difference between the signal in the lower small intestine and the cecum, which suggests that the devices were still largely retained in the small intestine and have not yet permeated to the colon. Alternatively, devices may have entered the colon, but were too large to accumulate in the lower cecum. In the 300 μm group at 4 hr, we observed a significant difference between the signal in the stomach and signal from the upper small intestine and cecum, which again suggests that devices were too large to be retained in the lower cecum, but also indicates that even after 4 hr there was still a significant population of devices that were retained in the stomach. This data as a whole demonstrates that once dosed via oral gavage, devices distribute throughout the GI tract over the course of hours. These results also suggest that smaller devices seem to empty from the stomach faster and distribute more quickly, whereas larger devices were more likely to be retained in the upper portion of the GI tract and stomach, and were unable to access the distended cecum. These results have implications in the potential use cases for planar microdevice delivery platforms in murine disease models. For example, if

larger devices are retained for extended periods in the stomach, they might have applications in extended release or long acting treatments.

Continuous Device Distributions and Quantitative Methods: Most studies investigating particle transit in the GI tract discuss material accumulation and distribution regionally, by summing the signal within a given area, as we have done above. However, utilization of high-resolution fluorescence imaging systems allows us to extract detailed information from images, using image analysis tools, allowing for the correlation of fluorescent signals to their specific location in the GI tract. This level of resolution has implications in further understanding the interaction of materials with local environments in the GI tract, and providing insight into the *in vivo* behavior of microdevices. To accomplish this, we developed an image analysis workflow that extracts the fluorescent data from our tissue imaging samples, and ties it to position data in the GI tract. To account for differences between animals, and for differences in dosing due to particle loss, we expressed our results as a percentage of the total signal observed at a given percent distance along the GI tract. As shown in **Figure 4-5**, we observed devices across the entirety of the GI tract in all device groups. As expected, a larger signal was seen at the proximal side of the GI tract (red bars), that then distributes down the GI tract at later time points (blue and green bars). Given that the average adult murine gastrointestinal tract is 50 cm in length, and given that on average our samples measured approximately 2000 pixels long, we can conclude that a pixel in these images could correspond to as little as 250 μm, or about one device width.[214] The bars in **Figure 4-5** and **Figure 4-6** correspond to a sum of the signal derived from 1% of the total length of the GI tract, or around 20 pixels, meaning that each bar with a non-zero signal likely represents tens of devices.

To more rigorously understand these patterns, we applied cross correlation analysis, as derived from its use in digital signal processing.[215] Cross correlation can be applied to uncover patterns between signals in the same dimensional space. Cross correlation can also be a tool for hypothesis correlation, similar to the Pearson product moment correlation. Specifically, cross-correlation can be used to determine if two signals correlate in a statistically significant manner, or if they fail to reject the null-hypothesis of no correlation. In **Figure 4-6** we observed that, after exiting the stomach, the device signals adopt unique distributions. We confirm this using cross correlation to demonstrate that at 30 min and 1 hr post gavage, different device sizes produce different distributions in the GI tract. By the 4 hr time point, we can no longer distinguish between device groups via cross correlation, which may be due to a concentrated signal near the cecum and colon washing out other signals, or signal loss due to device elimination. This result was further validated by analysis of the intra-group variation (**Figure 4-10**). We show that signals from the same time point and group tend to be well correlated, suggesting that the differences we observed in the cross-correlation analysis in **Figure 4-6** and **Figure 4-7** are due to differences in the behavior of different device sizes, and not due to signal variability. To better understand how our device signals differed, we looked at the lag from our cross-correlation analysis. Correlation lag quantifies a time or space delay between two signals in units of the minimum sampling distance.[216] In the case of our systems, this equates to one percent of the total distance along the GI tract. Correlation lag analysis further confirms that, in the case of planar microdevices, the GI transit rate is inversely correlated with device diameter, as shown by the dominance of positive lag peaks between small and large device groups (**Figure 4-7**). This is likely due to the increased surface area of the larger devices, leading to increased adhesion at the mucosal epithelium. Previously, it was show that the increase in microdevice surface area

through the addition of nanotopographical features, increased residence time, so it follows that a similar increase in device surface area would replicate those results.[185] The one exception we observed is the dominance of negative lag peaks in the 200 μm vs. 450 μm comparison at 60 min post gavage. We speculate that this is the result of the 200 μm devices beginning to be eliminated at this point, effectively reducing the residual signal and shifting the first moment of the signal in the negative direction. In total, these results seem to suggest that until at least 60 min post gavage, the rate of stomach emptying and the rate of device transit through the GI tract, was inversely correlated with device size. In summary, our continuous distribution analysis shows that it is reasonable to assume that microdevices are likely to begin to interact with any specific target location along the murine GI tract within one hour after administration, but as seen in **Figure 4-4**, the extent of this interaction may change from 1 to 4 hr. It is also clear from the presence of multiple discrete peaks in the signal vs distance curve from each group/time point, that devices do not transit in unison, but instead transit as independent particles. These results suggest that in the case of a specific acute local target, such as in the case of acute inflammatory disease, or in the case of specific microbial environments, discrete local areas are likely to encounter multiple devices non-synchronously over the course of many hours. This indicates that instead of doses being applied uniformly over time, doses will be administered in multiple independent bursts. We were unable to capture full device elimination by the 4 hr time point, so it is also reasonable to assume that the residence time of these particles was greater than 4 hr. Residence time is likely also impacted by device size, and so depending on the needs of the delivery application (acute vs. extended dosing), a microdevice diameter can be selected to achieve the desired delivery profile.

Compared to regionalized quantification, our continuous signal approach provides more insight into the specific distribution profile of each microdevice population. The regionalized approach benefits some statistical tests, but can mask underlying patterns in the device distribution. The continuous signal method also functions in an unbiased manner, removing the need to classify or
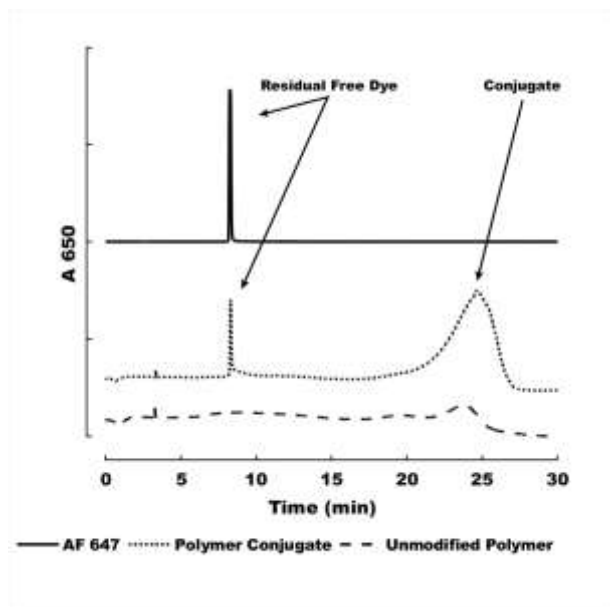
Figure 4-8:
HPLC validation of polymer-dye conjugate product. Dye, polymer conjugate, and unmodified polymer samples were prepared fresh in deionized water, at 100 μg/mL for the free dye and 10 mg/mL for the polymer samples. Free dye was observed to elute at 8.2 min, while the dye conjugate was observed to elute at 24.7 min. Free dye represents less than 3% of total signal in labeled polymer sample. Conjugation efficacy was determined via absorbance at 650 nm of a 1 mg/mL solution of the dye-polymer product, demonstrating the addition of approximately 3 μg of dye per mg of polymer, or the conversion of approximately 37% of the initial dye

demarcate specific regions of the GI tract, and does not depend on a prior understanding of the interaction between the devices and the tissue target in question. We anticipate that, used alongside regional quantification, our continuous signal method will allow researchers to better capture particle level interactions with tissue and unanticipated distribution patterns in an unbiased manner, identifying patterns that may be washed out in ROI-based analysis. We also anticipate that the continuous signal approach will allow researchers to better understand how

their microdevices transit as a population: either in a homogenous group, or as distinct populations, which has implications in application selection as described above.

4.6 Conclusions:

We have demonstrated the fabrication of fluorescently labeled planar microdevices and demonstrated how their size affected transit through the murine GI tract. We produced a covalently labeled polymer product using a set of enteric materials found in many FDA-approved products, and showed that it remained intact in simulated intestinal conditions. Our study of device accumulation in tissue compartments over time shows that particles 300 μm in diameter and larger can remain at least partially in the stomach for hours, while devices 200 μm in diameter are emptied faster. Our results also suggest that device size is inversely correlated with distribution rate, and that devices seem to transit independently of one another as opposed to moving in a uniform mass, meaning that as opposed to reaching a target site in unison, devices are likely to reach a site of action over the course of hours. We also demonstrated the use of a method to quantify the continuous distribution of particles along the GI tract, using image processing and digital signal processing tools. These results support our conclusions from examination of specific tissue regions, and suggest that the majority of device distribution occurs within the first 60 min after dosing, but the kinetics and extent of that distribution are a function of device size. We also see that devices seem to transit individually as opposed to as a homogeneous population, which has implications in the dosing profile of microdevice delivered therapeutics. Our continuous signal analysis also highlights that our devices are retained in the GI tract for longer than 4 hr, but devices 200 μm in diameter and smaller potentially begin elimination by 60 min post dosing. This result will be useful when considering the design of drug delivery systems, and the design considerations of delayed and targeted release platforms. These

results as a whole further inform the parameter space of planar microdevices for oral protein and
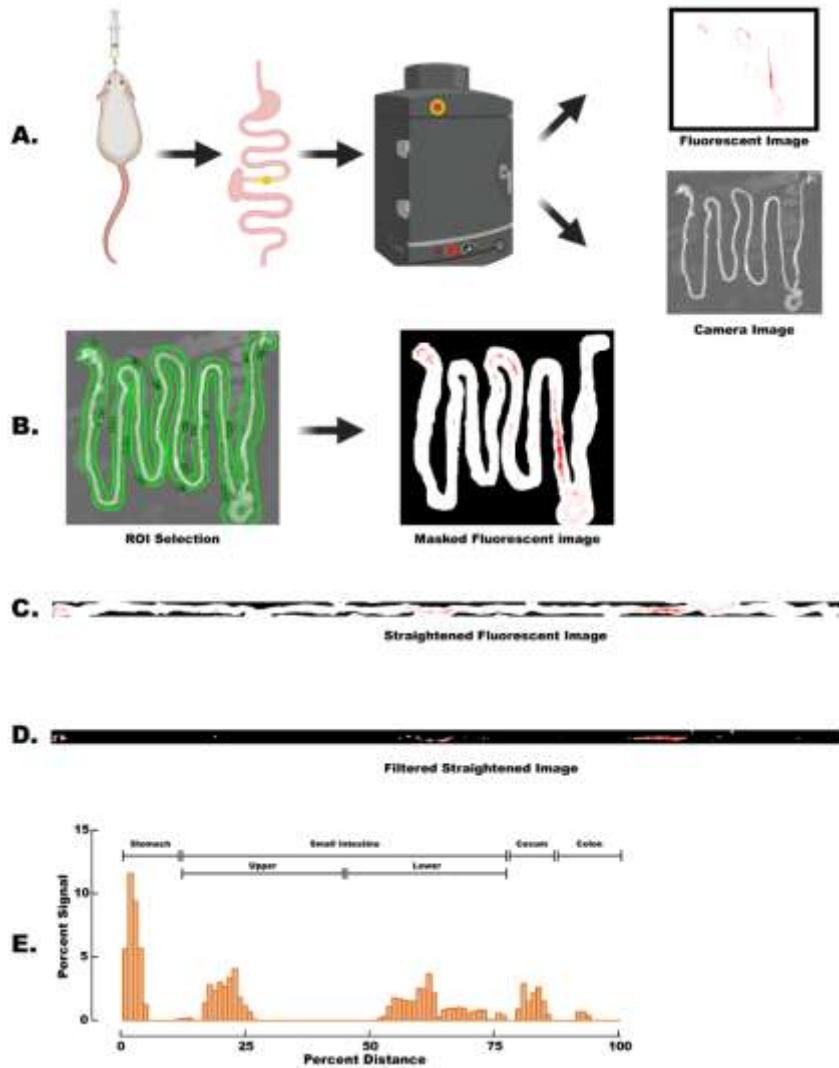

Figure 4-9:
Outline of image analysis pipeline for continuous device tracking. **(A)** After dosing with microdevices via oral-gavage, mice are sacrificed at the specified time points (30 min, 60 min, 4 hr). Extracted GI tracts were imaged using a Xeogen Spectrum imaging system, using the standard AF 647 filter set, adjusting the f-stop of the CCD to 1 to increase sensitivity. Imaging each sample produces two distinct images: a digital photograph of the tissue, and a monochromatic trace of the fluorescent signal. **(B)** Using MatLab scripting, a region of interest (ROI) is traced onto the photograph (by hand), and then applied to the fluorescent image, producing the masked image shown. **(C)** Applying an integrated ImageJ instance within the MatLab script, the ROI from the masked fluorescent image is selected and straightened as shown, to produce an image of a constant width that captures the entirety of the GI tract. **(D)** The straightened image is imported back into the MatLab instance, and filtered to remove any pixels not containing red signal using an orthogonal YCbCr color space mask. The RGB image is further processed (not shown) to a mono-chromatic format, leaving only the red channel. **(E)** The resulting matrix of pixel values is summed column-wise to produce a one-dimensional vector of signal information. This data is normalized by the total signal present in the given animal, and plotted as normalized percent signal vs. percent distance along the GI tract. Further, to mitigate some of the inherent volatility in the signal and preserve the inherent patterns in the data, it is compressed in a lossless manner, such that each datapoint represents the sum of signal present in the preceding 1% of the GI tract. On average, the stomach represents the first 15% of the signal, the small intestine the next 60% (split evenly between the upper and lower small intestine), the cecum the next 10%, and the colon the final 15%. Produced under license from Biorender.com.

100

small molecule delivery, and will enable informed decision making in the development of pre-

clinical and clinical products.
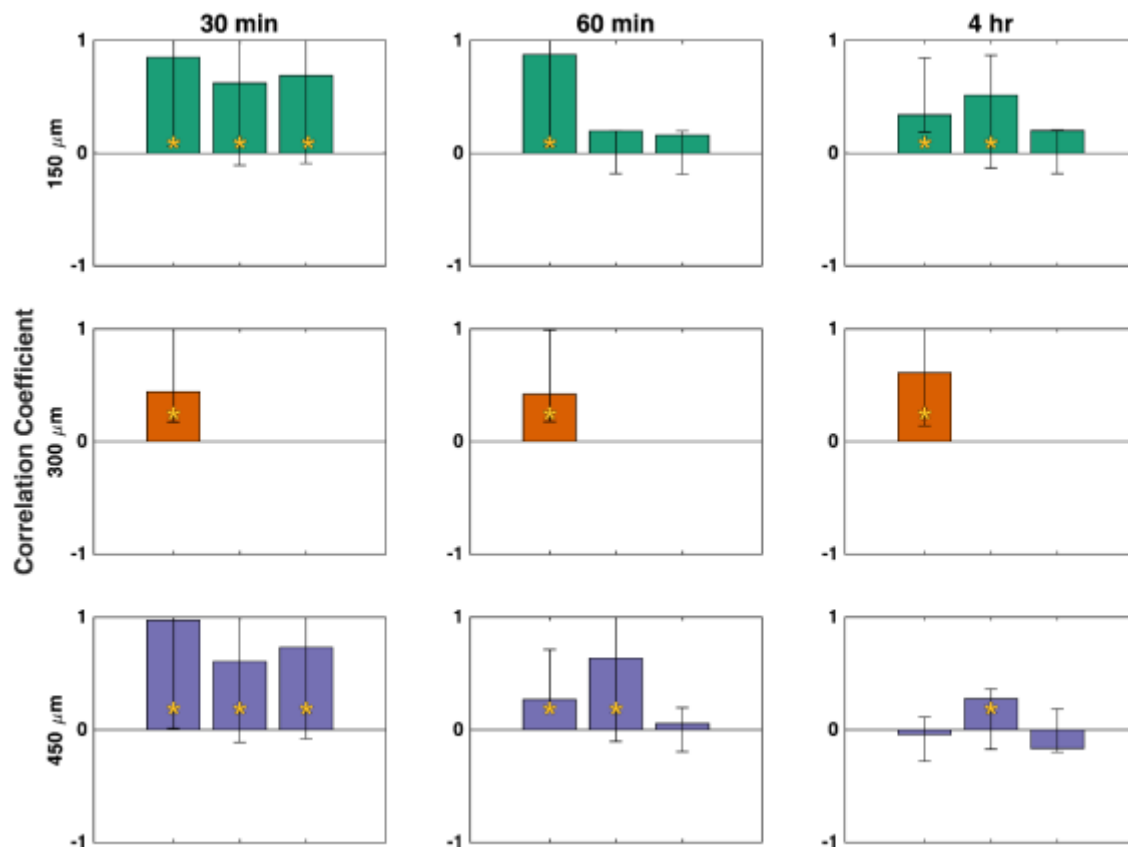
Figure 4-10:
Cross-correlation coefficients from pair wise intragroup comparisons of signal vs distance data. Each bar represents one pairwise comparison between two distinct signals, error bars represent the bounds of the 95% confidence interval of the correlation coefficient. Bars marked with * successfully reject the null-hypothesis of no correlation at $\alpha = 0.05$. Unmarked groups fail to reject the null-hypothesis of no correlation between signals. To limit the family wise error rate, p-values were adjusted using a Bonferroni correction for multiple comparisons.

References.

(1)   UNAIDS. *AIDS By the Numbers*; Geneva, Switzerland, 2016.

(2)   Baeten, J. M.; Donnell, D.; Ndase, P.; Mugo, N. R.; Campbell, J. D.; Wangisi, J.; Tappero, J. W.; Bukusi, E. A.; Cohen, C. R.; Katabira, E.; Ronald, A.; Tumwesigye, E.; Were, E.; Fife, K. H.; Kiarie, J.; Farquhar, C.; John-Stewart, G.; Kakia, A.; Odoyo, J.; Mucunguzi, A.; Nakku-Joloba, E.; Twesigye, R.; Ngure, K.; Apaka, C.; Tamooh, H.; Gabona, F.; Mujugira, A.; Panteleeff, D.; Thomas, K. K.; Kidoguchi, L.; Krows, M.; Revall, J.; Morrison, S.; Haugen, H.; Emmanuel-Ogier, M.; Ondrejcek, L.; Coombs, R. W.; Frenkel, L.; Hendrix, C.; Bumpus, N. N.; Bangsberg, D.; Haberer, J. E.; Stevens, W. S.; Lingappa, J. R.; Celum, C. Antiretroviral Prophylaxis for HIV Prevention in Heterosexual Men and Women. *N. Engl. J. Med.* **2012**, 120711140017009. https://doi.org/10.1056/NEJMoa1108524.

(3)   Thigpen, M. C.; Kebaabetswe, P. M.; Paxton, L. a.; Smith, D. K.; Rose, C. E.; Segolodi, T. M.; Henderson, F. L.; Pathak, S. R.; Soud, F. a.; Chillag, K. L.; Mutanhaurwa, R.; Chirwa, L. I.; Kasonde, M.; Abebe, D.; Buliva, E.; Gvetadze, R. J.; Johnson, S.; Sukalac, T.; Thomas, V. T.; Hart, C.; Johnson, J. a.; Malotte, C. K.; Hendrix, C. W.; Brooks, J. T. Antiretroviral Preexposure Prophylaxis for Heterosexual HIV Transmission in Botswana. *N. Engl. J. Med.* **2012**, *367* (5), 423–434. https://doi.org/10.1056/NEJMoa1110711.

(4)   Choopanya, K.; Martin, M.; Suntharasamai, P.; Sangkum, U.; Mock, P. A.; Leethochawalit, M.; Chiamwongpaet, S.; Kitisin, P.; Natrujirote, P.; Kittimunkong, S.; Chuachoowong, R.; Gvetadze, R. J.; McNicholl, J. M.; Paxton, L. A.; Curlin, M. E.; Hendrix, C. W.; Vanichseni, S. Antiretroviral Prophylaxis for HIV Infection in Injecting

Drug Users in Bangkok, Thailand (the Bangkok Tenofovir Study): A Randomised, Double-Blind, Placebo-Controlled Phase 3 Trial. *Lancet* **2013**, *381* (9883), 2083–2090. https://doi.org/10.1016/S0140-6736(13)61127-7.

(5)   Marrazzo, J. M.; Ramjee, G.; Richardson, B. A.; Gomez, K.; Mgodi, N.; Nair, G.; Palanee, T.; Nakabiito, C.; van der Straten, A.; Noguchi, L.; Hendrix, C. W.; Dai, J. Y.; Ganesh, S.; Mkhize, B.; Taljaard, M.; Parikh, U. M.; Piper, J.; Mâsse, B.; Grossman, C.; Rooney, J.; Schwartz, J. L.; Watts, H.; Marzinke, M. A.; Hillier, S. L.; McGowan, I. M.; Chirenje, Z. M. Tenofovir-Based Preexposure Prophylaxis for HIV Infection among African Women. *N. Engl. J. Med.* **2015**, *372* (6), 509–518. https://doi.org/10.1056/NEJMoa1402269.

(6)   Grant, R. M.; Lama, J. R.; Anderson, P. L.; McMahan, V.; Liu, A. Y.; Vargas, L.; Goicochea, P.; Casapía, M.; Guanira-Carranza, J. V.; Ramirez-Cardich, M. E.; Montoya-Herrera, O.; Fernández, T.; Veloso, V. G.; Buchbinder, S. P.; Chariyalertsak, S.; Schechter, M.; Bekker, L.-G.; Mayer, K. H.; Kallás, E. G.; Amico, K. R.; Mulligan, K.; Bushman, L. R.; Hance, R. J.; Ganoza, C.; Defechereux, P.; Postle, B.; Wang, F.; McConnell, J. J.; Zheng, J.-H.; Lee, J.; Rooney, J. F.; Jaffe, H. S.; Martinez, A. I.; Burns, D. N.; Glidden, D. V. Preexposure Chemoprophylaxis for HIV Prevention in Men Who Have Sex with Men. *N. Engl. J. Med.* **2010**, *363* (27), 2587–2599. https://doi.org/10.1056/NEJMoa1011205.

(7)   Cottrell, M. L.; Yang, K. H.; Prince, H. M. A.; Sykes, C.; White, N.; Malone, S.; Dellon, E. S.; Madanick, R. D.; Shaheen, N. J.; Hudgens, M. G.; Wulff, J.; Patterson, K. B.; Nelson, J. A. E.; Kashuba, A. D. M. A Translational Pharmacology Approach to Predicting Outcomes of Preexposure Prophylaxis Against HIV in Men and Women Using

Tenofovir Disoproxil Fumarate with or Without Emtricitabine. *J. Infect. Dis.* **2016**, *214* (1), 55–64. https://doi.org/10.1093/infdis/jiw077.

(8)   Dezzutti, C. S.; Hendrix, C. W.; Marrazzo, J. M.; Pan, Z.; Wang, L.; Louissaint, N.; Kalyoussef, S.; Torres, N. M.; Hladik, F.; Parikh, U.; Mellors, J.; Hillier, S. L.; Herold, B. C. Performance of Swabs, Lavage, and Diluents to Quantify Biomarkers of Female Genital Tract Soluble Mucosal Mediators. *PLoS One* **2011**, *6* (8). https://doi.org/10.1371/journal.pone.0023136.

(9)   Van Damme, L.; Corneli, a; Ahmed, K.; Agot, K.; Lombaard, J.; Kapiga, S.; Malahleha, M.; Owino, F.; Manongi, R.; Onyango, J.; Temu, L.; Monedi, M. C.; Mak'Oketch, P.; Makanda, M.; Reblin, I.; Makatu, S. E.; Saylor, L.; Kiernan, H.; Kirkendale, S.; Wong, C.; Grant, R.; Kashuba, a; Nanda, K.; Mandala, J.; Fransen, K.; Deese, J.; Crucitti, T.; Mastro, T. D.; Taylor, D. Preexposure Prophylaxis for HIV Infection among African Women. *N Engl J Med* **2012**, *367* (5), 411–422. https://doi.org/10.1056/NEJMoa1202614.

(10)   Hickey, M. B.; Merisko-Liversidge, E.; Remenar, J. F.; Namchuk, M. Delivery of Long-Acting Injectable Antivirals. *Curr. Opin. Infect. Dis.* **2015**, *28* (6), 1. https://doi.org/10.1097/QCO.0000000000000214.

(11)   Landovitz, R. J.; Grinsztejn, B. Long-Acting Injectable Preexposure Prophylaxis for HIV Prevention in South Africa: Is There a Will and a Way? *J. Infect. Dis.* **2016**, *213* (10), 1519–1520. https://doi.org/10.1093/infdis/jiv524.

(12)   Owen, A.; Rannard, S. Strengths, Weaknesses, Opportunities and Challenges for Long Acting Injectable Therapies: Insights for Applications in HIV Therapy. *Adv. Drug Deliv. Rev.* **2016**, *103*, 144–156. https://doi.org/10.1016/j.addr.2016.02.003.

(13)   Boffito, M.; Jackson, A.; Owen, A.; Becker, S. New Approaches to Antiretroviral Drug Delivery: Challenges and Opportunities Associated with the Use of Long-Acting Injectable Agents. *Drugs* **2014**, *74* (1), 7–13. https://doi.org/10.1007/s40265-013-0163-7.

(14)   Krakower, D. S.; Mayer, K. H. Pre-Exposure Prophylaxis to Prevent HIV Infection: Current Status, Future Opportunities and Challenges. *Drugs* **2015**, *75* (3), 243–251. https://doi.org/10.1007/s40265-015-0355-4.

(15)   Myers, J. E.; Ellman, T. M.; Westhoff, C. Injectable Agents for Pre-Exposure Prophylaxis: Lessons Learned from Contraception to Inform HIV Prevention. *Curr. Opin. HIV AIDS* **2015**, *10* (4), 271–277. https://doi.org/10.1097/COH.0000000000000166.

(16)   Nelson, A. G.; Zhang, X.; Ganapathi, U.; Szekely, Z.; Flexner, C. W.; Owen, A.; Sinko, P. J. Drug Delivery Strategies and Systems for HIV/AIDS Pre-Exposure Prophylaxis and Treatment. *J. Control. Release* **2015**, *219* (2015), 669–680. https://doi.org/10.1016/j.jconrel.2015.08.042.

(17)   Spreen, W. R.; Margolis, D. a; Pottage, J. C. Long-Acting Injectable Antiretrovirals for HIV Treatment and Prevention. *Curr. Opin. HIV AIDS* **2013**, *8* (6), 565–571. https://doi.org/10.1097/COH.0000000000000002.

(18)   Parsons, J. T.; Rendina, H. J.; Whitfield, T. H. F.; Grov, C. Familiarity with and Preferences for Oral and Long-Acting Injectable HIV Pre-Exposure Prophylaxis (PrEP) in a National Sample of Gay and Bisexual Men in the U.S. *AIDS Behav.* **2016**, *20* (7), 1390–1399. https://doi.org/10.1007/s10461-016-1370-5.

(19)   Luecke, E. H.; Cheng, H.; Woeber, K.; Nakyanzi, T.; Mudekunye-Mahaka, I. C.; van der Straten, A. Stated Product Formulation Preferences for HIV Pre-Exposure Prophylaxis

among Women in the VOICE-D (MTN-003D) Study. *J. Int. AIDS Soc.* **2016**, *19* (1), 1–9. https://doi.org/10.7448/IAS.19.1.20875.

(20)   Eisingerich, A. B.; Wheelock, A.; Gomez, G. B.; Garnett, G. P.; Dybul, M. R.; Piot, P. K. Attitudes and Acceptance of Oral and Parenteral HIV Preexposure Prophylaxis among Potential User Groups: A Multinational Study. *PLoS One* **2012**, *7* (1), 1–11. https://doi.org/10.1371/journal.pone.0028238.

(21)   Spreen, W.; Williams, P.; Margolis, D.; Ford, S. L.; Crauwels, H.; Lou, Y.; Gould, E.; Stevens, M.; Piscitelli, S. Pharmacokinetics, Safety, and Tolerability With Repeat Doses of GSK1265744 and Rilpivirine (TMC278) Long-Acting Nanosuspensions in Healthy Adults. *J. Acquir. Immune Defic. Syndr.* **2014**, *67* (5), 487–492. https://doi.org/10.1097/QAI.0000000000000365.

(22)   Cortez, J. M.; Quintero, R.; Moss, J. A.; Beliveau, M.; Smith, T. J.; Baum, M. M. Pharmacokinetics of Injectable, Long-Acting Nevirapine for HIV Prophylaxis in Breastfeeding Infants. *Antimicrob. Agents Chemother.* **2015**, *59* (1), 59–66. https://doi.org/10.1128/AAC.03906-14.

(23)   Kalepu, S.; Nekkanti, V. Improved Delivery of Poorly Soluble Compounds Using Nanoparticle Technology : A Review. *Drug Deliv. Transl. Res.* **2016**, 319–332. https://doi.org/10.1007/s13346-016-0283-1.

(24)   Rabinow, B. E. Nanosuspensions in Drug Delivery. *Nat. Rev. Drug Discov.* **2004**, *3* (9), 785–796. https://doi.org/10.1038/nrd1494.

(25)   Na, G. C.; Stevens, H. J.; Yuan, B. O.; Rajagopalan, N. Physical Stability of Ethyl Diatrizoate Nanocrystalline Suspension in Steam Sterilization. *Pharmaceutical research*.

1999, pp 569–574. https://doi.org/10.1023/A:1018883431970.

(26) Yadollahi, R.; Vasilev, K.; Simovic, S. Nanosuspension Technologies for Delivery of Poorly Soluble Drugs. *J. Nanomater.* **2015**, *2015* (iii), 1–13. https://doi.org/10.1155/2015/216375.

(27) Merisko-Liversidge, E. M.; Liversidge, G. G. Drug Nanoparticles: Formulating Poorly Water-Soluble Compounds. *Toxicol. Pathol.* **2008**, *36* (1), 43–48. https://doi.org/10.1177/0192623307310946.

(28) Merisko-Liversidge, E.; Liversidge, G. G.; Cooper, E. R. Nanosizing: A Formulation Approach for Poorly-Water-Soluble Compounds. *Eur. J. Pharm. Sci.* **2003**, *18* (2), 113–120. https://doi.org/10.1016/S0928-0987(02)00251-8.

(29) ZILLER, K.; RUPPRECHT, H. CONTROL OF CRYSTAL-GROWTH IN DRUG SUSPENSIONS .2. INFLUENCE OF POLYMERS ON DISSOLUTION AND CRYSTALLIZATION DURING TEMPERATURE CYCLING. *Pharm. Ind.* **1990**, *52* (8), 1017–1022.

(30) Keck, C. M.; Müller, R. H. Drug Nanocrystals of Poorly Soluble Drugs Produced by High Pressure Homogenisation. *Eur. J. Pharm. Biopharm.* **2006**, *62* (1), 3–16. https://doi.org/10.1016/j.ejpb.2005.05.009.

(31) Gao, L.; Zhang, D.; Chen, M. Drug Nanocrystals for the Formulation of Poorly Soluble Drugs and Its Application as a Potential Drug Delivery System. *J. Nanoparticle Res.* **2008**, *10* (5), 845–862. https://doi.org/10.1007/s11051-008-9357-4.

(32) Zuidema, J.; Pieters, F. A. J. M.; Duchateau, G. S. M. J. E. Release and Absorption Rate

Aspects of Intramuscularly Injected Pharmaceuticals. *Int. J. Pharm.* **1988**, *47* (1–3), 1–12. https://doi.org/10.1016/0378-5173(88)90209-8.

(33)   Stout, P. J. M.; Khoury, N.; Howard, S. A.; Mauger, J. W. Dissolution Performance Related to Particle Size Distribution for Cohpiercially Available Prednisolone Acetate Suspensions. *Drug Dev. Ind. Pharm.* **1992**, *18* (4), 395–408. https://doi.org/10.3109/03639049209043860.

(34)   Theis, J. G.; Liau-Chu, M.; Chan, H. S.; Doyle, J.; Greenberg, M. L.; Koren, G. Anaphylactoid Reactions in Children Receiving High-Dose Intravenous Cyclosporine for Reversal of Tumor Resistance: The Causative Role of Improper Dissolution of Cremophor EL. *J. Clin. Oncol.* **1995**, *13* (10), 2508–2516. https://doi.org/10.1200/JCO.1995.13.10.2508.

(35)   Boedeker, B. H.; Lojeski, E. W.; Kline, M. D.; Haynes, D. H. Ultra-Long-Duration Local Anesthesia Produced by Injection of Lecithin-Coated Tetracaine Microcrystals. *J. Clin. Pharmacol.* **1994**, *34* (6), 699–702. https://doi.org/10.1002/j.1552-4604.1994.tb02026.x.

(36)   Rajoli, R. K. R.; Back, D. J.; Rannard, S.; Freel Meyers, C. L.; Flexner, C.; Owen, A.; Siccardi, M. Physiologically Based Pharmacokinetic Modelling to Inform Development of Intramuscular Long-Acting Nanoformulations for HIV. *Clin. Pharmacokinet.* **2015**, *54* (6), 639–650. https://doi.org/10.1007/s40262-014-0227-1.

(37)   Andrews, C. D.; Heneine, W. Cabotegravir Long-Acting for HIV-1 Prevention. *Curr. Opin. HIV AIDS* **2015**, *10* (4), 258–263. https://doi.org/10.1097/COH.0000000000000161.

(38)   Williams, P. E.; Crauwels, H. M.; Basstanie, E. D. Formulation and Pharmacology of Long-Acting Rilpivirine. *Curr Opin HIV AIDS* **2015**, *10* (4), 233–238.

https://doi.org/10.1097/COH.0000000000000164.

(39)   Kovarova, M.; Swanson, M. D.; Sanchez, R. I.; Baker, C. E.; Steve, J.; Spagnuolo, R. A.; Howell, B. J.; Hazuda, D. J.; Garcia, J. V. A Long-Acting Formulation of the Integrase Inhibitor Raltegravir Protects Humanized BLT Mice from Repeated High-Dose Vaginal HIV Challenges. *J. Antimicrob. Chemother.* **2016**, No. March, 1–11. https://doi.org/10.1093/jac/dkw042.

(40)   Yoshinaga, T.; Kobayashi, M.; Seki, T.; Miki, S.; Wakasa-Morimoto, C.; Suyama-Kagitani, A.; Kawauchi-Miki, S.; Taishi, T.; Kawasuji, T.; Johns, B. A.; Underwood, M. R.; Garvey, E. P.; Sato, A.; Fujiwara, T. Antiviral Characteristics of GSK1265744, an HIV Integrase Inhibitor Dosed Orally or by Long-Acting Injection. *Antimicrob. Agents Chemother.* **2015**, *59* (1), 397–406. https://doi.org/10.1128/AAC.03909-14.

(41)   Spreen, W.; Min, S.; Ford, S. L.; Chen, S.; Lou, Y.; Bomar, M.; St Clair, M.; Piscitelli, S.; Fujiwara, T. Pharmacokinetics, Safety, and Monotherapy Antiviral Activity of GSK1265744, an HIV Integrase Strand Transfer Inhibitor. *HIV Clin. Trials* **2014**, *14* (5), 192–203. https://doi.org/10.1310/hct1405-192.

(42)   Spreen, W.; Ford, S. L.; Chen, S.; Wilfret, D.; Margolis, D.; Gould, E.; Piscitelli, S. GSK1265744 Pharmacokinetics in Plasma and Tissue After Single-Dose Long-Acting Injectable Administration in Healthy Subjects. *JAIDS J. Acquir. Immune Defic. Syndr.* **2014**, *67* (5), 481–486. https://doi.org/10.1097/QAI.0000000000000301.

(43)   van 't Klooster, G.; Hoeben, E.; Borghys, H.; Looszova, A.; Bouche, M. P.; van Velsen, F.; Baert, L. Pharmacokinetics and Disposition of Rilpivirine (TMC278) Nanosuspension as a Long-Acting Injectable Antiretroviral Formulation. *Antimicrob. Agents Chemother.*

2010, *54* (5), 2042–2050. https://doi.org/10.1128/AAC.01529-09.

(44)   Mordant, C.; Schmitt, B.; Pasquier, E.; Demestre, C.; Queguiner, L.; Masungi, C.; Peeters, A.; Smeulders, L.; Bettens, E.; Hertogs, K.; Heeres, J.; Lewi, P.; Guillemont, J. Synthesis of Novel Diarylpyrimidine Analogues of TMC278 and Their Antiviral Activity against HIV-1 Wild-Type and Mutant Strains. *Eur. J. Med. Chem.* **2007**, *42* (5), 567–579. https://doi.org/10.1016/j.ejmech.2006.11.014.

(45)   Goebel, F. .; Yakovlev, A. .; Pozniak, A. L. .; Vinogradova, E. .; Boogaerts, G. .; Hoetelmans, R. .; De Béthune, M.-P. P. .; Peeters, M. .; Woodfall, B. . f. Short-Term Antiviral Activity of TMC278 - A Novel NNRTI - In Treatment-Naive HIV-1-Infected Subjects. *Aids* **2006**, *20* (13), 1721–1726. https://doi.org/10.1097/01.aids.0000242818.65215.bd.

(46)   Baert, L.; van 't Klooster, G.; Dries, W.; François, M.; Wouters, A.; Basstanie, E.; Iterbeke, K.; Stappers, F.; Stevens, P.; Schueller, L.; Van Remoortere, P.; Kraus, G.; Wigerinck, P.; Rosier, J. Development of a Long-Acting Injectable Formulation with Nanoparticles of Rilpivirine (TMC278) for HIV Treatment. *Eur. J. Pharm. Biopharm.* **2009**, *72* (3), 502–508. https://doi.org/10.1016/j.ejpb.2009.03.006.

(47)   Jackson, A.; McGowan, I. Long-Acting Rilpivirine for HIV Prevention. *Curr Opin HIV AIDS* **2015**, *10* (4), 253–257. https://doi.org/10.1097/COH.0000000000000160.

(48)   McGowan, I.; Dezzutti, C. S.; Siegel, A.; Engstrom, J.; Nikiforov, A.; Duffill, K.; Shetler, C.; Richardson-Harman, N.; Abebe, K.; Back, D.; Else, L.; Egan, D.; Khoo, S.; Egan, J. E.; Stall, R.; Williams, P. E.; Rehman, K. K.; Adler, A.; Brand, R. M.; Chen, B.; Achilles, S.; Cranston, R. D. Long-Acting Rilpivirine as Potential Pre-Exposure Prophylaxis for

HIV-1 Prevention (the MWRI-01 Study): An Open-Label, Phase 1, Compartmental, Pharmacokinetic and Pharmacodynamic Assessment. *Lancet HIV* **2016**, *3018* (16), 1–10. https://doi.org/10.1016/S2352-3018(16)30113-8.

(49)   McGowan, I. Injectable and Implantable Antiretroviral Strategies for HIV Prevention. *Future Virol.* **2015**, *10* (10), 1163–1176. https://doi.org/10.2217/fvl.15.83.

(50)   Gautam, R.; Nishimura, Y.; Pegu, A.; Nason, M. C.; Klein, F.; Gazumyan, A.; Golijanin, J.; Buckler-White, A.; Sadjadpour, R.; Wang, K.; Mankoff, Z.; Schmidt, S. D.; Lifson, J. D.; Mascola, J. R.; Nussenzweig, M. C.; Martin, M. A. A Single Injection of Anti-HIV-1 Antibodies Protects against Repeated SHIV Challenges. *Nature* **2016**, *533* (7601), 105–109. https://doi.org/10.1038/nature17677.

(51)   Saunders, K. O.; Pegu, A.; Georgiev, I. S.; Zeng, M.; Joyce, M. G.; Yang, Z.-Y.; Ko, S.-Y.; Chen, X.; Schmidt, S. D.; Haase, A. T.; Todd, J.-P.; Bao, S.; Kwong, P. D.; Rao, S. S.; Mascola, J. R.; Nabel, G. J. Sustained Delivery of a Broadly Neutralizing Antibody in Nonhuman Primates Confers Long-Term Protection against Simian/Human Immunodeficiency Virus Infection. *J. Virol.* **2015**, *89* (11), 5895–5903. https://doi.org/10.1128/JVI.00210-15.

(52)   Sun, M.; Li, Y.; Yuan, Z.; Lu, W.; Kang, G.; Fan, W.; Li, Q. VRC01 Antibody Protects against Vaginal and Rectal Transmission of Human Immunodeficiency Virus 1 in Hu-BLT Mice. *Arch. Virol.* **2016**, *161* (9), 2449–2455. https://doi.org/10.1007/s00705-016-2942-4.

(53)   Ledgerwood, J. E.; Coates, E. E.; Yamshchikov, G.; Saunders, J. G.; Holman, L.; Enama, M. E.; Dezure, A.; Lynch, R. M.; Gordon, I.; Plummer, S.; Hendel, C. S.; Pegu, A.;

Conan-Cibotti, M.; Sitar, S.; Bailer, R. T.; Narpala, S.; McDermott, A.; Louder, M.; O'Dell, S.; Mohan, S.; Pandey, J. P.; Schwartz, R. M.; Hu, Z.; Koup, R. A.; Capparelli, E.; Mascola, J. R.; Graham, B. S.; Mendoza, F.; Novik, L.; Zephir, K.; Whalen, W.; Larkin, B.; Vasilenko, O.; Berkowitz, N.; Wilson, B.; Pittman, I.; Schieber, G.; Decederfelt, H.; Starling, J.; Gilly, J.; Rao, S.; Kaltovich, F.; Renehan, P.; Kunchai, M.; Romano, S.; Menard, K.; Diep, L.; Anude, C.; Allen, M. Safety, Pharmacokinetics and Neutralization of the Broadly Neutralizing HIV-1 Human Monoclonal Antibody VRC01 in Healthy Adults. *Clin. Exp. Immunol.* **2015**, *182* (3), 289–301. https://doi.org/10.1111/cei.12692.

(54) Whaley, K. J.; Zeitlin, L. Antibody-Based Concepts for Multipurpose Prevention Technologies. *Antiviral Res.* **2013**, *100*, S48–S53. https://doi.org/10.1016/j.antiviral.2013.09.027.

(55) Cheeseman, H. M.; Olejniczak, N. J.; Rogers, P. M.; L King, D. F.; Ziprin, P.; Liao, H.-X.; Haynes, B. F.; Shattock, R. J. Broadly Neutralising Antibodies Display Superior Potential Over Non- 1 Neutralising Antibodies in Preventing HIV-1 Infection of Mucosal Tissue 2 3 Running Title: Mucosal HIV-1 Antibody Inhibition 4 5. **2016**, No. October. https://doi.org/10.1128/JVI.01762-16.

(56) Zalevsky, J.; Chamberlain, A. K.; Horton, H. M.; Karki, S.; Leung, I. W. L.; Sproule, T. J.; Lazar, G. A.; Roopenian, D. C.; Desjarlais, J. R. Enhanced Antibody Half-Life Improves in Vivo Activity. *Nat. Biotechnol.* **2010**, *28* (2), 157–159. https://doi.org/10.1038/nbt.1601.

(57) Dall'Acqua, W. F.; Kiener, P. A.; Wu, H. Properties of Human IgG1s Engineered for Enhanced Binding to the Neonatal Fc Receptor (FcRn). *J. Biol. Chem.* **2006**, *281* (33),

23514–23524. https://doi.org/10.1074/jbc.M604292200.

(58) Warne, N. W. Development of High Concentration Protein Biopharmaceuticals: The Use of Platform Approaches in Formulation Development. *Eur. J. Pharm. Biopharm.* **2011**, *78* (2), 208–212. https://doi.org/10.1016/j.ejpb.2011.03.004.

(59) Hoffman, A. S. The Origins and Evolution of "Controlled" Drug Delivery Systems. *J. Control. Release* **2008**, *132* (3), 153–163. https://doi.org/10.1016/j.jconrel.2008.08.012.

(60) Brambilla, D.; Luciani, P.; Leroux, J. C. Breakthrough Discoveries in Drug Delivery Technologies: The next 30 Years. *J. Control. Release* **2014**, *190*, 9–14. https://doi.org/10.1016/j.jconrel.2014.03.056.

(61) Stevenson, C. L.; Santini, J. T.; Langer, R. Reservoir-Based Drug Delivery Systems Utilizing Microtechnology. *Adv. Drug Deliv. Rev.* **2012**, *64* (14), 1590–1602. https://doi.org/10.1016/j.addr.2012.02.005.

(62) Anselmo, A. C.; Mitragotri, S. An Overview of Clinical and Commercial Impact of Drug Delivery Systems. *J. Control. Release* **2014**, *190*, 15–28. https://doi.org/10.1016/j.jconrel.2014.03.053.

(63) Park, K. Controlled Drug Delivery Systems: Past Forward and Future Back. *J. Control. Release* **2014**, *190*, 3–8. https://doi.org/10.1016/j.jconrel.2014.03.054.

(64) Solorio, L.; Carlson, A.; Zhou, H.; Exner, A. A. Implantable Drug Delivery Systems. In *Engineering Polymer Systems for Improved Drug Delivery*; John Wiley & Sons, Inc.: Hoboken, NJ, USA, 2014; pp 189–225. https://doi.org/10.1002/9781118747896.ch7.

(65) Lewis, K. a; Goldyn, A. K.; West, K. W.; Eugster, E. a. A Single Histrelin Implant Is

Effective for 2 Years for Treatment of Central Precocious Puberty. *J. Pediatr.* **2013**, *163* (4), 1214–1216. https://doi.org/10.1016/j.jpeds.2013.05.033.

(66) Wenzl, R.; Van Beek, A.; Schnabel, P.; Huber, J. Pharmacokinetics of Etonogestrel Released from the Contraceptive Implant Implanon®. *Contraception* **1998**, *58* (5), 283–288. https://doi.org/10.1016/S0010-7824(98)00110-3.

(67) Palomba, S.; Falbo, A.; Di Cello, A.; Materazzo, C.; Zullo, F. Nexplanon: The New Implant for Long-Term Contraception. A Comprehensive Descriptive Review. *Gynecol. Endocrinol.* **2012**, *28* (9), 710–721. https://doi.org/10.3109/09513590.2011.652247.

(68) Ritger, P. L.; Peppas, N. a. A Simple Equation for Description of Solute Release I. Fickian and Non-Fickian Release from Non-Swellable Devices in the Form of Slabs, Spheres, Cylinders or Discs. *J. Control. Release* **1987**, *5* (1), 23–36. https://doi.org/10.1016/0168-3659(87)90034-4.

(69) Hsieh, D. S.; Rhine, W. D.; Langer, R. Zero-Order Controlled-Release Polymer Matrices for Micro- and Macromolecules. *J. Pharm. Sci.* **1983**, *72* (1), 17–22. https://doi.org/10.1002/jps.2600720105.

(70) Vidin, E.; Garbin, O.; Rodriguez, B.; Favre, R.; Bettahar-Lebugle, K. Removal of Etonogestrel Contraceptive Implants in the Operating Theater: Report on 28 Cases. *Contraception* **2007**, *76* (1), 35–39. https://doi.org/10.1016/j.contraception.2007.03.012.

(71) Mascarenhas, L. Insertion and Removal of Implanon®. *Contraception* **1998**, *58* (6), 79S-83S. https://doi.org/10.1016/S0010-7824(98)00121-8.

(72) Reuter, S.; Smith, a. Implanon: User Views in the First Year across Three Family

114

Planning Services in the Trent Region, UK. *Eur. J. Contracept. Reprod. Health Care* **2003**, *8* (December 2016), 27–36. https://doi.org/10.1080/713604396.

(73) Benagiano, G.; Gabelnick, H.; Farris, M. Contraceptive Devices: Subcutaneous Delivery Systems. *Expert Rev. Med. Devices* **2008**, *5* (5), 623–637. https://doi.org/10.1586/17434440.5.5.623.

(74) Holt, J.; Brimer, A.; Fetherston, S.; Boyd, P.; Devlin, B.; Malcolm, K. Matrix Vaginal Ring Formulations That Maintain Target In Vitro Release Rates of Dapivirine and Levonorgestrel (Alone or in Combination) over 90 Days. *AIDS Res. Hum. Retroviruses* **2014**, *30* (S1), A138–A139. https://doi.org/10.1089/aid.2014.5276.abstract.

(75) Schlesinger, E.; Ciaccio, N.; Desai, T. A. Polycaprolactone Thin-Film Drug Delivery Systems: Empirical and Predictive Models for Device Design. *Mater. Sci. Eng. C* **2015**, *57*, 232–239. https://doi.org/10.1016/j.msec.2015.07.027.

(76) Ratner, B. D. The Biocompatibility Manifesto: Biocompatibility for the Twenty-First Century. *J. Cardiovasc. Transl. Res.* **2011**, *4* (5), 523–527. https://doi.org/10.1007/s12265-011-9287-x.

(77) Burada, P. S.; Hänggi, P.; Marchesoni, F.; Schmid, G.; Talkner, P. Diffusion in Confined Geometries. *ChemPhysChem* **2009**, *10* (1), 45–54. https://doi.org/10.1002/cphc.200800526.

(78) Bernards, D. A.; Lance, K. D.; Ciaccio, N. A.; Desai, T. A. Nanostructured Thin Film Polymer Devices for Constant-Rate Protein Delivery. *Nano Lett.* **2012**, *12* (10), 5355–5361. https://doi.org/10.1021/nl302747y.

(79)   Ferrati, S.; Fine, D.; You, J.; De Rosa, E.; Hudson, L.; Zabre, E.; Hosali, S.; Zhang, L.; Hickman, C.; Sunder Bansal, S.; Cordero-Reyes, A. M.; Geninatti, T.; Sih, J.; Goodall, R.; Palapattu, G.; Kloc, M.; Ghobrial, R. M.; Ferrari, M.; Grattoni, A. Leveraging Nanochannels for Universal, Zero-Order Drug Delivery in Vivo. *J. Control. Release* **2013**, *172* (3), 1011–1019. https://doi.org/10.1016/j.jconrel.2013.09.028.

(80)   Ray, A. S.; Fordyce, M. W.; Hitchcock, M. J. M. Tenofovir Alafenamide: A Novel Prodrug of Tenofovir for the Treatment of Human Immunodeficiency Virus. *Antiviral Res.* **2016**, *125*, 63–70. https://doi.org/10.1016/j.antiviral.2015.11.009.

(81)   Margot, N. A.; Liu, Y.; Miller, M. D.; Callebaut, C. High Resistance Barrier to Tenofovir Alafenamide Is Driven by Higher Loading of Tenofovir Diphosphate into Target Cells Compared to Tenofovir Disoproxil Fumarate. *Antiviral Res.* **2016**. https://doi.org/10.1016/j.antiviral.2016.05.012.

(82)   Lee, W. A.; He, G. X.; Eisenberg, E.; Cihlar, T.; Swaminathan, S.; Mulato, A.; Cundy, K. C. Selective Intracellular Activation of a Novel Prodrug of the Human Immunodeficiency Virus Reverse Transcriptase Inhibitor Tenofovir Leads to Preferential Distribution and Accumulation in Lymphatic Tissue. *Antimicrob. Agents Chemother.* **2005**, *49* (5), 1898–1906. https://doi.org/10.1128/AAC.49.5.1898-1906.2005.

(83)   Zhang, W.; Parniak, M. A.; Sarafianos, S. G.; Cost, M. R.; Rohan, L. C. Development of a Vaginal Delivery Film Containing EFdA, a Novel Anti-HIV Nucleoside Reverse Transcriptase Inhibitor. *Int. J. Pharm.* **2014**, *461* (1–2), 203–213. https://doi.org/10.1016/j.ijpharm.2013.11.056.

(84)   Michailidis, E.; Ryan, E.; Hachiya, A.; Kirby, K.; Marchand, B.; Leslie, M.; Huber, A.;

Ong, Y.; Jackson, J.; Singh, K.; Kodama, E.; Mitsuya, H.; Parniak, M.; Sarafianos, S. Hypersusceptibility Mechanism of Tenofovir-Resistant HIV to EFdA. *Retrovirology* **2013**, *10* (1), 65. https://doi.org/10.1186/1742-4690-10-65.

(85)   Langer, R. Implantable Controlled Release Systems. *Pharmacol. Ther.* **1983**, *21* (1), 35–51. https://doi.org/10.1016/0163-7258(83)90066-9.

(86)   Cherng, J. Y.; Hou, T. Y.; Shih, M. F.; Talsma, H.; Hennink, W. E. Polyurethane-Based Drug Delivery Systems. *Int. J. Pharm.* **2013**, *450* (1–2), 145–162. https://doi.org/10.1016/j.ijpharm.2013.04.063.

(87)   Bolto, B.; Tran, T.; Hoang, M.; Xie, Z. Crosslinked Poly(Vinyl Alcohol) Membranes. *Prog. Polym. Sci.* **2009**, *34* (9), 969–981. https://doi.org/10.1016/j.progpolymsci.2009.05.003.

(88)   Moulay, S. Review: Poly(Vinyl Alcohol) Functionalizations and Applications. *Polym. Plast. Technol. Eng.* **2015**, *54* (12), 1289–1319. https://doi.org/10.1080/03602559.2015.1021487.

(89)   Hsu, T. T.; Langer, R. Polymers for the Controlled Release of Macromolecules: Effect of Molecular Weight of Ethylene-Vinyl Acetate Copolymer. *J. Biomed. Mater. Res.* **1985**, *19* (4), 445–460. https://doi.org/10.1002/jbm.820190409.

(90)   Robb, W. L. Thin Silicon Membranes. Their Permeation Properties and Some Applications. *Ann. N. Y. Acad. Sci.* **1968**, *146*, 119–137. https://doi.org/10.1111/j.1749-6632.1968.tb20277.x.

(91)   Malcolm, K.; Woolfson, D.; Russell, J.; Tallon, P.; McAuley, L.; Craig, D. Influence of

Silicone Elastomer Solubility and Diffusivity on the in Vitro Release of Drugs from Intravaginal Rings. *J. Control. Release* **2003**, *90* (2), 217–225. https://doi.org/10.1016/S0168-3659(03)00178-0.

(92)   Petrova, N. V.; Evtushenko, A. M.; Chikhacheva, I. P.; Zubov, V. P.; Kubrakova, I. V. Effect of Microwave Irradiation on the Cross-Linking of Polyvinyl Alcohol. *Russ. J. Appl. Chem.* **2005**, *78* (7), 1158–1161. https://doi.org/10.1007/s11167-005-0470-1.

(93)   Byron, P. R.; Dalby, R. N. Effects of Heat Treatment on the Permeability of Polyvinyl Alcohol Films to a Hydrophilic Solute. *J. Pharm. Sci.* **1987**, *76* (1), 65–67. https://doi.org/10.1002/jps.2600760118.

(94)   Sun, H.; Mei, L.; Song, C.; Cui, X.; Wang, P. The in Vivo Degradation, Absorption and Excretion of PCL-Based Implant. *Biomaterials* **2006**, *27* (9), 1735–1740. https://doi.org/10.1016/j.biomaterials.2005.09.019.

(95)   Silva-Cunha, A.; Fialho, S. L.; Naud, M. C.; Behar-Cohen, F. Poly-ε-Caprolactone Intravitreous Devices: An in Vivo Study. *Investig. Ophthalmol. Vis. Sci.* **2009**, *50* (5), 2312–2318. https://doi.org/10.1167/iovs.08-2969.

(96)   Ali, S. A. M.; Zhong, S.-P.; Doherty, P. J.; Williams, D. F. Mechanisms of Polymer Degradation in Implantable Devices I. Poly(Caprolactone). *Biomaterials* **1993**, *14* (9), 648–656. https://doi.org/10.1016/0142-9612(93)90063-8.

(97)   Garza-Flores, J.; Hall, P. E.; Perez-Palacios, G. Long-Acting Hormonal Contraceptives for Women. *J. Steroid Biochem. Mol. Biol.* **1991**, *40* (4–6), 697–704. https://doi.org/10.1016/0960-0760(91)90293-E.

(98) Ma, G.; Song, C.; Sun, H.; Yang, J.; Leng, X. A Biodegradable Levonorgestrel-Releasing Implant Made of PCL/F68 Compound as Tested in Rats and Dogs. *Contraception* **2006**, *74* (2), 141–147. https://doi.org/10.1016/j.contraception.2006.02.013.

(99) Gunawardana, M.; Remedios-Chan, M.; Miller, C. S.; Fanter, R.; Yang, F.; Marzinke, M. A.; Hendrix, C. W.; Beliveau, M.; Moss, J. A.; Smith, T. J.; Baum, M. M. Pharmacokinetics of Long-Acting Tenofovir Alafenamide (GS-7340) Subdermal Implant for HIV Prophylaxis. *Antimicrob. Agents Chemother.* **2015**, *59* (7), 3913–3919. https://doi.org/10.1128/AAC.00656-15.

(100) Schlesinger, E.; Johengen, D.; Luecke, E.; Rothrock, G.; McGowan, I.; van der Straten, A.; Desai, T. A Tunable, Biodegradable, Thin-Film Polymer Device as a Long-Acting Implant Delivering Tenofovir Alafenamide Fumarate for HIV Pre-Exposure Prophylaxis. *Pharm. Res.* **2016**, *33* (7), 1649–1656. https://doi.org/10.1007/s11095-016-1904-6.

(101) Jullien, V.; Tréluyer, J.-M.; Pons, G.; Rey, E. Determination of Tenofovir in Human Plasma by High-Performance Liquid Chromatography with Spectrofluorimetric Detection. *J. Chromatogr. B* **2003**, *785* (2), 377–381. https://doi.org/10.1016/S1570-0232(02)00933-9.

(102) Birkus, G.; Wang, R.; Liu, X.; Kutty, N.; MacArthur, H.; Cihlar, T.; Gibbs, C.; Swaminathan, S.; Lee, W.; McDermott, M. Cathepsin a Is the Major Hydrolase Catalyzing the Intracellular Hydrolysis of the Antiretroviral Nucleotide Phosphonoamidate Prodrugs GS-7340 and GS-9131. *Antimicrob. Agents Chemother.* **2007**, *51* (2), 543–550. https://doi.org/10.1128/AAC.00968-06.

(103) Matheson, L. E.; Hunke, W. A. Mass Transport Properties of Co(Polyether)Polyurethane

Membranes I: Preparation and Characterization. *J. Pharm. Sci.* **1981**, *70* (5), 571–573. https://doi.org/10.1002/jps.2600700528.

(104) Guan, J.; Sacks, M. S.; Beckman, E. J.; Wagner, W. R. Biodegradable Poly(Ether Ester Urethane)Urea Elastomers Based on Poly(Ether Ester) Triblock Copolymers and Putrescine: Synthesis, Characterization and Cytocompatibility. *Biomaterials* **2004**, *25* (1), 85–96. https://doi.org/10.1016/S0142-9612(03)00476-9.

(105) Shore, N. Introducing Vantas: The First Once-Yearly Luteinising Hormone-Releasing Hormone Agonist. *Eur. Urol. Suppl.* **2010**, *9* (8), 701–705. https://doi.org/10.1016/j.eursup.2010.08.004.

(106) Schlegel, P. N. Efficacy and Safety of Histrelin Subdermal Implant in Patients with Advanced Prostate Cancer. *J. Urol.* **2006**, *175* (4), 1353–1358. https://doi.org/10.1016/S0022-5347(05)00649-X.

(107) Schlegel, P. A Review of the Pharmacokinetic and Pharmacological Properties of a Once-Yearly Administered Histrelin Acetate Implant in the Treatment of Prostate Cancer. *BJU Int.* **2009**, *103*, 7–13. https://doi.org/10.1111/j.1464-410X.2009.08383.x.

(108) Croxatto, H. B. Progestin Implants. *Steroids* **2000**, *65* (10–11), 681–685. https://doi.org/10.1016/S0039-128X(00)00124-0.

(109) Ferrati, S.; Nicolov, E.; Bansal, S.; Zabre, E.; Geninatti, T.; Ziemys, A.; Hudson, L.; Ferrari, M.; Goodall, R.; Khera, M.; Palapattu, G.; Grattoni, A. Delivering Enhanced Testosterone Replacement Therapy through Nanochannels. *Adv. Healthc. Mater.* **2015**, *4* (3), 446–451. https://doi.org/10.1002/adhm.201400348.

(110) Nicolov, E.; Ferrati, S.; Goodall, R.; Hudson, L.; Hosali, S.; Crowley, M.; Palapattu, G.; Khera, M.; Grattoni, A. Mp43-20 Nanotechnology-Based Implant for Long Term Testosterone Replacement. *J. Urol.* **2014**, *191* (4), e485–e486. https://doi.org/10.1016/j.juro.2014.02.1177.

(111) Henry, R. R.; Rosenstock, J.; Logan, D.; Alessi, T.; Luskey, K.; Baron, M. A. Continuous Subcutaneous Delivery of Exenatide via ITCA 650 Leads to Sustained Glycemic Control and Weight Loss for 48 Weeks in Metformin-Treated Subjects with Type 2 Diabetes. *J. Diabetes Complications* **2014**, *28* (3), 393–398. https://doi.org/10.1016/j.jdiacomp.2013.12.009.

(112) Rohloff, C. M.; Alessi, T. R.; Yang, B.; Dahms, J.; Carr, J. P.; Lautenbach, S. D. DUROS Technology Delivers Peptides and Proteins at Consistent Rate Continuously for 3 to 12 Months. *J. diabetes Sci. Technol.* **2008**, *2* (3), 461–467. https://doi.org/10.1177/193229680800200316.

(113) Blakney, A. K.; Krogstad, E. A.; Jiang, Y. H.; Woodrow, K. A. Delivery of Multipurpose Prevention Drug Combinations from Electrospun Nanofibers Using Composite Microarchitectures. *Int. J. Nanomedicine* **2014**, *9* (1), 2967–2978. https://doi.org/10.2147/IJN.S61664.

(114) Blakney, A. K.; Ball, C.; Krogstad, E. a; Woodrow, K. a. Electrospun Fibers for Vaginal Anti-HIV Drug Delivery. *Antiviral Res.* **2013**, *100 Suppl*, S9-16. https://doi.org/10.1016/j.antiviral.2013.09.022.

(115) Teller, R. S.; Rastogi, R.; Johnson, T. J.; Blair, M. J.; Hitchcock, R. W.; Kiser, P. F. Intravaginal Flux Controlled Pump for Sustained Release of Macromolecules. *Pharm.*

Res. **2014**, 2344–2353. https://doi.org/10.1007/s11095-014-1331-5.

(116) Rastogi, R.; Teller, R. S.; Mesquita, P. M. M.; Herold, B. C.; Kiser, P. F. Osmotic Pump Tablets for Delivery of Antiretrovirals to the Vaginal Mucosa. *Antiviral Res.* **2013**, *100* (1), 255–258. https://doi.org/10.1016/j.antiviral.2013.08.007.

(117) Boyd, P.; Fetherston, S. M.; Mccoy, C. F.; Major, I.; Murphy, D. J.; Kumar, S.; Holt, J.; Brimer, A.; Blanda, W.; Devlin, B.; Malcolm, R. K. Matrix and Reservoir-Type Multipurpose Vaginal Rings for Controlled Release of Dapivirine and Levonorgestrel. *Int. J. Pharm.* **2016**, *511* (1), 619–629. https://doi.org/10.1016/j.ijpharm.2016.07.051.

(118) Bayer, L. L.; Jensen, J. T. ACIDFORM: A Review of the Evidence. *Contraception* **2014**, *90* (1), 11–18. https://doi.org/10.1016/j.contraception.2014.01.015.

(119) Garg, S.; Anderson, R. A.; Chany, C. J.; Waller, D. P.; Xia Hui Diao; Vermani, K.; Zaneveld, L. J. D. Properties of a New Acid-Buffering Bioadhesive Vaginal Formulation (ACIDFORM). *Contraception* **2001**, *64* (1), 67–75. https://doi.org/10.1016/S0010-7824(01)00217-7.

(120) Friend, D. R.; Clark, J. T.; Kiser, P. F.; Clark, M. R. Multipurpose Prevention Technologies: Products in Development. *Antiviral Res.* **2013**, *100* (SUPPL.), S39–S47. https://doi.org/10.1016/j.antiviral.2013.09.030.

(121) Su, J. T.; Teller, R. S.; Srinivasan, P.; Zhang, J.; Martin, A.; Sung, S.; Smith, J. M.; Kiser, P. F. A Dose Ranging Pharmacokinetic Evaluation of IQP-0528 Released from Intravaginal Rings in Non-Human Primates. *Pharm. Res.* **2017**, *34* (10), 2163–2171. https://doi.org/10.1007/s11095-017-2224-1.

(122) Blaschke, T. F.; Osterberg, L.; Vrijens, B.; Urquhart, J. Adherence to Medications: Insights Arising from Studies on the Unreliable Link between Prescribed and Actual Drug Dosing Histories. *Annu Rev Pharmacol Toxicol* **2012**, *52*, 275–301. https://doi.org/10.1146/annurev-pharmtox-011711-113247.

(123) van der Straten, A.; Montgomery, E. T.; Hartmann, M.; Minnis, A. Methodological Lessons from Clinical Trials and the Future of Microbicide Research. *Curr. HIV/AIDS Rep.* **2012**, *10* (1), 89–102. https://doi.org/10.1007/s11904-012-0141-9.

(124) Jacobstein, R. Long-Acting and Permanent Contraception: An International Development, Service Delivery Perspective. *J. Midwifery Women's Heal.* **2007**, *52* (4), 361–367. https://doi.org/10.1016/j.jmwh.2007.01.001.

(125) Woodruff, M. A.; Hutmacher, D. W. The Return of a Forgotten Polymer - Polycaprolactone in the 21st Century. *Prog. Polym. Sci.* **2010**, *35* (10), 1217–1256. https://doi.org/10.1016/j.progpolymsci.2010.04.002.

(126) Hu, J. Z.; Zhou, Y. C.; Huang, L. H.; Lu, H. Bin. Development of Biodegradable Polycaprolactone Film as an Internal Fixation Material to Enhance Tendon Repair: An in Vitro Study. *BMC Musculoskelet. Disord.* **2013**, *14*. https://doi.org/10.1186/1471-2474-14-246.

(127) Mei, L.; Bao, J.; Tang, L.; Zhang, C.; Wang, H.; Sun, L.; Ma, G.; Huang, L.; Yang, J.; Zhang, L.; Liu, K.; Song, C.; Sun, H. A Novel Mifepristone-Loaded Implant for Long-Term Treatment of Endometriosis: In Vitro and in Vivo Studies. *Eur. J. Pharm. Sci.* **2010**, *39* (5), 421–427. https://doi.org/10.1016/j.ejps.2010.01.012.

(128) Williams, J. M.; Adewunmi, A.; Schek, R. M.; Flanagan, C. L.; Krebsbach, P. H.;

Feinberg, S. E.; Hollister, S. J.; Das, S. Bone Tissue Engineering Using Polycaprolactone Scaffolds Fabricated via Selective Laser Sintering. *Biomaterials* **2005**, *26* (23), 4817–4827. https://doi.org/10.1016/j.biomaterials.2004.11.057.

(129) Schlesinger, E. B.; Bernards, D. A.; Chen, H. H.; Feindt, J.; Cao, J.; Dix, D.; Romano, C.; Bhisitkul, R. B.; Desai, T. A. Device Design Methodology and Formulation of a Protein Therapeutic for Sustained Release Intraocular Delivery. *Bioeng. Transl. Med.* **2019**, *4* (1), 152–163. https://doi.org/10.1002/btm2.10121.

(130) Lance, K. D.; Good, S. D.; Mendes, T. S.; Ishikiriyama, M.; Chew, P.; Estes, L. S.; Yamada, K.; Mudumba, S.; Bhisitkul, R. B.; Desai, T. A. In Vitro and in Vivo Sustained Zero-Order Delivery of Rapamycin (Sirolimus) from a Biodegradable Intraocular Device. *Investig. Ophthalmol. Vis. Sci.* **2015**, *56* (12), 7331–7337. https://doi.org/10.1167/iovs.15-17757.

(131) Yen, C.; He, H.; Lee, L. J.; Ho, W. S. W. Synthesis and Characterization of Nanoporous Polycaprolactone Membranes via Thermally- and Nonsolvent-Induced Phase Separations for Biomedical Device Application. *J. Memb. Sci.* **2009**, *343* (1–2), 180–188. https://doi.org/10.1016/j.memsci.2009.07.024.

(132) Pitt, C. G.; Chasalow, F. I.; Hibionada, Y. M.; Klimas, D. M.; Park, T.; Carolina, N. Aliphatic Polyesters . I . The Degradation of Poly (e- Caprolactone) In Vivo. *J. Appl. Polym. Sci.* **1981**, *26* (11), 3779–3787. https://doi.org/10.1002/app.1981.070261124.

(133) Lam, C. X. F.; Savalani, M. M.; Teoh, S. H.; Hutmacher, D. W. Dynamics of in Vitro Polymer Degradation of Polycaprolactone-Based Scaffolds: Accelerated versus Simulated Physiological Conditions. *Biomed. Mater.* **2008**, *3* (3), 34108.

https://doi.org/10.1088/1748-6041/3/3/034108.

(134) Pan, J.; Chen, X. Modelling Degradation of Amorphous Biodegradable Polyesters: Basic Model. In *Modelling Degradation of Bioresorbable Polymeric Medical Devices*; Elsevier, 2015; pp 15–31. https://doi.org/10.1533/9781782420255.1.15.

(135) Gleadall, A.; Pan, J.; Kruft, M. A.; Kellomäki, M. Degradation Mechanisms of Bioresorbable Polyesters. Part 1. Effects of Random Scission, End Scission and Autocatalysis. *Acta Biomater.* **2014**, *10* (5), 2223–2232. https://doi.org/10.1016/j.actbio.2013.12.039.

(136) Gleadall, A.; Pan, J.; Kruft, M. A.; Kellomäki, M. Degradation Mechanisms of Bioresorbable Polyesters. Part 2. Effects of Initial Molecular Weight and Residual Monomer. *Acta Biomater.* **2014**, *10* (5), 2233–2240. https://doi.org/10.1016/j.actbio.2014.01.017.

(137) Shih, C. Chain-End Scission in Acid Catalyzed Hydrolysis of Poly (d,l-Lactide) in Solution. *J. Control. Release* **1995**, *34* (1), 9–15. https://doi.org/10.1016/0168-3659(94)00100-9.

(138) Cha, Y.; Pitt, C. G. The Biodegradability of Polyester Blends. *Biomaterials* **1990**, *11* (2), 108–112. https://doi.org/10.1016/0142-9612(90)90124-9.

(139) Gan, Z.; Yu, D.; Zhong, Z.; Liang, Q.; Jing, X. Enzymatic Degradation of Poly(ε-Caprolactone)/Poly(Dl-Lactide) Blends in Phosphate Buffer Solution. *Polymer (Guildf).* **1999**, *40* (10), 2859–2862. https://doi.org/10.1016/S0032-3861(98)00549-7.

(140) Wang, L.; Ma, W.; Gross, R. A.; McCarthy, S. P. Reactive Compatibilization of

Biodegradable Blends of Poly(Lactic Acid) and Poly(ε-Caprolactone). *Polym. Degrad. Stab.* **1998**, *59* (1–3), 161–168. https://doi.org/10.1016/S0141-3910(97)00196-1.

(141) Pitt, G. G.; Gratzl, M.; Kimmel, G.; Surles, J.; Sohindler, A. Aliphatic Polyesters II. The Degradation of Poly (DL-Lactide), Poly (ε-Caprolactone), and Their Copolymers in Vivo. *Biomaterials* **1981**, *2* (4), 215–220. https://doi.org/10.1016/0142-9612(81)90060-0.

(142) Wei, X. W.; Gong, C. Y.; Gou, M. L.; Fu, S. Z.; Guo, Q. F.; Shi, S.; Luo, F.; Guo, G.; Qiu, L. Y.; Qian, Z. Y. Biodegradable Poly(ε-Caprolactone)-Poly(Ethylene Glycol) Copolymers as Drug Delivery System. *Int. J. Pharm.* **2009**, *381* (1), 1–18. https://doi.org/10.1016/j.ijpharm.2009.07.033.

(143) Bodmeier, R.; Oh, K. H.; Chen, H. The Effect of the Addition of Low Molecular Weight Poly(Dl-Lactide) on Drug Release from Biodegradable Poly(Dl-Lactide) Drug Delivery Systems. *Int. J. Pharm.* **1989**, *51* (1), 1–8. https://doi.org/10.1016/0378-5173(89)90068-9.

(144) Cutright, D. E.; Hunsuck, E. E. Tissue Reaction to the Biodegradable Polylactic Acid Suture. *Oral Surgery, Oral Med. Oral Pathol.* **1971**, *31* (1), 134–139. https://doi.org/10.1016/0030-4220(71)90044-2.

(145) Daugherty, A. L.; Cleland, J. L.; Duenas, E. M.; Mrsny, R. J. Pharmacological Modulation of the Tissue Response to Implanted Polylactic-Co-Glycolic Acid Microspheres. *Eur. J. Pharm. Biopharm.* **1997**, *44* (1), 89–102. https://doi.org/10.1016/S0939-6411(97)00065-9.

(146) Haward, R. N.; Wright, B.; Williamson, G. R.; Thackray, G. Effect of Blending on the Molecular Weight Distribution of Polymers. *J. Polym. Sci. Part A Gen. Pap.* **1964**, *2* (7), 2977–3007. https://doi.org/10.1002/pol.1964.100020701.

(147) Schindler, a; Hibionada, Y. M.; Pitt, C. G. Aliphatic Polyesters. III. Molecular Weight and Molecular Weight Distribution in Alcohol-Initiated Polymerizations of Epsilon-Caprolactone. *J. Polym. Sci. Polym. Chem. Ed.* **1982**, *20*, 319–326. https://doi.org/10.1002/pol.1982.170200206.

(148) Johnson, L. M.; Krovi, S. A.; Li, L.; Girouard, N.; Demkovich, Z. R.; Myers, D.; Creelman, B.; van der Straten, A. Characterization of a Reservoir-Style Implant for Sustained Release of Tenofovir Alafenamide (TAF) for HIV Pre-Exposure Prophylaxis (PrEP). *Pharmaceutics* **2019**, *11* (7), 315. https://doi.org/10.3390/pharmaceutics11070315.

(149) Lam, C. X.; Teoh, S. H.; Hutmacher, D. W. Comparison of the Degradation of Polycaprolactone and Polycaprolactone–(β-Tricalcium Phosphate) Scaffolds in Alkaline Medium. *Polym. Int.* **2007**, *56* (6), 718–728. https://doi.org/10.1002/pi.2195.

(150) Eshraghi, S.; Das, S. Mechanical and Microstructural Properties of Polycaprolactone Scaffolds with One-Dimensional, Two-Dimensional, and Three-Dimensional Orthogonally Oriented Porous Architectures Produced by Selective Laser Sintering. *Acta Biomater.* **2010**, *6* (7), 2467–2476. https://doi.org/10.1016/j.actbio.2010.02.002.

(151) Sastry, S.; Nyshadham, J.; Fix, J. Recent Technological Advances in Oral Drug Delivery - a Review. *Pharm. Sci. Technolo. Today* **2000**, *3* (4), 138–145. https://doi.org/10.1016/S1461-5347(00)00247-9.

(152) Morishita, M.; Peppas, N. A. Is the Oral Route Possible for Peptide and Protein Drug Delivery? *Drug Discov. Today* **2006**, *11* (19–20), 905–910. https://doi.org/10.1016/j.drudis.2006.08.005.

(153) Renukuntla, J.; Vadlapudi, A. D.; Patel, A.; Boddu, S. H. S.; Mitra, A. K. Approaches for Enhancing Oral Bioavailability of Peptides and Proteins. *Int. J. Pharm.* **2013**, *447* (1–2), 75–93. https://doi.org/10.1016/j.ijpharm.2013.02.030.

(154) Thwala, L. N.; Préat, V.; Csaba, N. S. Emerging Delivery Platforms for Mucosal Administration of Biopharmaceuticals: A Critical Update on Nasal, Pulmonary and Oral Routes. *Expert Opin. Drug Deliv.* **2017**, *14* (1), 23–36. https://doi.org/10.1080/17425247.2016.1206074.

(155) Fox, C. B.; Kim, J.; Le, L. V.; Nemeth, C. L.; Chirra, H. D.; Desai, T. A. Micro/Nanofabricated Platforms for Oral Drug Delivery. *J. Control. Release* **2015**, *219*, 431–444. https://doi.org/10.1016/j.jconrel.2015.07.033.

(156) Nielsen, L. H.; Keller, S. S.; Boisen, A. Microfabricated Devices for Oral Drug Delivery. *Lab Chip* **2018**, *18* (16), 2348–2358. https://doi.org/10.1039/C8LC00408K.

(157) Voldman, J.; Gray, M. L.; Schmidt, M. A. Microfabrication in Biology and Medicine. *Annu. Rev. Biomed. Eng.* **1999**, *1* (1), 401–425. https://doi.org/10.1146/annurev.bioeng.1.1.401.

(158) Huh, D.; Kim, H. J.; Fraser, J. P.; Shea, D. E.; Khan, M.; Bahinski, A.; Hamilton, G. A.; Ingber, D. E. Microfabrication of Human Organs-on-Chips. *Nat. Protoc.* **2013**, *8* (11), 2135–2157. https://doi.org/10.1038/nprot.2013.137.

(159) Sant, S.; Tao, S. L.; Fisher, O. Z.; Xu, Q.; Peppas, N. A.; Khademhosseini, A. Microfabrication Technologies for Oral Drug Delivery. *Adv. Drug Deliv. Rev.* **2012**, *64* (6), 496–507. https://doi.org/10.1016/j.addr.2011.11.013.

(160) Fox, C.; Chirra, H.; Desai, T. Planar Bioadhesive Microdevices: A New Technology for Oral Drug Delivery. *Curr. Pharm. Biotechnol.* **2014**, *15* (7), 673–683. https://doi.org/10.2174/1389201015666140915152706.

(161) Marizza, P.; Keller, S. S.; Müllertz, A.; Boisen, A. Polymer-Filled Microcontainers for Oral Delivery Loaded Using Supercritical Impregnation. *J. Control. Release* **2014**, *173* (1), 1–9. https://doi.org/10.1016/j.jconrel.2013.09.022.

(162) Nielsen, L. H.; Melero, A.; Keller, S. S.; Jacobsen, J.; Garrigues, T.; Rades, T.; Müllertz, A.; Boisen, A. Polymeric Microcontainers Improve Oral Bioavailability of Furosemide. *Int. J. Pharm.* **2016**, *504* (1–2), 98–109. https://doi.org/10.1016/j.ijpharm.2016.03.050.

(163) Koch, B.; Rubino, I.; Quan, F.-S.; Yoo, B.; Choi, H.-J. Microfabrication for Drug Delivery. *Materials (Basel).* **2016**, *9* (8), 646. https://doi.org/10.3390/ma9080646.

(164) Norman, J.; Madurawe, R. D.; Moore, C. M. V.; Khan, M. A.; Khairuzzaman, A. A New Chapter in Pharmaceutical Manufacturing: 3D-Printed Drug Products. *Adv. Drug Deliv. Rev.* **2017**, *108*, 39–50. https://doi.org/10.1016/j.addr.2016.03.001.

(165) Narkevich, I. A.; Flisyuk, E. V.; Terent'eva, O. A.; Semin, A. A. Additive Manufacturing Technologies for Pharmaceutics. *Pharm. Chem. J.* **2018**, *51* (11), 1025–1029. https://doi.org/10.1007/s11094-018-1733-5.

(166) Lim, S. H.; Kathuria, H.; Tan, J. J. Y.; Kang, L. 3D Printed Drug Delivery and Testing Systems — a Passing Fad or the Future? *Adv. Drug Deliv. Rev.* **2018**. https://doi.org/10.1016/j.addr.2018.05.006.

(167) McHugh, K. J.; Nguyen, T. D.; Linehan, A. R.; Yang, D.; Behrens, A. M.; Rose, S.;

Tochka, Z. L.; Tzeng, S. Y.; Norman, J. J.; Anselmo, A. C.; Xu, X.; Tomasic, S.; Taylor, M. A.; Lu, J.; Guarecuco, R.; Langer, R.; Jaklenec, A. Fabrication of Fillable Microparticles and Other Complex 3D Microstructures. *Science (80-.).* **2017**, *357* (6356), 1138–1142. https://doi.org/10.1126/science.aaf7447.

(168) Sadia, M.; Arafat, B.; Ahmed, W.; Forbes, R. T.; Alhnan, M. A. Channelled Tablets: An Innovative Approach to Accelerating Drug Release from 3D Printed Tablets. *J. Control. Release* **2018**, *269* (November 2017), 355–363. https://doi.org/10.1016/j.jconrel.2017.11.022.

(169) Solanki, N. G.; Tahsin, M.; Shah, A. V.; Serajuddin, A. T. M. Formulation of 3D Printed Tablet for Rapid Drug Release by Fused Deposition Modeling: Screening Polymers for Drug Release, Drug-Polymer Miscibility and Printability. *J. Pharm. Sci.* **2018**, *107* (1), 390–401. https://doi.org/10.1016/j.xphs.2017.10.021.

(170) Tappa, K.; Jammalamadaka, U.; Ballard, D. H.; Bruno, T.; Israel, M. R.; Vemula, H.; Meacham, J. M.; Mills, D. K.; Woodard, P. K.; Weisman, J. A. Medication Eluting Devices for the Field of OBGYN (MEDOBGYN): 3D Printed Biodegradable Hormone Eluting Constructs, a Proof of Concept Study. *PLoS One* **2017**, *12* (8), 1–17. https://doi.org/10.1371/journal.pone.0182929.

(171) Maniruzzaman, M.; Boateng, J. S.; Snowden, M. J.; Douroumis, D. A Review of Hot-Melt Extrusion: Process Technology to Pharmaceutical Products. *ISRN Pharm.* **2012**, *2012*, 1–9. https://doi.org/10.5402/2012/436763.

(172) Thakral, S.; Thakral, N. K.; Majumdar, D. K. Eudragit®: A Technology Evaluation. *Expert Opin. Drug Deliv.* **2013**, *10* (1), 131–149.

https://doi.org/10.1517/17425247.2013.736962.

(173) Nollenberger, K.; Albers, J. Poly(Meth)Acrylate-Based Coatings. *Int. J. Pharm.* **2013**, *457* (2), 461–469. https://doi.org/10.1016/j.ijpharm.2013.09.029.

(174) Kyobula, M.; Adedeji, A.; Alexander, M. R.; Saleh, E.; Wildman, R.; Ashcroft, I.; Gellert, P. R.; Roberts, C. J. 3D Inkjet Printing of Tablets Exploiting Bespoke Complex Geometries for Controlled and Tuneable Drug Release. *J. Control. Release* **2017**, *261* (March), 207–215. https://doi.org/10.1016/j.jconrel.2017.06.025.

(175) Sealfon, S. C.; Chu, T. T. RNA and DNA Microarrays. In *Biological Microarrays. Methods in Molecular Biology*; 2011; pp 3–34. https://doi.org/10.1007/978-1-59745-551-0_1.

(176) Goldmann, T.; Gonzalez, J. S. DNA-Printing: Utilization of a Standard Inkjet Printer for the Transfer of Nucleic Acids to Solid Supports. *J. Biochem. Biophys. Methods* **2000**, *42* (3), 105–110. https://doi.org/10.1016/S0165-022X(99)00049-4.

(177) Daly, R.; Harrington, T. S.; Martin, G. D.; Hutchings, I. M. Inkjet Printing for Pharmaceutics - A Review of Research and Manufacturing. *Int. J. Pharm.* **2015**, *494* (2), 554–567. https://doi.org/10.1016/j.ijpharm.2015.03.017.

(178) Sumerel, J.; Lewis, J.; Doraiswamy, A.; Deravi, L. F.; Sewell, S. L.; Gerdon, A. E.; Wright, D. W.; Narayan, R. J. Piezoelectric Ink Jet Processing of Materials for Medical and Biological Applications. *Biotechnol. J.* **2006**, *1* (9), 976–987. https://doi.org/10.1002/biot.200600123.

(179) Fox, C. B.; Nemeth, C. L.; Chevalier, R. W.; Cantlon, J.; Bogdanoff, D. B.; Hsiao, J. C.;

Desai, T. A. Picoliter-Volume Inkjet Printing into Planar Microdevice Reservoirs for Low-Waste, High-Capacity Drug Loading. *Bioeng. Transl. Med.* **2017**, *2* (1), 9–16. https://doi.org/10.1002/btm2.10053.

(180) Abid, Z.; Gundlach, C.; Durucan, O.; von Halling Laier, C.; Nielsen, L. H.; Boisen, A.; Keller, S. S. Powder Embossing Method for Selective Loading of Polymeric Microcontainers with Drug Formulation. *Microelectron. Eng.* **2017**, *171*, 20–24. https://doi.org/10.1016/j.mee.2017.01.018.

(181) Nielsen, L. H.; Rades, T.; Boyd, B.; Boisen, A. Microcontainers as an Oral Delivery System for Spray Dried Cubosomes Containing Ovalbumin. *Eur. J. Pharm. Biopharm.* **2017**, *118*, 13–20. https://doi.org/10.1016/j.ejpb.2016.12.008.

(182) Marizza, P.; Pontoni, L.; Rindzevicius, T.; Alopaeus, J. F.; Su, K.; Zeitler, J. A.; Keller, S. S.; Kikic, I.; Moneghini, M.; De Zordi, N.; Solinas, D.; Cortesi, A.; Boisen, A. Supercritical Impregnation of Polymer Matrices Spatially Confined in Microcontainers for Oral Drug Delivery: Effect of Temperature, Pressure and Time. *J. Supercrit. Fluids* **2016**, *107*, 145–152. https://doi.org/10.1016/j.supflu.2015.08.023.

(183) Marizza, P.; Keller, S. S.; Boisen, A. Inkjet Printing as a Technique for Filling of Micro-Wells with Biocompatible Polymers. *Microelectron. Eng.* **2013**, *111*, 391–395. https://doi.org/10.1016/j.mee.2013.03.168.

(184) Mazzoni, C.; Tentor, F.; Strindberg, S. A.; Nielsen, L. H.; Keller, S. S.; Alstrøm, T. S.; Gundlach, C.; Müllertz, A.; Marizza, P.; Boisen, A. From Concept to in Vivo Testing: Microcontainers for Oral Drug Delivery. *J. Control. Release* **2017**, *268* (September), 343–351. https://doi.org/10.1016/j.jconrel.2017.10.013.

(185) Chirra, H. D.; Shao, L.; Ciaccio, N.; Fox, C. B.; Wade, J. M.; Ma, A.; Desai, T. A. Planar Microdevices for Enhanced In Vivo Retention and Oral Bioavailability of Poorly Permeable Drugs. *Adv. Healthc. Mater.* **2014**, *3* (10), 1648–1654. https://doi.org/10.1002/adhm.201300676.

(186) Kim, B. Y.; Jeong, J. H.; Park, K.; Kim, J. D. Bioadhesive Interaction and Hypoglycemic Effect of Insulin-Loaded Lectin-Microparticle Conjugates in Oral Insulin Delivery System. *J. Control. Release* **2005**, *102* (3), 525–538. https://doi.org/10.1016/j.jconrel.2004.10.032.

(187) Soltman, D.; Subramanian, V. Inkjet-Printed Line Morphologies and Temperature Control of the Coffee Ring Effect. *Langmuir* **2008**, *24* (5), 2224–2231. https://doi.org/10.1021/la7026847.

(188) Li, Y.; Yang, Q.; Li, M.; Song, Y. Rate-Dependent Interface Capture beyond the Coffee-Ring Effect. *Sci. Rep.* **2016**, *6* (1), 24628. https://doi.org/10.1038/srep24628.

(189) Sun, J.; Bao, B.; He, M.; Zhou, H.; Song, Y. Recent Advances in Controlling the Depositing Morphologies of Inkjet Droplets. *ACS Appl. Mater. Interfaces* **2015**, *7* (51), 28086–28099. https://doi.org/10.1021/acsami.5b07006.

(190) Mampallil, D.; Eral, H. B. A Review on Suppression and Utilization of the Coffee-Ring Effect. *Adv. Colloid Interface Sci.* **2018**, *252*, 38–54. https://doi.org/10.1016/j.cis.2017.12.008.

(191) Heinemann, L.; Richter, B. Clinical Pharmacology of Human Insulin. *Diabetes Care* **1993**, *16* (Supplement_3), 90–100. https://doi.org/10.2337/diacare.16.3.90.

(192) Choonara, B. F.; Choonara, Y. E.; Kumar, P.; Bijukumar, D.; du Toit, L. C.; Pillay, V. A Review of Advanced Oral Drug Delivery Technologies Facilitating the Protection and Absorption of Protein and Peptide Molecules. *Biotechnol. Adv.* **2014**, *32* (7), 1269–1282. https://doi.org/10.1016/j.biotechadv.2014.07.006.

(193) Lee, H. J. Protein Drug Oral Delivery: The Recent Progress. *Arch. Pharm. Res.* **2002**, *25* (5), 572–584. https://doi.org/10.1007/BF02976925.

(194) Abramson, A.; Halperin, F.; Kim, J.; Traverso, G. Quantifying the Value of Orally Delivered Biologic Therapies: A Cost-Effectiveness Analysis of Oral Semaglutide. *J. Pharm. Sci.* **2019**, *108* (9), 3138–3145. https://doi.org/10.1016/j.xphs.2019.04.022.

(195) Homayun, B.; Lin, X.; Choi, H. J. Challenges and Recent Progress in Oral Drug Delivery Systems for Biopharmaceuticals. *Pharmaceutics* **2019**, *11* (3). https://doi.org/10.3390/pharmaceutics11030129.

(196) Brown, T. D.; Whitehead, K. A.; Mitragotri, S. Materials for Oral Delivery of Proteins and Peptides. *Nat. Rev. Mater.* **2019**. https://doi.org/10.1038/s41578-019-0156-6.

(197) Ahadian, S.; Finbloom, J. A.; Mofidfar, M.; Diltemiz, S. E.; Nasrollahi, F.; Davoodi, E.; Hosseini, V.; Mylonaki, I.; Sangabathuni, S.; Montazerian, H.; Fetah, K.; Nasiri, R.; Dokmeci, M. R.; Stevens, M. M.; Desai, T. A.; Khademhosseini, A.; Mo, M.; Emir, S.; Nasrollahi, F.; Davoodi, E.; Hosseini, V.; Mylonaki, I.; Sangabathuni, S.; Montazerian, H.; Fetah, K.; Nasiri, R.; Remzi, M.; Stevens, M. M.; Desai, T. A.; Khademhosseini, A. Micro and Nanoscale Technologies in Oral Drug Delivery. *Adv. Drug Deliv. Rev.* **2020**. https://doi.org/10.1016/j.addr.2020.07.012.

(198) Li, J.; Thamphiwatana, S.; Liu, W.; Esteban-Fernández De Ávila, B.; Angsantikul, P.;

Sandraz, E.; Wang, J.; Xu, T.; Soto, F.; Ramez, V.; Wang, X.; Gao, W.; Zhang, L.; Wang, J. Enteric Micromotor Can Selectively Position and Spontaneously Propel in the Gastrointestinal Tract. *ACS Nano* **2016**, *10* (10), 9536–9542. https://doi.org/10.1021/acsnano.6b04795.

(199) Vaut, L.; Juszczyk, J. J.; Kamguyan, K.; Jensen, K. E.; Tosello, G.; Boisen, A. 3D Printing of Reservoir Devices for Oral Drug Delivery: From Concept to Functionality through Design Improvement for Enhanced Mucoadhesion. *ACS Biomater. Sci. Eng.* **2020**. https://doi.org/10.1021/acsbiomaterials.9b01760.

(200) Li, D.; Zhuang, J.; He, H.; Jiang, S.; Banerjee, A.; Lu, Y.; Wu, W.; Mitragotri, S.; Gan, L.; Qi, J. Influence of Particle Geometry on Gastrointestinal Transit and Absorption Following Oral Administration. *ACS Appl. Mater. Interfaces* **2017**, *9* (49), 42492–42502. https://doi.org/10.1021/acsami.7b11821.

(201) Schmidt, C.; Lautenschlaeger, C.; Collnot, E. M.; Schumann, M.; Bojarski, C.; Schulzke, J. D.; Lehr, C. M.; Stallmach, A. Nano- and Microscaled Particles for Drug Targeting to Inflamed Intestinal Mucosa - A First in Vivo Study in Human Patients. *J. Control. Release* **2013**, *165* (2), 139–145. https://doi.org/10.1016/j.jconrel.2012.10.019.

(202) Hua, S. Advances in Oral Drug Delivery for Regional Targeting in the Gastrointestinal Tract - Influence of Physiological, Pathophysiological and Pharmaceutical Factors. *Front. Pharmacol.* **2020**, *11* (April), 1–22. https://doi.org/10.3389/fphar.2020.00524.

(203) Christfort, J. F.; Guillot, A. J.; Melero, A.; Thamdrup, L. H. E.; Garrigues, T. M.; Boisen, A.; Zór, K.; Nielsen, L. H. Cubic Microcontainers Improve In Situ Colonic Mucoadhesion and Absorption of Amoxicillin in Rats. *Pharmaceutics* **2020**, *12* (4), 355.

https://doi.org/10.3390/pharmaceutics12040355.

(204) Nemeth, C. L.; Lykins, W. R.; Tran, H.; ElSayed, M. E. H.; Desai, T. A. Bottom-Up
Fabrication of Multilayer Enteric Devices for the Oral Delivery of Peptides. *Pharm. Res.*
2019, *36* (6), 89. https://doi.org/10.1007/s11095-019-2618-3.

(205) Smart, J. D.; Kellaway, I. W. Pharmaceutical Factors Influencing the Rate of
Gastrointestinal Transit in an Animal Model. *Int. J. Pharm.* **1989**, *53* (1), 79–83.
https://doi.org/10.1016/0378-5173(89)90365-7.

(206) Ma, Y.; Fuchs, A. V.; Boase, N. R. B.; Rolfe, B. E.; Coombes, A. G. A.; Thurecht, K. J.
The in Vivo Fate of Nanoparticles and Nanoparticle-Loaded Microcapsules after Oral
Administration in Mice: Evaluation of Their Potential for Colon-Specific Delivery. *Eur. J.
Pharm. Biopharm.* **2015**, *94*, 393–403. https://doi.org/10.1016/j.ejpb.2015.06.014.

(207) Shen, C.; Yang, Y.; Shen, B.; Xie, Y.; Qi, J.; Dong, X.; Zhao, W.; Zhu, W.; Wu, W.;
Yuan, H.; Lu, Y. Self-Discriminating Fluorescent Hybrid Nanocrystals: Efficient and
Accurate Tracking of Translocation via Oral Delivery. *Nanoscale* **2018**, *10* (1), 436–450.
https://doi.org/10.1039/c7nr06052a.

(208) Bhutiani, N.; Samykutty, A.; McMasters, K. M.; Egilmez, N. K.; McNally, L. R. In Vivo
Tracking of Orally-Administered Particles within the Gastrointestinal Tract of Murine
Models Using Multispectral Optoacoustic Tomography. *Photoacoustics* **2019**, *13*
(November 2018), 46–52. https://doi.org/10.1016/j.pacs.2018.11.003.

(209) Gómez-Lado, N.; Seoane-Viaño, I.; Matiz, S.; Madla, C. M.; Yadav, V.; Aguiar, P.; Basit,
A. W.; Goyanes, A. Gastrointestinal Tracking and Gastric Emptying of Coated Capsules
in Rats with or without Sedation Using CT Imaging. *Pharmaceutics* **2020**, *12* (1).

https://doi.org/10.3390/pharmaceutics12010081.

(210) Oosegi, T.; Onishi, H.; Machida, Y. Gastrointestinal Distribution and Absorption Behavior of Eudragit-Coated Chitosan-Prednisolone Conjugate Microspheres in Rats with TNBS-Induced Colitis. *Int. J. Pharm.* **2008**, *348* (1–2), 80–88. https://doi.org/10.1016/j.ijpharm.2007.07.007.

(211) Panthani, M. G.; Khan, T. A.; Reid, D. K.; Hellebusch, D. J.; Rasch, M. R.; Maynard, J. A.; Korgel, B. A. In Vivo Whole Animal Fluorescence Imaging of a Microparticle-Based Oral Vaccine Containing (CuInSexS2- x)/ZnS Core/Shell Quantum Dots. *Nano Lett.* **2013**, *13* (9), 4294–4298. https://doi.org/10.1021/nl402054w.

(212) McConnell, E. L.; Basit, A. W.; Murdan, S. Measurements of Rat and Mouse Gastrointestinal PH, Fluid and Lymphoid Tissue, and Implications for in-Vivo Experiments. *J. Pharm. Pharmacol.* **2008**, *60* (1), 63–70. https://doi.org/10.1211/jpp.60.1.0008.

(213) Vaut, L.; Jensen, K. E.; Tosello, G.; Khosla, A.; Furukawa, H.; Boisen, A. Additive Manufacturing of Microreservoir Devices for Oral Drug Delivery Using an Acculas BA-30 Micro-Stereolithography Instrument: A Feasibility Study. *J. Electrochem. Soc.* **2019**, *166* (9), B3257–B3263. https://doi.org/10.1149/2.0421909jes.

(214) Ogiolda, L.; Wanke, R.; Rottmann, O.; Hermanns, W.; Wolf, E. Intestinal Dimensions of Mice Divergently Selected for Body Weight. *Anat. Rec.* **1998**, *250* (3), 292–299. https://doi.org/10.1002/(SICI)1097-0185(199803)250:3<292::AID-AR4>3.0.CO;2-2.

(215) Derrick, T. R.; Thomas, J. M. Time Series Analysis: The Cross-Correlation Function. *Innov. Anal. Hum. Mov.* **2004**, No. 46.

(216) Azaria, M.; Hertz, D. Time Delay Estimation by Generalized Cross Correlation Methods. *IEEE Trans. Acoust.* **1984**, *32* (2), 280–285. https://doi.org/10.1109/TASSP.1984.1164314.

Publishing Agreement

It is the policy of the University to encourage open access and broad distribution of all theses, dissertations, and manuscripts. The Graduate Division will facilitate the distribution of UCSF theses, dissertations, and manuscripts to the UCSF Library for open access and distribution. UCSF will make such theses, dissertations, and manuscripts accessible to the public and will take reasonable steps to preserve these works in perpetuity.

I hereby grant the non-exclusive, perpetual right to The Regents of the University of California to reproduce, publicly display, distribute, preserve, and publish copies of my thesis, dissertation, or manuscript in any form or media, now existing or later derived, including access online for teaching, research, and public service purposes.

_____   Author Signature

12/9/2020
_____
                                                    Date